

RICE UNIVERSITY

**Influence of Varying Analyte Concentration, Environment, and  
Composition on Nanoshell-based SERS**

By

**Carly Sue Levin**

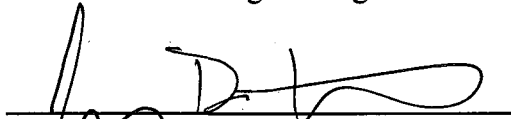
A THESIS SUBMITTED  
IN PARTIAL FULFILLMENT OF THE  
REQUIREMENTS FOR THE DEGREE

**Doctor of Philosophy**

APPROVED THESIS COMMITTEE:



Naomi J. Halas, Chair  
Stanley C. Moore Professor in Electrical and  
Computer Engineering,  
Professor of Chemistry, and  
Professor of Bioengineering



Jeffrey D. Hartgerink  
Associate Professor of Chemistry and  
Associate Professor of Bioengineering



Michael S. Wong  
Associate Professor of Chemical and Biomolecular  
Engineering and  
Associate Professor of Chemistry

HOUSTON, TEXAS  
MAY 2009

UMI Number: 3362348

### INFORMATION TO USERS

The quality of this reproduction is dependent upon the quality of the copy submitted. Broken or indistinct print, colored or poor quality illustrations and photographs, print bleed-through, substandard margins, and improper alignment can adversely affect reproduction.

In the unlikely event that the author did not send a complete manuscript and there are missing pages, these will be noted. Also, if unauthorized copyright material had to be removed, a note will indicate the deletion.

**UMI**<sup>®</sup>

---

UMI Microform 3362348  
Copyright 2009 by ProQuest LLC  
All rights reserved. This microform edition is protected against  
unauthorized copying under Title 17, United States Code.

---

ProQuest LLC  
789 East Eisenhower Parkway  
P.O. Box 1346  
Ann Arbor, MI 48106-1346

## Abstract

Influence of Varying Analyte Concentration, Environment,  
and Composition on Nanoshell-based SERS

By

Carly Sue Levin

This thesis describes a series of experiments designed to examine the use of Au nanoshells as highly controllable surface enhanced Raman spectroscopy (SERS) nanosensor substrates. Individual Au nanoshells provide simple, scalable substrates for SERS with demonstrated strong electromagnetic field enhancements which exist near the molecule-substrate interface. The SERS spectral response is explored as a function of analyte concentration, environmental pH, and various analyte properties and composition. As a function of analyte concentration, the SERS response is exploited for the determination of packing density and molecular conformation of thiolated poly(ethylene glycol) (PEG) adsorbates on Au nanoshells. By varying the environmental pH when a pH-sensitive molecular adsorbate is attached to the Au nanoshells, the resultant SERS spectra allow for local pH monitoring with an average accuracy of  $\pm 0.10$  pH units across the operating range of the nanodevice. Changing analyte properties, such as carbon chain length for alkanethiol self-assembled monolayers (SAMs) on gold, produces a series of sharp resonances in the SERS spectra, suggesting coupling of the gold-sulfur bond stretch with the longitudinal acoustic, “accordion”, vibrations of the molecular alkane chain. Further variation in chain termination or the addition of a phospholipid headgroup yields observable SERS spectral differences, providing unique fingerprints for each molecule. An associated phospholipid layer assembled onto an underlying alkanethiol SAM forms a

hybrid bilayer on Au nanoshells, providing a way to spectrally monitor intercalation of the nonsteroidal anti-inflammatory drug (NSAID), ibuprofen. Low frequency SERS peaks for halogen, nitrogen, and oxygen containing molecules act as probes for metal-adsorbate binding, with spectral evidence for carbon monoxide adsorption occurring in the high frequency region. Finally, we demonstrate the synthesis and characterization of nanoparticles composed of magnetic cores with continuous Au shell layers that simultaneously possess both magnetic and plasmonic properties. The work presented in this thesis further demonstrates the emergence of Au nanoshells as versatile and valuable tools for sensing applications.

**Dedication**

*In Loving Memory of My Grandfather*

*Dr. Erwin Levin*

*1918 - 2008*

## Acknowledgements

First, I would like to thank my advisor Dr. Naomi Halas for her help and guidance during my graduate career. Dr. Halas's enthusiasm for science, critical eye, and wise advice has helped me to develop the essential skills of a successful researcher. Special thanks to my Nanobiology co-mentor Dr. Jeffrey D. Hartgerink, my thesis committee member Dr. Michael S. Wong, and the many professors, post-docs, and students that I have collaborated with: Ben Janesko, Dr. Gustavo Scuseria, Dan Ward, Dr. Douglas Natelson, Cristina Hofmann, Anna Kelly, Teyeb Ould-Ely, Dr. Kenton H. Whitmire, Tamer Ali, Dr. Peter Nordlander, Dr. Emilia Morosan, Chris Rozell, Dr. Bruce Johnson, Dr. Don Johnson, Dr. Susan Clare, Yong Zhou, Dr. Robert M. Raphael, Venky Nammalvar, Dr. Rebekah Drezek, Dr. Kristian Helmerson, Brooke Cranswick, Rani Kishore, Dr. Rajesh Naik and others.

I would also like to extend my appreciation to all current members of the Halas group: Rizia Bardhan, Aoune Barhoumi, Bruce Brinson, Lisa Brown, Jared Day, Tumasang Fofang, Nathaniel Grady, Ryan Huschka, Cyre Kalu, Mark Knight, Janardan Kundu, Britt Lassiter, Nikolay Mirin, Shaunak Mukherjee, Oara Neumann, Chaitra Rai and Joe Young and all former members of the Halas group: Sandra Whaley Bishnoi, Joe Cole, Jeremy Dumoit, Muhammed Gheith, Glenn Goodrich, Serge Grabtchak, Lee Hirsch, Joe Jackson, Surbhi Lal, Kristina Lestick, Yu Liu, Zaw Lwin, Jen Steele, Priya Sundararajan, Felicia Tam, Hui Wang, and Dongmao Zhang. Special mention goes to several undergraduate students for all of their hard work: Allen Chen, Diana DeRosa, Tim Kinney, Julie Liao, Peijing Teh, and to many of Rice's academic and administrative staff: Martha Alexander, Carolyn Aresu, Sofia Medrano-Correa, Angelo Benedetto,

Richard Crouse, Wenhua Guo, Keith Poli. Finally, I would like to thank my friends Jennifer Jamison and Emily Barter, my family, and my husband Sebastian for their patience, support, and encouragement.

## Table of Contents

Abstract .....	ii
Acknowledgements .....	v
Table of Contents .....	vii
List of Figures .....	x
List of Tables .....	xv
Chapter 1: Introduction to surface enhanced spectroscopies and nanoshells .....	1
1.1: Raman scattering .....	1
1.2: Surface enhanced Raman scattering (SERS) .....	3
1.3: Surface enhanced infrared absorption (SEIRA) .....	5
1.4: Electromagnetic properties of nanoshells and their use as surface enhanced spectroscopic sensors .....	7
1.4: Silica-gold nanoshell fabrication, sample preparation, and characterization .....	9
1.5: Thesis outline .....	12
Chapter 2: SERS response as a function of concentration: Determining the conformation of thiolated poly(ethylene glycol) on Au nanoshells .....	13
2.1: Introduction .....	13
2.2: Experimental .....	16
2.3: Results and discussion .....	18
2.4: Conclusions .....	24
Chapter 3: SERS response as a function of pH: An all-optical nanoscale pH meter .....	25
3.1: Introduction .....	25
3.2: Experimental .....	28
3.2: Results and discussion .....	30
3.4: Conclusions .....	37
Chapter 4: SERS response as a function of chain length, terminus, and headgroup: SERS of thiolated aliphatic moieties .....	38
4.1: Alkanethiols .....	38
4.1.1: Introduction .....	38
4.1.2: Experimental .....	39
4.1.3: Results and discussion .....	40



4.1.4: Conclusions .....	48
4.2: $\omega$ -terminated alkanethiols: acids, alcohols, and dithiols .....	49
4.2.1: Introduction .....	49
4.2.2: Results and discussion .....	49
4.3: Alkanethiols with a phospholipid headgroup .....	51
4.3.1: Introduction .....	51
4.3.2: Results and discussion .....	52
Chapter 5: Interactions of ibuprofen with hybrid lipid bilayers probed by complementary surface-enhanced vibrational spectroscopies .....	55
5.1: Introduction .....	55
5.2: Experimental .....	60
5.3: Results and discussion .....	63
5.4: Conclusions .....	78
Chapter 6: SERS of non-thiolated moieties .....	79
6.1: Au-halide complexes .....	79
6.1.1: Introduction .....	79
6.1.2: Results and discussion .....	80
6.1.3: Conclusions .....	82
6.2: Au-oxygen and Au-nitrogen complexes .....	83
6.2.1: Introduction .....	83
6.2.2: Caffeine .....	83
6.2.3: Water soluble cholesterol .....	87
6.2.4: Pyridine .....	88
6.2.5: Aniline .....	90
6.2.6: Nanoshell binding peptide .....	92
6.3: CO adsorption on Au nanoshells .....	94
Chapter 7: Magnetic-plasmonic core-shell nanoparticles .....	98
7.1: Introduction .....	98
7.2: Experimental .....	101
7.3: Results and discussion .....	103
7.4: Conclusions .....	120
Chapter 8: Summary .....	121

References.....	124
Appendix A: TEOS purification by simple distillation .....	146
Appendix B: Image processing and nanoshell sizing using the Scion Image program..	148
Appendix C: Calculating nanoshell concentration using the Beer-Lambert law.....	149
Appendix D: SERS substrate development .....	150

## List of Figures

- Figure 1.1:** Energy level diagram showing the states involved in Raman signal. The line thickness is roughly proportional to the signal strength from the different transitions.<sup>3</sup> .... 2
- Figure 1.2:** Theoretically calculated (Mie scattering) optical resonances demonstrating plasmon tunability for nanoshells with an inner silica core radius  $r_1 = 60$  nm and an overall particle radius  $r_2 = 65, 67, 70,$  and  $80$  nm (corresponding to 5, 7, 10, and 20 nm thick Au shells). The plasmon resonance (extinction) of the particles redshifts as  $r_1/r_2$  increases. Modified from Oldenburg *et al.*<sup>28</sup> to exclude the broadening mechanism..... 8
- Figure 2.1:** (a) Self-assembly of *p*MA on a Au-silica nanoshell. (b) Self-assembly of *p*MA-PEG-FI on a Au-silica nanoshell. (c) Schematic depicting (i) mushroom and (ii) brush configurations of *p*MA-PEG-FI adsorbate molecule. .... 16
- Figure 2.2:** SERS spectra for Au-silica nanoshells coated with (a) *p*MA-PEG5000-FI, (b) *p*MA-PEG2000-FI, and (c) *p*MA (offset for clarity). .... 19
- Figure 2.3:** SERS spectra of *p*MA on Au-silica nanoshells at various concentrations.... 20
- Figure 2.4:** (a) SERS intensity at  $1080\text{ cm}^{-1}$  as a function of *p*MA concentrations (diamonds) and best-fit Langmuir isotherm (line). The inset shows the linear regime. (b) SERS intensity for various amounts of *p*MA molecules per Au-silica nanoshell. .... 21
- Figure 3.1:** Schematic diagram of the Au nanoshell pH sensor, consisting of nanoshells with core radius  $r_1=55$  nm and total nanoparticle radius  $r_2=71$  nm and an adsorbed monolayer of *para*-mercaptobenzoic acid. The *p*MBA molecules yield a pH dependent SERS spectrum. .... 29
- Figure 3.2:** (A) SERS spectra of *p*MBA on NSs at various pH values ranging from pH 4.00 to pH 9.00 in steps of 0.50 pH units. (B) Repetitive cycling of the Raman pH nanosensor measured by monitoring the change in the  $I(\text{COO}^-)/I(\text{C=O})$  ( $1702\text{ cm}^{-1}/1393\text{ cm}^{-1}$ ) Stokes modes. The intensities were measured with respect to that of the  $1077\text{ cm}^{-1}$  band to which spectra (at each pH) were normalized. Error bars represent the standard deviation for the measurements. .... 33
- Figure 3.3:** (a) Spectral changes form a manifold (one-dimensional curve) in  $R^N$  that is indexed by pH, where  $N$  is the number of spectral bands measured. The best piecewise linear fit to the training samples is found using two segments, and that local linear approximation forms a model of the pH manifold. (b) The spectrum of a testing sample is projected onto the model described in a to find the point on the manifold that is closest to the spectrum of the test data. The index of this projected point forms the pH estimate. Cross validation was used to judge the quality of the model (leave one scan out of the model building and then estimate using that scan). The points are the average of the cross validation estimates, and the error bars represent one standard deviation in the cross validation estimates. (c) Magnitude of the average error of the cross validation estimation procedure shown in b. The average error magnitude across the pH range of the device is 0.10 pH..... 35
- Figure 4.1:** Experimental unenhanced liquid Raman (A) and SERS (B-C) spectra on Au nanoshells for alkanethiols  $\text{HS}-(\text{CH}_2)_n-\text{H}$ , where  $n = 10-16$  (offset for clarity). .... 41

- Figure 4.2:** Schematic of the 1D model of (Au surface)-S-(CH<sub>2</sub>)<sub>n-2</sub>-H self-assembled monolayer.  $k$  and  $\alpha$  are the harmonic force constant and polarizability derivative of each bond..... 43
- Figure 4.3:** (A) 1D model results for SERS spectra of (Au surface)-S-(CH<sub>2</sub>)<sub>n</sub>-H, for  $n = 10$  (dodecanethiol, bottom) to  $n = 16$  (hexadecanethiol, top). Simulated spectra are plotted with a uniform Gaussian broadening of  $10 \text{ cm}^{-1}$ . (B) Frequencies of the two narrow, intense peaks in the Au-S-(CH<sub>2</sub>)<sub>n</sub>-H spectra of Figure 4.1B, plotted as a function of chain length (where for the LAM- $k$  peak frequencies,  $\blacktriangle$  is  $k = 1$  and  $\blacksquare$  is  $k = 2$  from experiment, and  $-$  is  $k = 1$  and  $-$  is  $k = 2$  obtained from the 1D model in A)..... 44
- Figure 4.4:** (A) SERS spectra of (Au surface)-S-(CH<sub>2</sub>)<sub>12</sub>-H, as predicted by the 1D model. The  $x$  axis begins at  $0 \text{ cm}^{-1}$  in order to include the  $k = 0$  mode. (B) Normal-mode eigenvectors for the four vibrational modes shown in part A. The longitudinal displacement of each atom is plotted on the  $y$  axis. The  $k = 0, k = 1, k = 2,$  and  $k = 3$  modes occur at  $74, 226, 373,$  and  $519 \text{ cm}^{-1}$ , respectively. The Au-S bond stretch is maximized for the modes with  $k = 2$  and  $k = 3$  internal nodes ( $\square$  is  $k = 0, \blacksquare$  is  $k = 1, \blacktriangle$  is  $k = 2, \bullet$  is  $k = 3$ )...... 45
- Figure 4.5:** Experimental low frequency SERS spectra for dodecanethiol on (A) Ag coated Au and (B) Au nanoshells (offset for clarity) with line indicating the peak position shift from  $316 \text{ cm}^{-1}$  on Ag coated Au nanoshells to  $326 \text{ cm}^{-1}$  for Au nanoshells..... 46
- Figure 4.6:** Results of ab initio electronic structure calculations on Au<sub>3</sub>-S-(CH<sub>2</sub>)<sub>n</sub>-H (see the text). Frequencies of the two narrow, intense peaks in the Au-S-(CH<sub>2</sub>)<sub>n</sub>-H spectra (Figure 4.1B), plotted as a function of chain length  $n$  (where for the LAM- $k$  peak frequencies,  $\blacktriangle$  is  $k = 1$  and  $\blacksquare$  is  $k = 2$  from experiment, and  $\Delta$  is  $k = 1$  and  $\square$  is  $k = 2$  obtained from the ab initio calculations). ..... 47
- Figure 4.7:** (A) Unenhanced Raman spectrum (powder, average of 5 scans), (B) SERS spectrum (1 mM, average of 5 scans), and (C) IR spectrum (powder, coaddition of 256 scans,  $4 \text{ cm}^{-1}$  resolution) of 11-mercaptoundecanoic acid. .... 50
- Figure 4.8:** (A) SERS spectra of (i) 1,9 nonanedithiol (black) and (ii) 1,8 octanedithiol (red) (10 mM, offset for clarity, average of 5 scans). (B) Schematic diagram of the self-assembly process of (1,8) octanedithiol on Au. Different dithiol and disulfide conformations include: (i, iii) an extended chain configuration with one thiol end binding, and (ii, iv) coordination of two or more thiols with the Au surface. .... 51
- Figure 4.9:** Schematic of liposome encapsulated nanoshells and chemical structure of 1,2-dipalmitoyl-sn-glycero-3-phosphothio-ethanol (PTE). .... 53
- Figure 4.10:** Extinction spectra of nanoshells [ $r_1, r_2$ ] = [60, 83] nm suspended in (i) water  $n = 1.22,$  (ii) ethanol  $n = 1.36$  and (iii) functionalized with PTE lipids and suspended in ethanol (spectra offset for clarity)..... 54
- Figure 4.11:** (A) unenhanced Raman spectra of (i) neat hexadecanethiol and (ii) PTE powder, and (B) SERS spectra of 100  $\mu\text{M}$  solutions of (iii) hexadecanethiol and (iv) PTE conjugated to Au nanoshells (spectra offset for clarity, average of 5 scans)..... 54
- Figure 5.1:** Schematic illustration of (A) an ibuprofenate functionalized nanoshell and (B) a hybrid bilayer with ibuprofen intercalation on a nanoshell for SERS measurements.

(C) The interparticle junction of two hybrid bilayer nanoshells with ibuprofen intercalation (dimer shown for simplicity) used for SEIRA measurements. .... 59

**Figure 5.2:** TEM images of (A) a bare Au nanoshell and (B) hybrid bilayer functionalized Au nanoshells deposited on TEM grids (as shown by the line and contrast in B). (C) Optical images of Au nanoshells (i) dispersed in water, (ii) functionalized with an alkanethiol (which preferentially disperse in an organic carbon disulfide layer on the bottom, rather than the top water layer), and (iii) functionalized with a hybrid lipid bilayer dispersed in water. The scale bars in A, B are 20 nm. .... 64

**Figure 5.3:** The excitation generalized polarization ( $GP_{ex}$ ) spectra of hybrid bilayers on nanoshells (HBL) and deuterated hybrid bilayers on nanoshells (HBL-D54) with Laurdan at pH 3 and 10. .... 66

**Figure 5.4:** Raman spectra (A) of (i) ibuprofen sodium salt powder (50x objective, 25.5 mW laser power), (ii) sodium ibuprofenate in aqueous solution (2 M, 63x objective, 40.6 mW laser power), and (iii) surface enhanced Raman spectrum of sodium ibuprofenate (50 mM, 63x objective, 0.144 mW) adsorbed onto Au nanoshells. IR spectra (B) of (i) ibuprofen sodium salt powder and (ii) surface enhanced IR spectrum of sodium ibuprofenate (50 mM) adsorbed onto Au nanoshells (inset shows high frequency regime). (Spectra offset for clarity). .... 68

**Figure 5.5:** (A) Chemical structure of 1,2-Dimyristoyl-*sn*-Glycero-3-Phosphocholine (DMPC) highlighting the phosphate and acyl linkage groups. (B) SEIRA spectra for (i) hybrid bilayers (30  $\mu$ M dodecanethiol with 100  $\mu$ M DMPC lipids), (ii) hybrid bilayers with 200 mM, and (iii) hybrid bilayers with 500 mM ibuprofenate loading solution. The stars indicate the peaks from clearly identifiable modes of the ibuprofenate, indicating its presence in the hybrid bilayer. The lines indicate DMPC modes (spectra are offset for clarity). .... 76

**Figure 6.1:** Normalized SERS spectra of several halogen containing molecules (40 mM, average of 5 scans): (A) cetyltrimethylammonium bromide (CTAB) and chloride (CTAC), (B) sodium iodide (NaI), bromide (NaBr), and chloride (NaCl), (C) iodododecane, bromododecane, and chlorododecane, and (D) acetylcholine iodide, bromide, and chloride. .... 81

**Figure 6.2:** Chemical structure of caffeine. The molecule contains both a pyrimidine ring seen on the left side, and an imidazole ring on the right. The imidazole ring system is present in important biological building blocks such as histidine and histamine. .... 84

**Figure 6.3:** (A) Unenhanced Raman spectrum of caffeine powder (average of 5 scans) and (B) SERS spectra of caffeine functionalized Au nanoshells obtained at pH 2.0 (red), 5.5 (black), and 9.5 (blue) (100  $\mu$ M, offset for clarity, average of 5 scans). .... 85

**Figure 6.4:** Chemical structure of water soluble cholesterol. .... 88

**Figure 6.5:** (A) Unenhanced Raman spectrum of water soluble cholesterol powder (average of 5 scans) and (B) SERS spectrum of water soluble cholesterol adsorbed on Au nanoshells (100  $\mu$ M, average of 10 scans). .... 88

**Figure 6.6:** SERS spectrum of pyridine functionalized Au nanoshells (10  $\mu$ M, average of 5 scans, inset shows the chemical structure of pyridine). .... 90

**Figure 6.7:** (A) Unenhanced Raman spectrum of neat aniline (average of 5 scans) and (B) SERS spectra of aniline functionalized Au nanoshells at pH 3.0 (red) and 10.0 (blue) (1 mM, offset for clarity, average of 5 scans, inset shows the chemical structure of aniline). ..... 90

**Figure 6.8:** Sequence of the Au nanoshell binding peptide NS32Y with predicted charges on the residues in milliQ water at pH 5.5. .... 92

**Figure 6.9:** (A) Unenhanced Raman spectrum of NS23Y powder (average of 5 scans) and (B) SERS spectrum of NS23Y functionalized Au nanoshells (500  $\mu$ M, average of 5 scans)..... 93

**Figure 6.10:** High frequency SERS spectra for *p*MBA functionalized nanoshells (1  $\mu$ M to 0.1 mM). At low *p*MBA concentrations a predominant peak at 2138  $\text{cm}^{-1}$  is observed and attributed to CO. As the concentration of *p*MBA is increased, the adsorbed atop bound CO is displaced and the high frequency peak decreases in intensity. The conversion to a doublet at 2136 and 2181  $\text{cm}^{-1}$  indicates that the little CO that remains occupies the atop adsorption site or consists as free CO in solution near the metal nanoshell. (Normalized intensity, spectra offset for clarity.)..... 97

**Figure 7.1:** Schematic of Au coated iron oxide synthesis for (A) faceted and (D) tetracubic (i) unfunctionalized core, (ii) Au decorated precursor, and (iii) Au coated iron oxide nanoparticles. TEM images representing various stages of synthesis for (B, C) faceted and (E, F) tetracubic (i) unfunctionalized core (with average  $r_1 = 31.5 \pm 9.7$  nm and  $28.5 \pm 7.3$  nm), (ii) Au nanoparticle decorated precursor, and (iii) Au coated iron oxide nanoparticles. .... 104

**Figure 7.2:** Solution extinction measurements of (A) faceted (B) and tetracubic gold coated iron oxide (i) ethanolic uncoated cores ( $r_1 = 31.5 \pm 9.7$  and  $28.5 \pm 7.3$  nm), (ii) Au-decorated precursor nanoparticles ( $r_1 = 32.6 \pm 9.0$  and  $28.6 \pm 8.5$  nm) in aqueous solution, and (iii-vi) Au coated nanoparticles with increasing Au thicknesses (number of particles sized is 100,  $r_2$  is  $59.9 \pm 12.4$ ,  $65.0 \pm 19.9$ ,  $73.1 \pm 11.7$ , and  $76.6 \pm 9.8$  nm for the faceted cores and  $40.0 \pm 6.7$ ,  $49.1 \pm 10.7$ ,  $53.8 \pm 4.6$ , and  $66.4 \pm 5.0$  nm for the tetracubic cores in aqueous solution. (Spectra offset for clarity.) (C) Optical image of particles shown in A. .... 105

**Figure 7.3:** Hybridization in a nanoshell (A) with a low permittivity core, *e.g.*, silica, and (B) with a high permittivity core, *e.g.*, iron oxide. Dark (black) and bright (red) plasmon modes are shown in each case. Arrows show the shift of the hybridized plasmon modes with increasing shell layer thickness. The colored insets show local electric field enhancements distributions for the spherical-core geometries in Figure 4A,B. A silica core is selected for insets in (A) showing dark (A-upper) and bright (A-lower) modes. A high permittivity core ( $\epsilon = 12.0$ ) is selected for insets in (B) showing bright (B-upper) and dark (B-lower) modes. The inner radius of the core is  $r_1 = 32$  nm and the outer radius of the shell is  $r_2 = 50$  nm. A drude model is used to represent the gold material dielectric properties..... 106

**Figure 7.4:** (A,B) Theoretical comparison of extinction spectra for nanoshells with cores of different shapes: spherical (blue solid line), cubic (red dashed line), and concave cubic (green dash-dotted line). The outer radius of the shell is  $r_2 = 50$  nm and the effective

radius of the core is  $r_{\text{eff}} = 32$  nm. The core dielectrics are (A) silica ( $\epsilon = 2.04$ ) and (B) an artificial material with  $\epsilon = 12.0$ . (C,D) Calculated LSPR shifts of the (C) bonding dipolar nanoshell resonances for a silica core and (D) antibonding dipolar nanoshell resonances for an artificial core with  $\epsilon = 12.0$ , as a function of the ratio of the outer radius of the shell,  $r_2$ , to the effective core radius  $r_{\text{eff}} = 32$  nm. .... 109

**Figure 7.5:** Comparison of the electric field enhancement distribution in an equatorial plane through the center of the three different nanoshells. The dipolar modes ( $l = 1$ ) are shown for (A) spherical, (B) cubic, and (C) concave cubic cores at 565 nm, 599 nm, and 623 nm, respectively. (D) The quadrupole mode ( $l = 2$ ) is shown for the concave cubic core geometry at 542 nm. The parameters used in this simulations are the same as Figure 7.4A. Inset shows the nanoparticle shape. .... 111

**Figure 7.6:** (A) Theoretical color contour representation of the extinction spectra for different core dielectric permittivities and shell thicknesses for the same effective core radius of  $r_{\text{eff}} = r_1 = 36$  nm. Each panel shows the extinction spectra for a fixed  $\epsilon_{\text{core}}$  with the shell radius increasing from  $r_2 = 50$  to  $r_2 = 70$  nm. The color corresponds to the extinction cross-section values normalized to the maximum extinction value. The surrounding medium is water (dielectric constant of 1.77). (B-D) Theoretically calculated extinction spectra for spherical nanoshells with different shell thicknesses (where  $r_{\text{eff}} = r_1 = 36$  nm) normalized to the thinnest shell extinction peak, using a (B) high core dielectric permittivity of 22, (C) core dielectric permittivity of 12, and (D) low core dielectric permittivity of 2. The bright mode does not significantly shift in (D) and redshifts in (B) to higher wavelengths. The best match to the experimental data behavior is shown in (C). .... 112

**Figure 7.7:** Powder X-ray diffraction patterns for (i) iron oxide core nanoparticles (tetracubes), (ii) Au nanoparticle decorated precursors, and (iii) Au coated iron oxide nanoparticles (with 10.9 nm shell thickness). (B) XRD peak positions for (i) wüstite, (ii) magnetite, and (iii) gold. .... 116

**Figure 7.8:** Raman spectrum of iron oxide nanoparticles (785 nm, 1.5 mW). The wüstite ( $\text{Fe}_x\text{O}$ ) phase undergoes mild oxidation to magnetite ( $\text{Fe}_3\text{O}_4$ ).<sup>292</sup> .... 116

**Figure 7.9:** (A) Optical images of (i) Au-decorated iron oxide precursor particles, (ii) Au-decorated iron oxide precursor particles with magnet, (iii) Au coated nanoparticles, and (iv) Au coated nanoparticles with magnet. (B) Representative SEM image of the shells shown in (iv). .... 117

**Figure 7.10:** Magnetization as a function of magnetic field at constant temperature (100 K or 250 K) for (A) uncoated and (B) Au coated iron oxide nanoparticles (tetracubic, with 10.9 nm shell thickness, where insets show the magnetic hysteresis). .... 120

**Figure 7.11:** Magnetization measurements as a function of temperature for uncoated and Au coated iron oxide nanoparticles (tetracubic with 10.9 nm shell thickness). .... 120

**Figure 0.1:** Typical apparatus for simple distillation at atmospheric temperature or under vacuum. Inset shows correct placement of thermometer in stillhead. .... 147

## List of Tables

<b>Table 2.1:</b> Mushroom and Brush Regime Estimates from Lipid Membrane Studies and Experimental Values of the Number of Molecules Per Nanoshell for a 2000 MW and 5000 MW PEG Linkers <sup>a</sup> .....	23
<b>Table 5.1:</b> IR Peak Assignments for Hybrid Bilayers on Au Nanoshells <sup>194,198-200</sup> .....	76
<b>Table 5.2:</b> IR Peak Assignments for Ibuprofen <sup>186,187</sup> .....	77



## **Chapter 1: Introduction to surface enhanced spectroscopies and nanoshells**

### **1.1: Raman scattering**

When incident light excites a molecule, most of the light scattered by the molecule consists of photons which have the same frequency and wavelength as those incident photons. This form of scattering, known as elastic or Rayleigh scattering, involves negligible energy transfer. However, a few of these photons will either gain or lose energy and are inelastically scattered. When inelastic scattering was first experimentally reported in a 1928 Nature paper by Raman and Krishnan, it was described by its “feebleness in comparison with the ordinary scattering.”<sup>1</sup> Today, the inelastic scattering process is referred to as Raman scattering, and the small fraction of scattered photons with a frequency different from the incident photons is approximately 1 in 1 million.<sup>2</sup> Of this fraction, most of the photons are lower in frequency than those that are incident. This results from an excitation from the ground state to a virtual energy state, followed by a relaxation into an excited vibrational state known as Stokes scattering. However, if the initial state is instead a vibrationally excited state, the molecule may then relax to the ground state; causing the scattered photon to have a greater frequency and appear at higher energy. This effect at room temperature is rare and known as anti-Stokes scattering. A Rayleigh and Raman scattering energy level diagram is presented in Figure 1.1.

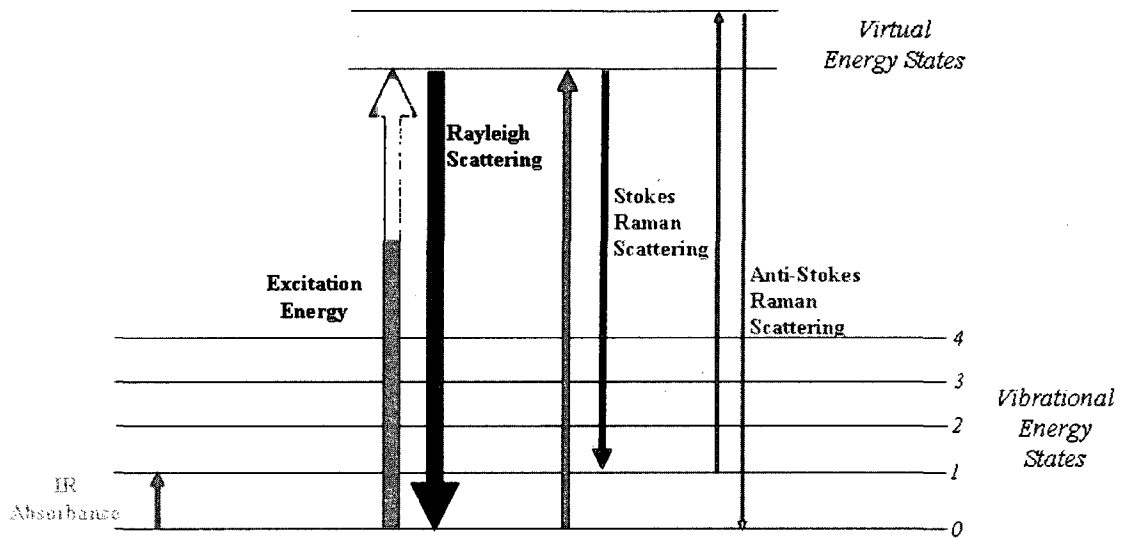


**Figure 1.1:** Energy level diagram showing the states involved in Raman signal. The line thickness is roughly proportional to the signal strength from the different transitions.<sup>3</sup>

Molecular vibrations can be detected by observing a shift in wavelength compared to that of an excitation source. The different functional groups of a molecule each have characteristic vibrational energies, so that every molecule presents a unique Raman spectrum. This makes Raman spectroscopy a valuable and powerful technique as it provides a molecular fingerprint rich in structural information.<sup>4,5</sup> A molecular vibration distorts the electron cloud around a molecule and displaces the constituent atoms from their equilibrium positions. This distortion is known as polarizability, and the intensity of Raman scattering is proportional to the amount of polarizability change.

In addition to high specificity, Raman spectroscopy has numerous advantages as an analytical technique. The analyte does not need special sample preparation or pretreatment, can be reused as it is not destroyed, and may remain in aqueous solution. Spectra are rapidly acquired and chemical reactions can be monitored in real time. Changes in an analyte's composition and structure, for example, due to oxidation under a Raman laser<sup>6</sup>, can be examined. Near-instantaneous results, along with commercially

available libraries and modeling software, have provided advances in the evolution of Raman spectroscopy. However, the normal Raman scattering process remains limited in the absence of resonance or surface enhancement as the Raman cross sections of molecules are very small (such as  $2.6 \times 10^{-31} \text{ cm}^2 \text{ sr}^{-1}$  at 514.5 nm for  $\text{N}_2$ ).<sup>7</sup>

## **1.2: Surface enhanced Raman scattering (SERS)**

By placing the analyte molecule or scatterer on or near a roughened noble-metal substrate, the magnitude of the Raman scattering signal can be significantly enhanced. This technique, known as surface enhanced Raman spectroscopy (SERS) and discovered over 30 years ago<sup>8,9</sup>, is a suitable application for studying small quantities of analytes and low concentrations. It is generally accepted that SERS is the result of two main effects: a chemical effect and an electromagnetic (EM) effect. The chemical effect, now thought to contribute an average enhancement factor of 100, involves the creation of a charge transfer state between the metal and adsorbate molecules.<sup>10</sup> However, it is the EM effect that provides the main contribution, where the local electromagnetic field close to a roughened noble-metal surface is greatly enhanced due to the excitation of a localized surface plasmon (LSP).

Surface plasmons are the collective oscillations of the conduction electrons against the background of ionic metal cores.<sup>8,9,11-13</sup> Since metals have a high density of free electrons to move, they support plasmons. Localized plasmons arise when the plasmon excitation occurs at an interface with dimensions comparable to or significantly smaller than the wavelength of excitation. When metal nanoparticles are excited by electromagnetic radiation, their conduction electrons collectively oscillate, exhibiting localized surface plasmons.<sup>11</sup> The size, shape, and dielectric properties of the metal

nanoparticles determine the wavelength (corresponding to the extinction maximum,  $\lambda_{\text{max}}$ ) of the localized surface plasmon resonance.<sup>12</sup> Noble metal nanoparticles Au, Ag, and Cu have the ability to support plasmon resonances at visible wavelengths.<sup>13</sup> When the incident photon energy is in resonance with the localized surface plasmons, large electromagnetic fields are generated on the surface of the structure. The intense, optical frequency evanescent field that is excited at the nanoparticle surface is known as the near field. The strength of this enhanced near field decays off with distance away from the metal surface.

SERS exploits the use of LSPs and their resultant large electromagnetic fields. The process consists of five of significant steps. First, an incoming photon interacts with a metallic substrate, exciting a plasmon. Next, the plasmon polarizes a nearby molecule which creates a large dipole moment. Following, the molecular polarization is altered when the molecule changes its vibrational state. This resultant change in polarization couples back into an emitted plasmon. Finally, the plasmon then couples to an outgoing Raman scattered photon, completing the process.<sup>14</sup>

Since both the excitation field and the Raman scattered field contribute to enhancement, the SERS signal is proportional to the fourth power of the field enhancement.<sup>15</sup> For high enhancement to be obtained, it is desirable to have the laser excitation wavelength near or within the linewidth of the plasmon resonance band. Isolated, single, colloidal silver and gold have reported calculated maximum electromagnetic field enhancements on the order of  $10^6$ - $10^7$  for excitation wavelengths at the appropriate single-particle plasmon resonance (407 and 514 nm).<sup>15</sup> However, random aggregates of these colloidal nanoparticles were used to provide the first clear

demonstration of single molecule SERS (SM-SERS) detection.<sup>15-18</sup> While these aggregates and assemblies provide strong enhancements, they prove difficult to precisely reproduce at predetermined locations. Nanoparticle arrays offer a more robust and reliable alternative and have shown an average SERS enhancement factor of  $>10^8$  under near-infrared (785 nm) excitation.<sup>16</sup>

As the field of nanotechnology rapidly develops, the application of SERS has become more widespread in analytical, material, and biochemical research. SERS is being fueled by advances such as single molecule detection and new substrate development as simple, scalable substrates are in demand. One alternative is nanometer-scale electromigrated gaps between extended electrodes, which have proven to be reliable and sensitive substrates for SERS.<sup>17</sup> Substrates are being plasmonically tailored<sup>18</sup> as new nanostructure geometries and their plasmonic properties are explored.

### **1.3: Surface enhanced infrared absorption (SEIRA)**

Similar to Raman spectroscopy, conventional infrared (IR) spectroscopy has also been established as routine molecular-specific technique for the characterization of chemical species. However, this analytical technique has also been criticized in that it lacks sufficient sensitivity for trace concentrations.<sup>19</sup> The application of surface enhanced infrared absorption (SEIRA) spectroscopy overcomes this limitation and in combination with SERS, it unifies the field of surface enhanced vibration spectroscopy (SEVS). SEIRA, typically observed on small ( $\ll$  wavelength of light) metal islands<sup>20</sup> and films of metallic nanoparticles<sup>21</sup>, is due to chemical and two important electromagnetic mechanisms: the lightning rod effect and hybridized plasmons.

The phenomenon known as the lightning rod effect is associated with geometric factors and is distinct from plasmons. The incident electromagnetic field cannot appreciably penetrate inside a metal and is instead compressed into the gap between two adjacent metal structures.<sup>18</sup> In the low frequency regime, the screening is efficient because the real part of the dielectric function of metals becomes large and negative. This phenomenon results in a slow monotonic increase of the maximum field enhancement over the midIR region (2 – 20  $\mu\text{m}$ ). These large electric field enhancements in metallic junctions at long wavelengths is not limited to nanoshells or nanoshell arrays.<sup>22</sup> Crowding of the field can also take place near a small radius of curvature or at sharp points, and occurs for all metal objects in the IR and terahertz regions where metals are essentially perfect conductors.

Hybridized plasmons occur when two individual nanostructures are brought together so that their individual plasmons can couple. This interaction creates a new “dimer” plasmon which results in a wavelength shift that depends sensitively on the particle separation.<sup>23</sup> Changing the local dielectric in their interparticle junction region by loading it with molecules contributes to an additional red-shift.<sup>24</sup> These large plasmon shifts along with the corresponding electromagnetic hot spots are suitable for SEIRA spectroscopy, where the plasmon frequencies must overlap directly to the dipole-active vibrational modes of the adsorbate molecule.

The combination of these two processes, along with chemical enhancements, results in infrared absorption of 10 to 1,000 times more intense than would be expected from conventional measurements without the metal. For SEIRA, enhancements are determined by the square of the local field enhancements<sup>25</sup> while for SERS, it is

dependent on the fourth power of the local field enhancements<sup>26</sup>. Also similar to SERS, the enhancement is a near field effect and, therefore, occurs within a short distance from the surface. This allows for the selective detection of signals from the adsorbed monolayer. Techniques such as SERS and SEIRA, which lower the detection limit of conventional Raman and infrared spectroscopy, are of great interest, but in order to systematically understand these processes the continued engineering and exploration of new plasmonic substrates is required.

#### **1.4: Electromagnetic properties of nanoshells and their use as surface enhanced spectroscopic sensors**

Nanoshells are core-shell nanostructures consisting of a dielectric core coated with a thin, metallic shell.<sup>27,28</sup> Their plasmon resonances can be tuned to specific wavelengths from the visible to midIR region of the electromagnetic spectrum by varying the nanoshell core and shell dimensions.<sup>29-32</sup> For a given core radius, a decrease in shell thickness (or increase in the core to shell ratio) shifts the plasmon peak to longer wavelengths (Figure 1.2). This optical tunability enables the use of nanoshells in a broad range of biomedical applications, such as whole blood immunoassays,<sup>33</sup> optically triggerable drug delivery,<sup>34</sup> and photothermal cancer therapy,<sup>35-38</sup> all made possible by tuning the nanoshell plasmon resonance to absorb in the near-infrared region of the electromagnetic spectrum, where blood and tissue are most transparent. Plasmon resonances in the near-infrared region also make it possible to perform dual *in vivo* imaging and therapeutic application.<sup>39</sup> For example, Au nanoshells have been proven to function as therapeutic agents for photothermal cancer treatment, where, by loading them into monocytes, they can serve as “Trojan Horses”. Nanoshell-loaded monocytes are

recruited into hypoxic regions within tumors, which are virtually inaccessible to current cancer therapies, and near-infrared light illumination then results in photoinduced cell death of the monocytes/macrophages within the tumor spheroid.<sup>40</sup>

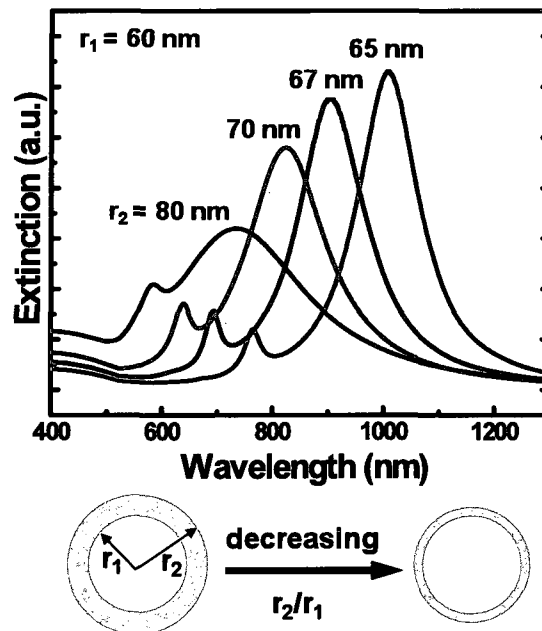


**Figure 1.2:** Theoretically calculated (Mie scattering) optical resonances demonstrating plasmon tunability for nanoshells with an inner silica core radius  $r_1 = 60$  nm and an overall particle radius  $r_2 = 65, 67, 70,$  and  $80$  nm (corresponding to 5, 7, 10, and 20 nm thick Au shells). The plasmon resonance (extinction) of the particles redshifts as  $r_1/r_2$  increases. Modified from Oldenburg *et al.*<sup>28</sup> to exclude the broadening mechanism.

Au nanoshells have also been shown to provide highly controllable spectroscopic substrates. The extinction spectra of nanoshells quantitatively agree with classical Mie scattering theory,<sup>41</sup> which allows for accurate nanoengineering of their optical response. The core and shell dimensions can be designed to provide a high-intensity plasmon-resonant local field at the nanoparticle surface to optimize the SERS response of individual nanoshell substrates for a chosen pump laser wavelength.<sup>42,43</sup> SERS in the near-infrared region of the spectrum is desirable since Raman scattering alone is much weaker in this region compared to the visible region, and any unwanted background



fluorescence from molecules is drastically reduced in this wavelength range.<sup>44</sup> The average SERS enhancements integrated over a nanoshell surface can be comparable to those obtained in the much higher field, smaller sampling volume geometry of a junction between two adjacent nanoparticles, also known as a “dimer” or “hot spot”.<sup>45</sup> Analogous to nanoparticle dimers, the formation of small aggregates or arrays of nanoshells also allow one to resonantly engineer the large local electromagnetic field out into the mid-infrared region of the spectrum, providing a high-quality substrate for surface enhanced infrared absorption (SEIRA) spectroscopy.<sup>46,47</sup> Plasmon resonance excitation in these two diverse frequency regions, visible and infrared, allows for the combined use of the two complimentary vibrational spectroscopies, SERS and SEIRA, on a single substrate. Furthermore, since similar surface selection rules operate for these two spectroscopies,<sup>48</sup> which arise from the fact that the component of the transition dipole normal to the surface is excited more strongly than the tangential component,<sup>49</sup> it is preferable to combine the use of SERS and SEIRA when possible to provide a complete analysis regarding surface orientation and intermolecular interactions.

#### **1.4: Silica-gold nanoshell fabrication, sample preparation, and characterization**

Silica-Au nanoshells were fabricated according to previously reported protocols.<sup>28</sup> The silica cores were synthesized using the Stöber method<sup>50</sup> of particle growth or obtained from Precision Colloid (Cartersville, GA). In the Stöber method, tetraethyl orthosilicate (TEOS), ammonium hydroxide, and ethanol are combined as outlined in Appendix A. Distillation of the TEOS before mixing results in a more monodisperse

solution of silica particles. A general protocol for the purification of TEOS by simple distillation along with a diagram for the apparatus setup can be found in Appendix A.

The nanoshells were designed to elicit a SERS response on individual nanoshell surfaces. The nanoshell core and shell dimensions were adjusted so that the plasmon resonance provided a far-field absorbance maximum near 785 nm in either air or water, to provide SERS enhancement at the 785 nm pump laser wavelength. For SERS measurements in air, Au nanoshells were fabricated with a 90 nm core radius and 17 nm shell thickness, while for solution SERS measurements, Au nanoshells were fabricated with either a 63 nm core radius and approximate 20 nm shell thickness or 55 nm core radius and 16 nm shell thickness. The internal and overall dimensions of the nanoparticles were confirmed using UV-visible extinction measurements, comparison with Mie scattering theory, and scanning electron microscopy (SEM). A detailed protocol describing SEM image processing and nanoshell sizing using the Scion Image program can be found in Appendix B. For Mie scattering calculations, an empirically determined dielectric function was used for that of Au,<sup>51</sup> while a constant dielectric of  $\epsilon = 2.04$  was used for that of the porous silica core<sup>52,53</sup>. Appendix C describes the use of Mie theory and the Beer-Lambert Law to determine nanoshell concentration.

SERS substrates consisted of nanoshells deposited onto either glass or quartz slides or silicon wafer supports (Addison Engineering, Inc.) coated with poly(4-vinylpyridine) (PVP)<sup>54</sup> or functionalized with either (3-aminopropyl)triethoxysilane (APTES, Aldrich) or poly-L-lysine (0.1% w/v in water, Sigma) for attachment of the nanoparticles to the support. Before any coating or functionalization was performed, the slides/wafers were cleaned in a piranha solution (7:3 v/v 98% H<sub>2</sub>SO<sub>4</sub>: 30% H<sub>2</sub>O<sub>2</sub>), rinsed

with milliQ water, followed by rinsing with 200 proof ethanol and dried in a stream of N<sub>2</sub>. A detailed protocol describing SERS substrate development can be found in Appendix D.

SERS spectra were obtained using a Renishaw inVia micro-Raman spectrometer with a 785 nm excitation laser with a 30 μm by 3 μm spot size. The incident NIR laser beam is focused through an objective lens and the sample spot is illuminated. The reflected light is then collected in a backscattered geometry through the objective, where it passes through a holographic notch filter which rejects any Rayleigh scattered light. The backscattered light is then dispersed using a 1200 lines / mm grating and detected on a charge-coupled device (CCD) detector. This configuration allows for recorded spectra with a spectral resolution of approximately 1 datapoint / cm<sup>-1</sup> in the spectral region between 150 and 3200 cm<sup>-1</sup>. Typically, measurements were performed with a 20 s integration time and anywhere from 55 μW to 8 mW power across the sample. For SERS measurements in air a 50x objective was used, while for solution measurements a 63x water immersion objective was used.

Scanning electron microscope (SEM) images were obtained on a FEI Quanta 400 environmental SEM at an accelerating voltage of 20 kV. SEM images of over 100 particles were processed with Scion Image to determine an average particle radius and accompanying size distribution (standard deviation of particle radii). Transmission electron microscope (TEM) micrographs were obtained using a JEOL 2010 TEM. Extinction spectra were obtained using a Cary 5000 UV/Vis/NIR spectrophotometer.

## 1.5: Thesis outline

In this thesis, gold nanoshells are used as a stand-alone SERS nanosensor substrate and their SERS response is explored as a function of analyte concentration, environment, and composition. Chapter 2 discusses the surface-enhanced Raman scattering response and concentration dependence of thiolated poly(ethylene glycol) (PEG) adsorbates on Au nanoshells. By incorporating the linker molecule *p*-mercaptoaniline (*p*MA), the number of 2000 MW and 5000 MW PEG molecules on each nanoparticle is determined by interpolation of the Langmuir isotherm for *p*MA. The packing density and PEG adsorbate configuration on Au nanoshell surfaces is also determined. Chapter 3 investigates changing the local environmental pH and its effects on the SERS response of the pH-sensitive molecular adsorbate, *p*-mercaptobenzoic acid (*p*MBA). Chapter 4 considers the resultant differences in the SERS response for nanoshells functionalized with alkanethiols through modifying various analyte properties, such as chain length, chain termination, and introduction of a phospholipid headgroup. Chapter 5 explores hybrid bilayer formation on gold nanoshells and SERS detection and characterization of the membrane-associated molecule ibuprofen. Chapter 6 examines the SERS response of non-thiolated moieties, where low frequency SERS spectra are presented for analyte molecules containing halogens or oxygen and nitrogen functional groups, and high frequency spectra present evidence for carbon monoxide adsorption on Au nanoshells. Finally, the synthesis and plasmonic properties of bifunctional nanoshells containing a magnetic iron oxide core are demonstrated in Chapter 8. Chapter 9 summarizes the results and discusses possible future directions.

## **Chapter 2: SERS response as a function of concentration: Determining the conformation of thiolated poly(ethylene glycol) on Au nanoshells**

### **2.1: Introduction**

It is highly valuable to obtain SERS spectra as a function of analyte concentration, a parameter which can easily be experimentally altered. Due to the enhancement of different modes of the molecule at different concentrations, SERS provides insight into the behavior of the analyte and its preferred orientation. SERS also offers a low molecular detection limit down to pico- to zeptomolar adsorbate concentrations and is routinely used to characterize sub-monolayer coverage of surface-bound molecules.<sup>4</sup> In this chapter, a quantitative, nondestructive assay based on surface-enhanced Raman scattering (SERS) is presented for determining the number and, therefore, packing density of PEG molecules bound to Au nanoshell surfaces.<sup>55</sup> The conformation of the PEG adsorbates on nanoshell surfaces is also determined. All SERS spectra were taken by Carly Levin. Sandra W. Bishnoi and Nathaniel K. Grady contributed to spectral analysis, interpretation, and discussion. Reproduced with permission from Levin, C. S.; Bishnoi, S. W.; Grady, N. K.; Halas, N. J. *Anal. Chem.* 2006, 78, 3277-3281. Copyright 2006 American Chemical Society.

For the current discoveries in nanoscience to mature into useful technologies, there is a critical need for accurate, quantitative characterization methods of nanoscale structure and composition. This is particularly important in biomedical applications, where uncontrolled or unmonitored changes in nanoscale structure, chemical composition, or molecular conformation may dramatically affect physiological response to a pharmaceutical or nanoscale device. In particular, precise quantification of molecular

densities and conformations in organic-inorganic functional nanostructures will greatly advance our abilities to understand, optimize, and control their efficacy and distribution in complex physiological environments.

Poly(ethylene glycol) (PEG) is a polymer of unusually widespread applicability in biomedicine. The attachment of PEG oligomers to oncological pharmaceuticals, such as interferon- $\alpha$ , doxorubicin, or filgrastin, is currently used to lengthen the circulation time of these molecules in the bloodstream, reducing the frequency that these drugs must be administered, and increasing efficacy and tolerability.<sup>56</sup> The size, geometry, and attachment site of the PEG moiety play such a critical role in determining the pharmacokinetics of the functionalized pharmaceutical that therapeutically optimized agents must be designed on a case-by-case basis.<sup>57</sup> Recent reports of photothermal cancer therapy based on Au nanoshells, metallodielectric nanoparticles consisting of a spherical dielectric core coated with a thin metallic shell, have utilized thiolated PEG coatings to reduce unwanted protein adhesion under untargeted local or systemic delivery.<sup>35,38</sup> Surface passivation of nanoshells using covalently bound thiolated PEG, in combination with antibody conjugation, assisted in maintaining antibody activity in targeted delivery.<sup>36,37</sup> When bound to cylindrical Au nanorods, thiolated PEG disrupts the strong interparticle interaction that leads to nanoparticle aggregation, allowing them to be dispersed in aqueous media and making them amenable to biomedical applications.<sup>58</sup> There is no available information, however, about the molecular conformation of thiolated PEG layers bound to Au nanoparticles of any geometry.

PEG has been shown to adopt two different molecular conformations when grafted onto lipid membranes: “mushroom” and “brush”.<sup>59</sup> In the mushroom

conformation, the chains are randomly oriented and a low packing density is maintained. In the brush conformation, the polymer chains are more extended and weakly aligned and the molecular layer maintains an ~10-fold greater packing density than the mushroom configuration. Determining the number of thiolated PEG molecules on a nanoshell surface will allow us to infer a packing density and, thus, a preferred molecular conformation, for PEG on the nanoparticle surface. Since no direct method currently exists for quantifying the number of PEG molecules bound to a nanoparticle surface, the conformation of PEG when bound to nanoparticle surfaces is unknown, as is any potentially conformation-dependent influence on nanoparticle biodistribution.

SERS measurements were utilized to acquire a Langmuir isotherm for *p*-mercaptoaniline (*p*MA) on nanoshell substrates. This isotherm serves as our “standard” since *p*MA possesses a known packing density on Au surfaces.<sup>60</sup> The 2000 and 5000 MW PEG polymer chains were conjugated to a *p*MA linker molecule and subsequently bound to nanoshell substrates. The *p*MA signal intensities at saturation coverage of each of these two “unknowns” were compared by interpolation with the *p*MA isotherm. From this measurement, the packing density of the 2000 and 5000 MW PEG were determined. In each case, the measured adsorbate packing densities were consistent with a “brush” configuration of PEG on the nanoparticle surface.

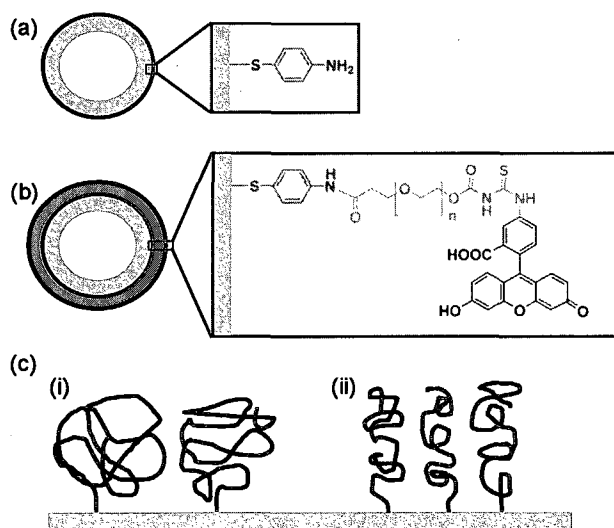


**Figure 2.1:** (a) Self-assembly of *p*MA on a Au-silica nanoshell. (b) Self-assembly of *p*MA-PEG-FI on a Au-silica nanoshell. (c) Schematic depicting (i) mushroom and (ii) brush configurations of *p*MA-PEG-FI adsorbate molecule.

## 2.2: Experimental

Self-assembled monolayers (SAMs) of both *p*MA and the engineered molecule *p*MA-PEG-fluorescein (FI) formed on Au nanoshells are illustrated schematically in Figure 2.1. A fluorescein tag was utilized on the PEG to provide independent quantitation of PEG in solution based on fluorescein extinction and also to provide additional assurance that the SERS signal from the PEG adsorbates was due to the presence of the entire *p*MA-PEG-FI conjugate complex. Potentially, the fluorescein moiety could allow for fluorescence monitoring in conjunction with SERS measurements to obtain additional information about the packing density of the conjugate. However, as the conjugate remains bound to the nanoshells, this type of measurement is problematic, due to likely fluorophore quenching because of the proximity to the Au surface. This would yield strong variations in the signal as a function of distance between metal and fluorophore,<sup>61-63</sup> which would make quantitation using fluorescence impossible since the fluorescence



yield per molecule would not match the standard intensity of the free fluorophore. *p*MA-PEG-fluorescein was synthesized using two different PEG linker lengths with a repeating monomer unit of 45 and 114. N-Hydroxysuccinimide (NHS)-PEG-fluorescein with molecular weights 2410 and 5546 (Nektar Therapeutics, Huntsville, AL) was dissolved in a 1 mM borate buffer solution (pH 9.1). *p*MA was first solubilized in dimethyl sulfoxide and then dissolved in the borate buffer solution. The NHS-PEG-fluorescein and *p*MA in 2-fold excess were combined and dialyzed for ~10 h to allow for amide bond formation of the *p*MA-PEG-fluorescein.<sup>64</sup> The solvent was changed during dialysis to allow for removal of N-hydroxysuccinimide and to allow for a more complete conjugation. Excess unbound *p*MA was removed by membrane dialysis. After incubation, both *p*MA-PEG-FI conjugates were quantified by UV-visible extinction, based on an absorbance value at 494 nm and an extinction coefficient of 78 000 M<sup>-1</sup>cm<sup>-1</sup>, to determine solution concentrations following dialysis.<sup>65</sup> Au nanoshells of core radius 90 nm and shell thickness 17 nm were fabricated as previously described, where the internal and overall dimensions of the nanoparticles were confirmed by consistent determination using UV-visible extinction measurements, comparison with Mie scattering theory, and scanning electron microscopy (SEM).<sup>28</sup> For nanoshells with an outer radius of 107 nm, the corresponding surface area is 3.6 x 10<sup>4</sup> nm<sup>2</sup> per nanoparticle.

SERS substrates consisted of nanoshells deposited onto glass slides coated with either poly(4-vinylpyridine) (PVP)<sup>54</sup> or functionalized with (3-aminopropyl)triethoxysilane for attachment of the nanoparticle to the glass support. The average number of nanoshells per laser spot was 188 ± 28 as determined by counting the nanoshells in 60 SEM micrographs of sample substrates. The SERS spectra were

obtained using a Renishaw inVia micro-Raman spectrometer with a 785-nm excitation laser at 8 mW power across the sample with a 30  $\mu\text{m}$  by 3  $\mu\text{m}$  spot size and 20-s integration time. All spectra were acquired in ambient air.

### 2.3: Results and discussion

The SERS spectra in Figure 2.2 for Au nanoshells coated with *p*MA (a) and the 2000 MW and 5000 MW *p*MA-PEG-FI conjugates (b, c), were obtained from a 1  $\mu\text{M}$  solution and allowed to dry. The spectra show predominant Stokes features (1590 and 1077  $\text{cm}^{-1}$ ) arising from the Raman active bending and stretching modes of the benzene moiety in the *p*-mercaptoaniline molecule,<sup>66</sup> which dominate the SERS spectra and are assigned to  $\nu_{8a}$  and  $\nu_{12}$  aromatic ring vibrations, respectively.<sup>67,68</sup> Traces b and c in Figure 2.2 show the same prominent *p*MA modes as in Figure 2.2a with a noticeable additional peak at  $\sim 1330 \text{ cm}^{-1}$ , attributed to the xanthene ring of the fluorescein moiety.<sup>69</sup> The 2000 MW PEG conjugate exhibits more distinct fluorescein Stokes features than the 5000 MW PEG conjugate, most likely because of the greater number of molecules on a nanoshell surface (smaller molecular footprint) and the possibility that the fluorescein moiety is closer to the surface for this smaller oligomer-based conjugate. The observation of both *p*MA and fluorescein peaks in the SERS spectra provides evidence of the successful conjugation of the *p*MA-PEG-FI and its attachment via the thiol moiety to the nanoshell surface.

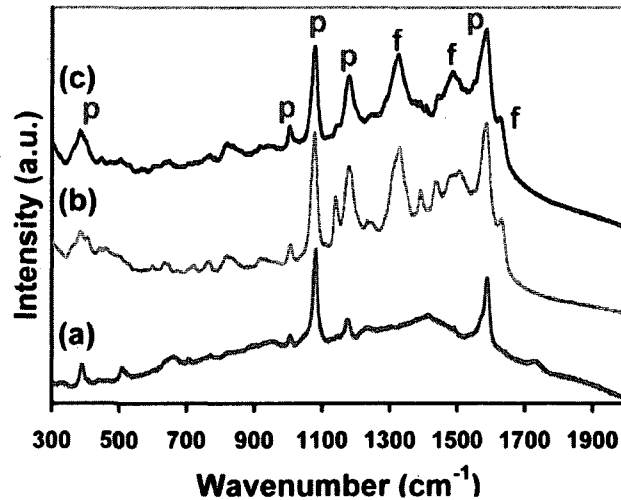


**Figure 2.2:** SERS spectra for Au-silica nanoshells coated with (a) *p*MA-PEG5000-FI, (b) *p*MA-PEG2000-FI, and (c) *p*MA (offset for clarity).

By acquiring SERS spectra of a substrate (nanoshells) exposed to adsorbate solutions (*p*MA) of a range of concentrations (Figure 2.3), an adsorption isotherm can be constructed.<sup>70,71</sup> The spectra shown at each concentration are the average of 12 spectra obtained from 3 prepared samples. At low concentrations, the intensity of the spectral features increase rapidly with increasing concentration and asymptotically approach saturation coverage at high *p*MA concentrations.

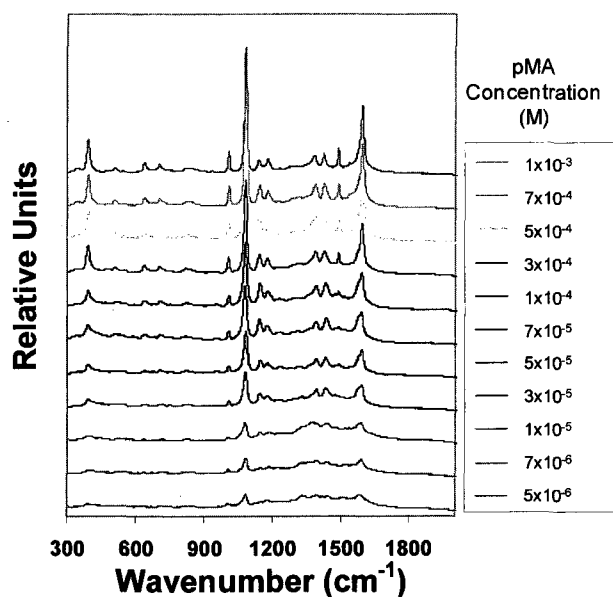


**Figure 2.3:** SERS spectra of *p*MA on Au-silica nanoshells at various concentrations.

Construction of a Langmuir isotherm, shown in Figure 2.4, of unconjugated *p*MA on Au nanoshell surfaces provides a standard curve from which the surface coverages of the *p*MA-PEG-fluorescein can be interpolated. The 1080-cm<sup>-1</sup> mode was chosen for analysis because, as an a<sub>1</sub> in-plane mode of the benzene ring, it is orientation independent.<sup>72</sup> Here, the error bars indicate the standard deviation in SERS intensity for three prepared samples at each concentration. The data follow the well-known equation for a Langmuir isotherm:<sup>70</sup>

$$y = \frac{Akx}{1+kx} \quad \text{Equation 1}$$

where  $y$  is the Stokes intensity of the 1080-cm<sup>-1</sup> mode,  $A$  is a scaling factor between SERS intensity and fractional surface coverage,  $k$  is the adsorption coefficient indicating the affinity of *p*MA for the Au nanoshell surface, and  $x$  is the total concentration of bound and free *p*MA. The parameters obtained from a least-squares fit to the data were  $A$

$= 11.41 \pm 0.33$  (dimensionless) and  $k = 9.48 \times 10^3 \pm 884$  (1/M), where the errors represent a 95% confidence level from the curve fit and  $R^2 = 0.9925$ . Similar values for binding constants were observed by Gearheart *et al.*, who found that for straight, bent, and kinked duplex DNA adsorbed onto small gold nanoparticles, the respective binding constants were  $11\,000 \pm 1300$ ,  $13\,000 \pm 1400$ , and  $14\,000 \pm 350$  M<sup>-1</sup>.<sup>73</sup> The ability to quantify these data with a Langmuir isotherm shows that a single monolayer of pMA is probed even at high concentrations.

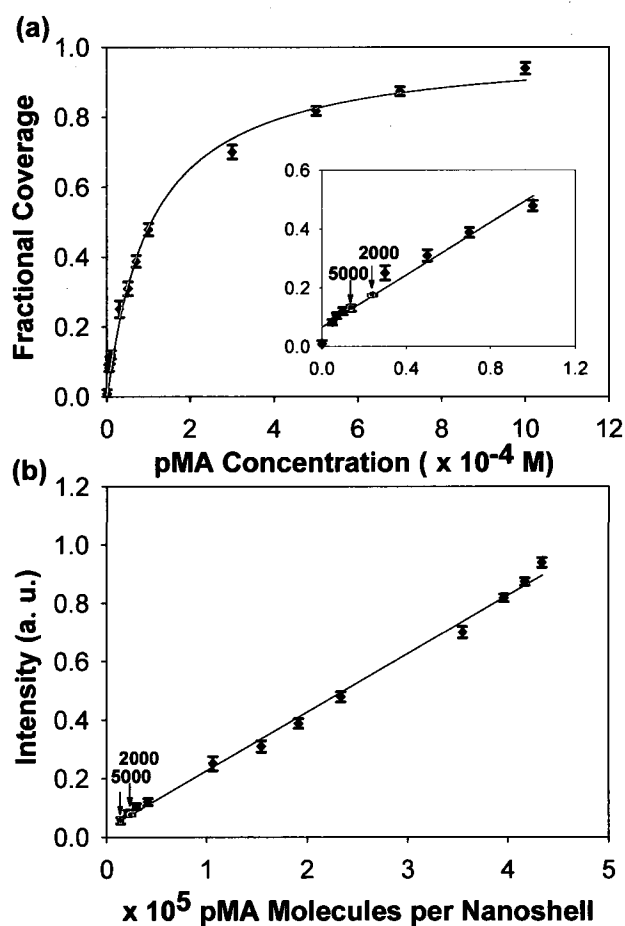


**Figure 2.4:** (a) SERS intensity at 1080 cm<sup>-1</sup> as a function of pMA concentrations (diamonds) and best-fit Langmuir isotherm (line). The inset shows the linear regime. (b) SERS intensity for various amounts of pMA molecules per Au-silica nanoshell.

From the isotherm in Figure 2.4, the number of *p*MA molecules per nanoshell at each concentration can be determined, based on  $188 \pm 28$  nanoshells/laser spot and a  $0.3 \text{ nm}^2/\text{molecule}$  packing density of *p*MA.<sup>60</sup> The concentration-dependent SERS intensity plotted as a function of *p*MA molecules per nanoshell is shown in Figure 2.4b and clearly follows a linear response ( $I = 0.2001a + 0.0277$  with  $R^2 = 0.9947$ ). Error in the *y*-axis indicates the standard deviation from the measurement of three samples. Error in the *x*-axis (not shown) is a result of the error in the pipet, the error in the fit in Figure 2.4a, the error in the calculated surface area of the nanoshell, and the error in the number of nanoshells per laser spot. The linear relationship in Figure 2.4b provides a standard to quantitatively assay the number of PEG molecules present on a nanoshell.

Having calibrated the SERS response of *p*MA molecules adsorbed on Au nanoshells, the packing density of *p*MA-PEG-FI can now be measured. Three samples each of  $1 \text{ }\mu\text{M}$  *p*MA-PEG2000-fluorescein and *p*MA-PEG5000-fluorescein were deposited on the PVP-nanoshell SERS substrates previously described. This concentration was chosen to ensure the formation of a complete SAM. After an 8-h incubation, the Au nanoshells were rinsed twice with MilliQ water (pH 9.1) to remove any unbound molecules. The water-based solvent, borate buffer, was utilized to maintain the pH of the fluorescein and thus keep it in the dianion form.<sup>69</sup> Local conformation of the PEG chain can depend on fragment concentration. When the polymer fragment concentration is increased, water becomes a “poorer solvent”, making the polymer act more hydrophobic.<sup>74</sup> The substrates were allowed to dry, and the SERS spectra were measured. The SERS intensity at  $1080 \text{ cm}^{-1}$  evaluated by interpolation of the plot in Figure 2.4b indicates a surface coverage of 40 500 molecules/nanoshell for *p*MA-

PEG2000-fluorescein and 13 300 molecules/nanoshell for the *p*MA-PEG5000-fluorescein. Based on the known surface area of the nanoshells used in this experiment, the packing density of the 2000 MW *p*MA-PEG-fluorescein is  $46.7 \pm 20.8$  pmol/cm<sup>2</sup> and  $15.3 \pm 7.9$  pmol/cm<sup>2</sup> for the 5000 MW *p*MA-PEG-fluorescein.

**Table 2.1:** Mushroom and Brush Regime Estimates from Lipid Membrane Studies and Experimental Values of the Number of Molecules Per Nanoshell for a 2000 MW and 5000 MW PEG Linkers<sup>a</sup>

PEG linker	PEG:2000 (pmol/cm <sup>2</sup> )	PEG:5000 (pmol/cm <sup>2</sup> )
estimated packing density for mushroom	3.66	1.18
estimated packing density for brush	34.6	17.3
SERS measurement	$46.7 \pm 20.8$	$15.3 \pm 7.9$

<sup>a</sup> The estimates are based on a nanoshell with an outer radius of 107 nm.

To determine whether the packing densities for PEG on nanoshells obtained in this manner infer either the brush or mushroom conformation, we estimate the theoretical packing densities for PEG on nanoshells based on the previously reported packing densities of PEG grafted onto flat lipid membranes.<sup>59</sup> Assuming a mushroom conformation for a 2000 MW PEG, the Flory radius is 3.8 nm and height is 5.6 nm, whereas for a 5000 MW PEG, the Flory radius is 6.7 nm and height is 11.2 nm. Therefore, in the mushroom conformation, 2000 MW and 5000 MW PEG occupy areas of 45.3 and 141 nm<sup>2</sup>, respectively, and for the brush conformation, 2000 MW and 5000 MW PEG occupy areas of 4.8 and 9.6 nm<sup>2</sup>. Scaling these to the  $3.6 \times 10^4$  nm<sup>2</sup> surface area of the nanoshells used in this experiment, we can compare these estimates directly with the values obtained from our SERS measurements (Table 2.1). From this

comparison we can infer that both the 2000 MW and the 5000 MW PEG adsorbates cover surface areas consistent with the more compact brush conformation, when bound to a nanoshell surface, within experimental error. Interestingly, this is the same conformation reported for these two PEG molecules when grafted onto 2D lipid membranes, a quite different chemical and geometrical environment.<sup>59</sup> Utilizing transmission electron microscopy and thermogravimetric analysis, Wuelfing *et al.* reported that, on a monolayer-protected gold cluster of 2.8 nm, PEG-SH (MW 5000) has a molecular footprint of 0.35 nm<sup>2</sup>.<sup>75</sup> Here, we report a footprint of 10.8 nm<sup>2</sup> (MW 5000); this value lies between the measurements made on small colloid and lipid membranes.

## 2.4: Conclusions

A method for determining molecular conformation of molecules on nanoparticle surfaces, based on quantifying adsorbate coverage on the nanoshell surface using SERS, is demonstrated. It is important to note that the some of the largest sources of error are due to (1) variation in the number of nanoshells sampled per laser spot size (roughly 15%) and (2) the fact that the nanoshells themselves are bound to a substrate, limiting the available surface area per nanoshell, and (3) any discrepancies that may exist between the literature value for *p*MA packing density, evaluated on a crystalline Au surface, and the *p*MA coverage on a multicrystalline Au nanoshell surface. Controlled substrate preparation and redundancy with other analytical techniques may be used to address and quite possibly reduce the error in this measurement approach even further. More specifically, the quantification of PEG layers on nanoparticle surfaces may have wide application in biological analysis, nanostructure architecture, and nanodevice



construction and may assist further experimentalists in the optimization of nanoparticle pegylation protocols for in vivo applications.

## **Chapter 3: SERS response as a function of pH: An all-optical nanoscale pH meter**

### **3.1: Introduction**

The local environment of the analyte can be altered by changing pH, which results in variations in the SERS spectral response. This chapter demonstrates that Au nanoshells with a pH-sensitive molecular adsorbate, *p*-mercaptobenzoic acid (*p*MBA), can function as a standalone, all optical nanoscale pH meter.<sup>76</sup> The local environment of the nanosensor is monitored by the pH-dependent SERS spectra of the *p*MBA molecules. SERS spectra were taken by Sandra W. Bishnoi and Muhammed K. Gheith, application of the locally linear manifold approximation algorithm was performed by Christopher Rozell and Dr. Don Johnson, and Gaussian calculations were performed in collaboration with Dr. Bruce Johnson. Carly Levin participated in sample preparation, spectral analysis, interpretation, and discussion. Reproduced with permission from Bishnoi, S. W.; Rozell, C. J.; Levin, C. S.; Gheith, M. K.; Johnson, B. R.; Johnson, D. H.; Halas, N. J. *Nano Lett.* 2006, 6, 1687-1692. Copyright 2006 American Chemical Society.

The development of active nanostructures, capable of performing a function or executing a specific task, is currently a major focus of research efforts in nanotechnology. One already highly successful nanodevice paradigm is the nanosensor: a designed nanostructure, which, when addressed either optically or electrically, responds by providing information about its local environment through its optical or electrical response. All-optical nanosensors hold exceptional promise as embeddable nanodevices

that could potentially be used to probe a variety of exceedingly complex environments, such as individual living cells or the human body, in a virtually noninvasive manner. Early examples of optically addressable nanosensors are quantum dots and fluorescent nanoparticles, which have been used as passive, beaconlike reporters for marking specific biological structures in imaging applications that can potentially assist medical procedures.<sup>77,78</sup> Metallic nanoparticles, such as nanoshells,<sup>28,29</sup> nanocubes,<sup>79</sup> and nanorods,<sup>80</sup> have also been successfully demonstrated as contrast agents in bioimaging. When designed to elicit an optical resonant response at near-infrared wavelengths, the spectral region of greatest physiological transmissivity, they provide image contrast by increasing the scattered light from their immediate location without the strong absorption and fluorescence encountered when using visible light. Metallic nanoparticles have also been shown to provide a highly localized photothermal heating response sufficient to induce cell death and to induce complete, longterm tumor remission in animal studies.<sup>38</sup>

In addition to passive and active functions, there is a third, “informative” role, for which metallic nanoparticles are particularly well suited, and which enables nanosensor development. Metal nanostructures, when excited on their plasmon resonance, give rise to high-intensity electromagnetic fields at their surfaces, which can be harnessed for chemically specific sensing functionalities. Metallic nanoparticles can be designed to enhance the spectroscopic response of molecules bound to, or in close proximity of, their surfaces, an effect known as surface-enhanced Raman scattering (SERS).<sup>8,48</sup> Detailed local chemical information can be retrieved from the spectrum of the inelastically scattered light from the nanoparticle complex.<sup>81</sup> A more general all optical nanosensing device can be envisioned based on a plasmon-resonant nanoparticle and a physically or

chemically responsive layer of adsorbate molecules, where the local environment of the nanodevice is probed by incident light and the device output is the spectrum of Raman scattered light.

Here, an all-optical nanosensor capable of measuring pH in its local vicinity continuously over the range of 5.80 to 7.60 pH units is reported. The device consists of an Au nanoshell designed to elicit a high-enhancement SERS response as a standalone nanostructure from a layer of adsorbate molecules<sup>42,43</sup> at near-infrared wavelengths. The molecular adsorbate layer consists of *para*-mercaptobenzoic acid (*p*MBA), previously shown to be a molecule with a pH sensitive SERS response.<sup>67,82,83</sup> The fact that the SERS signal of an individual adsorbate-coated nanoshell can be of the same order of magnitude intensity as the SERS signal from an individual nanosphere junction, or “hot spot”<sup>45</sup> is explored so that individual nanostructures can function as standalone nanosensors. It can be shown that the designed structure can function as an optically addressable, robust nanodevice, providing complex yet highly reproducible pH-dependent SERS spectra as the optical output. Because the nanosensor is designed for optimal use with near-infrared excitation and Raman-emission wavelengths, the input and output optical signals of this nanosensor are transmissible through blood and tissue and enabling their potential use in diagnostic applications in living systems. By comparison, pH-sensitive dyes, which also have been pursued as optical sensors, require excitation and emission wavelengths in the visible region of the spectrum greatly restricting their use in living systems, exhibit cell leakage and diffusion which prevents their use for local nanoscale pH measurements, and are unable to provide a continuous signal across a broad pH range.<sup>84</sup> A highly practical and general method was developed for converting the complex pH-dependent SERS

spectral output into a streamlined pH readout while maximally preserving its information content, and thereby the resolution and accuracy, of the nanodevice. By adapting an approach from statistical learning theory (which infers simple statistical structure from large and complex data sets)<sup>85</sup> that reduces the dimensionality of the multispectral data set to a simple device characteristic, the accuracy and resolution of the nanoscale pH “meter” can be assessed. An average accuracy of (0.10 pH units across the working pH range of the device is obtained. In the study reported here, both the working nanodevice and its performance analysis illustrate general approaches that should be broadly applicable in the development of other SERS-based functional nanodevices and in evaluating SERS-based device performance relative to an analogous micro- or macroscopic device.

### **3.2: Experimental**

The nanosensor is illustrated in Figure 3.1. To construct this device, Au nanoshells were fabricated according to protocols reported previously.<sup>28</sup> The nanoshell core and shell dimensions were adjusted so that the plasmon resonance provided a farfield absorbance maximum near 785 nm in H<sub>2</sub>O,  $[r_1, r_2] = [55, 71]$  nm, to provide surface-enhanced Raman scattering enhancement at the 785 nm pump laser wavelength. Au nanoshells were immobilized by depositing a drop of aqueous nanoshells solution onto 3-aminopropyltriethoxysilane (APTES, Aldrich) coated silicon wafer supports (Addison Engineering, Inc.) and allowing the water to evaporate. The electrostatic interaction between the nanoshells and the amine group resulted in dispersed nanoshells bound to the silicon substrate. The anchored nanoshells were exposed to solutions of *p*MBA (Sigma-Aldrich) presolubilized in ethanol then diluted in Milli-Q water

(Millipore) for 1 h, then thoroughly rinsed with Milli-Q water. To measure the pH response, SERS spectra were measured from acidic to basic pH levels. Before acquiring Raman spectra at each pH, the sample was immersed in phosphate-buffered saline (PBS) of pH adjusted to the desired value for 10 min. A Fisher Scientific accumet AP63 portable pH meter was used to adjust the pH of the buffer to an accuracy of 0.01 pH units. Raman spectra were then recorded while the entire substrate was immersed in ambient buffer solution using a Renishaw inVia Raman microscope (Renishaw, U.K.) with 785 nm wavelength excitation and 55  $\mu\text{W}$  power at the sample. Backscattered light was collected using a 63x water immersion lens (Leica, Germany), and high-resolution spectra were acquired using a 30-s integration time. Scans were collected from various spots on each silicon wafer, at each pH value. Between the Raman scans at different pH levels, samples were rinsed with Milli-Q water and incubated, for 10 min, in fresh buffer at the new pH.

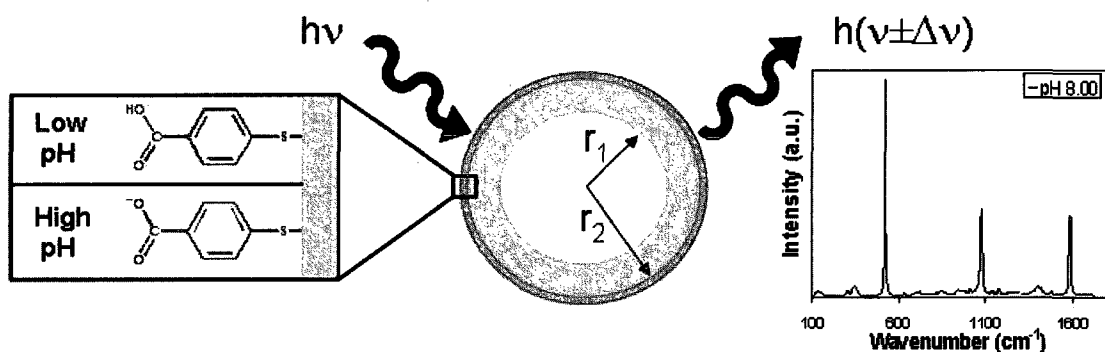


**Figure 3.1:** Schematic diagram of the Au nanoshell pH sensor, consisting of nanoshells with core radius  $r_1=55$  nm and total nanoparticle radius  $r_2=71$  nm and an adsorbed monolayer of *para*-mercaptobenzoic acid. The pMBA molecules yield a pH dependent SERS spectrum.

### 3.2: Results and discussion

Varying the pH of the nanodevice causes reproducible changes in the SERS spectra. SERS spectra were obtained as a function of pH, ranging from pH 4.00 to pH 9.00 (Figure 3.2A). The prominent Stokes features, appearing at  $1077\text{ cm}^{-1}$  and  $1590\text{ cm}^{-1}$ , are assigned to the ring breathing and axial deformation modes of *p*MBA, respectively.<sup>67</sup> As the pH of the nanoenvironment is changed from pH 4.0 to 9.0, highly reproducible spectral changes are observed in the SERS spectra. The most significant of these changes occurs at  $1702$  and  $1394\text{ cm}^{-1}$ , attributable to the C=O and COO<sup>-</sup> stretching modes of *p*MBA, respectively. By monitoring the ratio of these two peaks, we illustrate that this nanodevice can be cycled repeatedly from pH 4 to 9, where the ratio of the  $1702$  and  $1394\text{ cm}^{-1}$  peaks provides a simple optical readout for low-resolution changes in local pH (Figure 3.2B).

The highly complex changes in the SERS spectrum of this molecule that occur over this large pH range not only provide a great deal of information that can be used in assessing the device resolution but are themselves of intrinsic fundamental interest. *p*MBA is a weak acid,<sup>86,87</sup> and because a reduction in the pK<sub>a</sub> of acid molecules typically occurs upon covalent attachment to metal surfaces,<sup>88,89</sup> it is expected that *p*MBA may still be partially protonated under significantly acidic conditions. The presence of dissociated carboxylate groups at low pH is indicated by the appearance of the broad COO<sup>-</sup> band at  $1393\text{ cm}^{-1}$ , appearing much weaker than the C=O band at  $1702\text{ cm}^{-1}$ . With increasing pH, the number of dissociated carboxylate groups increases, enhancing the vibrational stretching mode of COO<sup>-</sup>, resulting in an increase in mode intensity and a shift of the  $1393\text{ cm}^{-1}$  mode to higher wavenumbers. However, even at pH 9, the COO<sup>-</sup> band remains

broad, suggesting that some *p*MBA molecules may still be involved in hydrogen bonding in addition to the possible interaction between COO<sup>-</sup> groups and the ring hydrogens. The low-energy shoulder of the carbonyl mode at 1702 cm<sup>-1</sup>, occurring most strongly at low pH, indicates that some *p*MBA molecules might be participating in intramonolayer hydrogen bonding between adjacent *p*MBA molecules and/or between *p*MBA and the solution ambient.

Multiple overlapping features in the broad 1393 cm<sup>-1</sup> COO<sup>-</sup> band are evident at low pH, which may possibly be attributable to hydrogen bonding between protonated and deprotonated carboxylate groups.<sup>90</sup> From Gaussian calculations (DFT/B3LYP level), it can be inferred that such broadening could be caused by possible interactions between the carboxylate groups and the ring hydrogens. Interactions involving the COO<sup>-</sup>, COOH, and the ring hydrogens may be responsible for altering the COO<sup>-</sup> and C=O modes, resulting in the spectral broadening of this mode observed at acidic pH.<sup>91</sup> Other spectral features in the *p*MBA SERS spectrum that also show pH-dependency include the nominally 1137 cm<sup>-1</sup> Stokes mode, predicted to be a CH in-plane bending mode, which undergoes noticeable spectral changes in intensity with increasing pH.<sup>92</sup> The intensity of this weak mode increases with increasing pH, as does the mode appearing at 845 cm<sup>-1</sup>. This latter spectral feature is assigned to COO<sup>-</sup> bending,<sup>67,92</sup> and its spectral behavior closely resembles that of the COO<sup>-</sup> stretching mode at 1393 cm<sup>-1</sup>. The spectral features at 696, 718, and 800 cm<sup>-1</sup> also show pH-dependent changes in intensity. With increasing pH, the intensity of the 696 cm<sup>-1</sup> band gradually decreases and that of the 718 cm<sup>-1</sup> band increases. The 696 cm<sup>-1</sup> mode was assigned in neutral *p*MBA (acidic limit) to a mixture of OCO bending, in-plane ring compression, and C-S stretching. The mode at 718 cm<sup>-1</sup>

was assigned to out-of-plane ring hydrogen wagging. In the basic limit, the deprotonated *p*MBA anion was found to have corresponding modes, only reversed in energy from the case of the protonated molecule. The  $800\text{ cm}^{-1}$  band appears to have a mixed vibrational nature of in-plane ring deformation motion, C-COOH stretching, and COO<sup>-</sup> bending, decreasing with increasing pH. Because the intensity of in-plane ring vibrational modes, such as that of the  $1137\text{ cm}^{-1}$  and  $718\text{ cm}^{-1}$  bands, was seen to increase with increasing pH, it is proposed that the  $800\text{ cm}^{-1}$  band is dominated mainly by the C-COOH stretching vibration.<sup>82,93</sup> Because the 696, 718, and  $1137\text{ cm}^{-1}$  features are all related to the benzene ring of the *p*MBA molecule, the pH-dependent change in the intensity of these bands may be related to the orientation of *p*MBA on the Au nanoshell surface.<sup>66</sup> However, because saturation coverage of *p*MBA was present on the nanoshells, it is expected that the *p*MBA molecules are packed densely on the nanoshell surface in an upright configuration and undergo only minor reorientations with respect to surface normal over the pH range investigated.



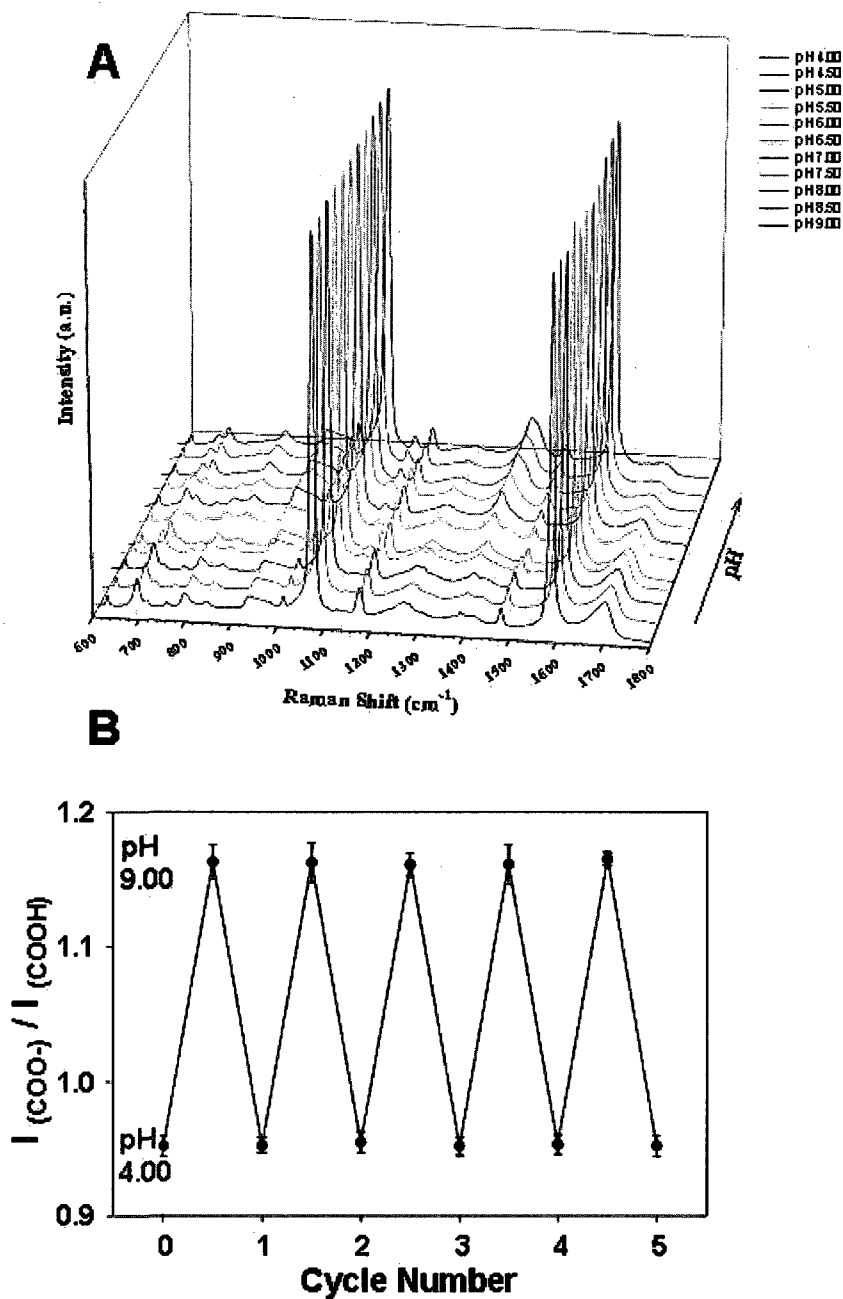


**Figure 3.2:** (A) SERS spectra of *p*MBA on NSs at various pH values ranging from pH 4.00 to pH 9.00 in steps of 0.50 pH units. (B) Repetitive cycling of the Raman pH nanosensor measured by monitoring the change in the  $I(\text{COO}^-)/I(\text{C}=\text{O})$  ( $1702\text{ cm}^{-1}/1393\text{ cm}^{-1}$ ) Stokes modes. The intensities were measured with respect to that of the  $1077\text{ cm}^{-1}$  band to which spectra (at each pH) were normalized. Error bars represent the standard deviation for the measurements.

Transforming a complex data set of pH-dependent SERS spectra into a device whose accuracy can be assessed quantitatively presents an interesting challenge. Clearly, the accuracy of the nanodevice will depend critically on how much pH-dependent information inherently available in the SERS spectra can be accommodated in device analysis. The data displayed in Figure 3.2A demonstrates a large pH range (4.00-9.00) in increments of 0.5 units where the SERS signal is clearly dependent on local pH. However, to test the validity and accuracy of the nanodevice, a finer data set was collected in increments of 0.2 pH units over a narrower pH range (5.80-7.60). This pH range was chosen because of its biological relevance; for example, within this pH range a distinction can be made between acidic cancer cells and healthy tissue.<sup>94</sup> A simple ratio of pH-dependent SERS peaks extracted from the spectral output of the nanodevice (Figure 3.2B) may be used to monitor large changes in pH, but in order to determine the usefulness of such a nanodevice in real applications, it is crucial to obtain a quantitative understanding of the accuracy of its pH measurements across the working pH range of the device.

It is observed that the changes in pH elicit smooth changes in the measured SERS spectrum over this pH range. Each measured spectrum is considered as a point in an  $N$ -dimensional space ( $R^N$ ), where  $N$  is the number of discrete points taken to acquire each SERS spectrum. Each axis in this abstract space indicates Raman frequency, with the value along each axis expressing the spectral energy at that frequency. Varying pH induces spectral changes that trace out a well behaved one-dimensional trajectory in  $R^N$  (parametrized by the pH value) that defines the relationship between the pH and the SERS spectra (Figure 3.3a). If we could exactly parametrize this pH-dependent Raman

curve (more generally known as a manifold), then for a given test sample we could estimate the pH by simply finding the point on the curve closest to the test sample's spectrum. It is very difficult to exactly characterize manifolds in high-dimensional spaces using limited data. Instead, we built a locally linear approximation to the pH-Raman manifold by finding the best collection of straight line segments to fit a collection of training data samples (similar to the locally linear embedding algorithm<sup>95</sup>).

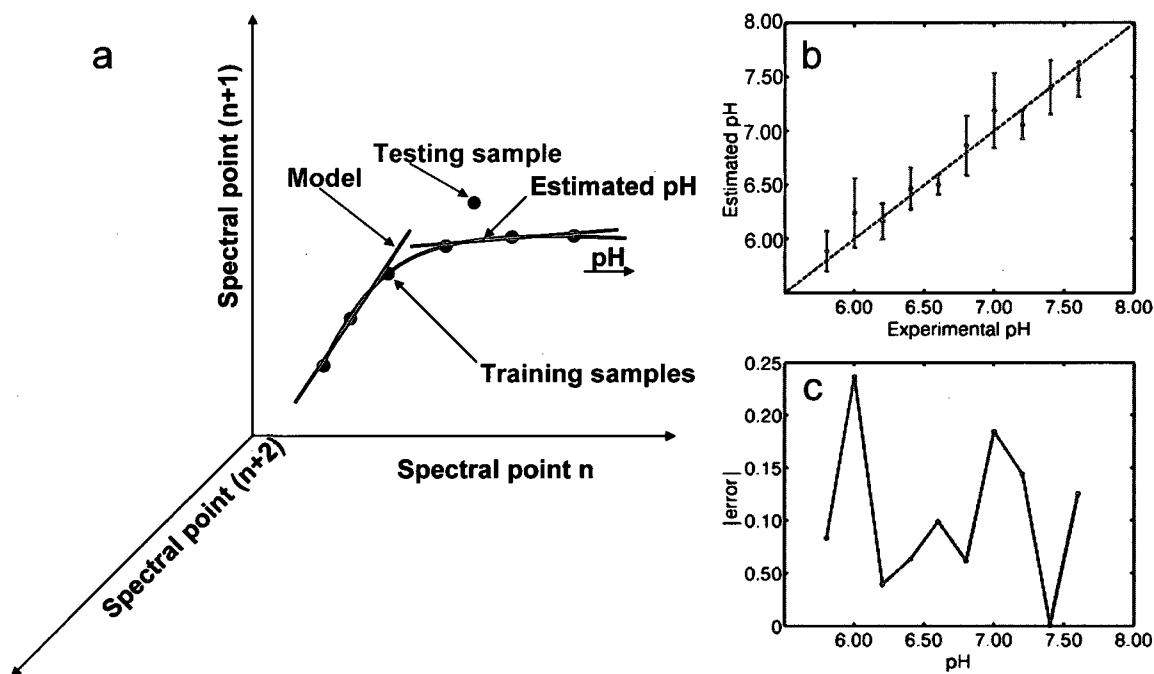


**Figure 3.3:** (a) Spectral changes form a manifold (one-dimensional curve) in  $R^N$  that is indexed by pH, where  $N$  is the number of spectral bands measured. The best piecewise linear fit to the training samples is found using two segments, and that local linear approximation forms a model of the pH manifold. (b) The spectrum of a testing sample is projected onto the model described in a to find the point on the manifold that is closest to the spectrum of the test data. The index of this projected point forms the pH estimate. Cross validation was used to judge the quality of the model (leave one scan out of the model building and then estimate using that scan). The points are the average of the cross validation estimates, and the error bars represent one standard deviation in the cross validation estimates. (c) Magnitude of the average error of the cross validation estimation procedure shown in b. The average error magnitude across the pH range of the device is 0.10 pH.

A series of pH-dependent SERS spectra serves as our “training” data with which we test this parametrization. Each spectrum in this figure was constructed from an average of five SERS spectra taken at the same pH and at different regions on the wafer sample. Because the analysis depends only on the relative intensity at many different Raman frequencies ranging from 600 to 1800  $\text{cm}^{-1}$ , each SERS spectrum is normalized to its value at a specific frequency (1400  $\text{cm}^{-1}$ ). Because the relative changes in peak heights is being examined, it does not matter where the baseline is chosen as long as there is no known contributing signal from the molecule or possible contribution from the silicon substrate. To model the pH-Raman manifold, we then found the piecewise linear curve in  $R^N$  with  $k$  segments that minimizes the mean-squared error over this collection of training data. The  $(k - 1)$  breakpoints were found by exhaustively searching all possible gaps between the training data pH values to find the breakpoints that produce the minimum mean-squared error fit. The best-fitting linear segments were found using a standard least-squares method applied in  $R^N$ . For this device output, a two-segment piecewise linear curve was found to fit the pH manifold with high accuracy and minimal complexity. We then used crossvalidation<sup>96</sup> to judge the variation of our estimation procedure by testing each SERS spectrum against the parametrized manifold (Figure 3.3b). This was accomplished by constructing the pH-Raman manifold model using four of the five available spectra at each pH and testing the variation between the fifth spectrum and the parametrized model. This procedure was repeated five times (leaving each scan out once), and the resulting pH estimates were used to judge the accuracy and precision of the procedure. The magnitude of the average error over the pH range of the device was obtained in this manner (Figure 3.3c). The average error magnitude across the

working pH range is 0.10. However, this varies significantly across the pH range of the device, with a much larger error occurring around pH 6.0 than elsewhere in the pH range being evaluated. The increased error in this specific range is due to an observed increase in spectral fluctuations for the SERS spectra for this specific pH, which is likely to be near the effective  $pK_a$  of the *p*MBA adsorbate molecules. It is quite possible that molecular fluctuations occurring at this pH due to protonation-deprotonation dynamics may give rise to the increased spectral noise observed, which translate to a lower accuracy for our nanodevice at this specific region of its pH range.

The ultimate resolving power of this nanosensor depends partially on the resolution of the training data used to model the pH-Raman manifold. To further explore the resolving power of the nanosensor built with training data at 0.20 pH intervals, the manifold approximation technique is used to estimate the pH of two test samples taken between the training data pH values (having pH values of 6.10 and 7.15). The nanosensor estimated the pH values of these test samples to be 6.47 and 7.01, respectively. For the pH 6.10 test sample, we see an error slightly larger than that predicted by the cross-validation study. As we saw with the training data, the larger error appears in the pH range where increased SERS spectral fluctuations are observed.

### **3.4: Conclusions**

The all-optical nanoscale pH “meter” reported here is likely to be highly useful in a wide range of applications within biology and biomedicine where such a probe may prove to be a useful new tool for research, diagnosis, or monitoring. Embedding the pH sensor inside plant or animal cells or tissues would allow a new way to monitor the complex changes that can occur within living systems at the single-cell or subcellular

level. Examples may include studying the response of plant cells to stress, early-stage monitoring of transplant rejection, or the “optical biopsy” of possibly cancerous lesions or tumors.<sup>97</sup> The analysis method demonstrated here to assess the accuracy of the nanodevices may also be broadly applicable across a family of chemically functional, SERS-based nanodevices that, in principle, could be fabricated on a ever-increasing variety of plasmon-resonant nanoparticle substrates with large local field enhancements at their surfaces.

## **Chapter 4: SERS response as a function of chain length, terminus, and headgroup: SERS of thiolated aliphatic moieties**

### **4.1: Alkanethiols**

#### **4.1.1: Introduction**

Alkanethiols are an analyte system with several parameters which can be varied for spectroscopic investigation. The analyte consists of an aliphatic chain, a chain terminus, and a headgroup portion; all of which can be chemically modified. Here, the use of Au nanoshell substrates to examine the SERS spectra of SAMs of alkanethiols from decanethiol to hexadecanethiol ( $\text{HS}-(\text{CH}_2)_n\text{-H}$ ,  $n = 10\text{-}16$ ) is discussed.<sup>98</sup> These results are significant in that there have been both relatively few analyses on SAMs in the low frequency region and the fact that they demonstrate coupling between the Au-S stretch and higher-order longitudinal acoustic modes of the alkanethiol molecules. All SERS spectra were taken by Carly Levin and theoretical modeling was performed by Dr. Benjamin G. Janesko and Dr. Gustavo Scuseria. Reproduced with permission from Levin, C. S.; Janesko, B. G.; Bardhan, R.; Scuseria, G. E.; Hartgerink, J. D.; Halas, N. J. *Nano Lett.* 2006, 6, 2617-2621. Copyright 2006 American Chemical Society.

Alkanethiols on gold surfaces are the prototypical self-assembled monolayer (SAM) system,<sup>99</sup> utilized extensively in nanoscale science and applications. The structure and energetics of the gold-sulfur interaction has been studied extensively, both experimentally<sup>100-102</sup> and theoretically.<sup>103-108</sup> Surface-enhanced Raman spectroscopy (SERS) is an excellent method for probing this interaction because of the strong field enhancements that can be excited at the molecule-substrate interface. However, despite extensive work on the SERS spectra of alkanethiol SAMs,<sup>109</sup> there have been relatively few analyses in the low frequency region ( $<500\text{ cm}^{-1}$ ) where the Au-S stretch occurs.<sup>110-112</sup> Recent advances in optical filter technology improving suppression of the Rayleigh line, combined with the development of controllable SERS substrates, have presented an opportunity to observe the vibrational modes of alkanethiol SAMs in this low frequency regime.

Au nanoshells have been shown to provide highly controllable SERS substrates. Their plasmon resonances can be tuned to specific wavelengths by varying the nanoshell core and shell dimensions.<sup>28-31</sup> The high-intensity electromagnetic fields at the nanoshell surface that give rise to SERS can also, therefore, be optimized for specific pump laser wavelengths of interest.<sup>42,43</sup> The integrated SERS signal enhancements from nonresonant molecules bound to nanoshells are very large, comparable to those of solid nanoparticle dimers.<sup>16,45</sup>

#### 4.1.2: Experimental

Au nanoshells of core radius 90 nm and shell thickness 17 nm were fabricated according to protocols described previously,<sup>28</sup> and the dimensions were confirmed by scanning electron microscopy (SEM). The nanoshell core and shell dimensions were

adjusted so that the plasmon resonance provided a far-field absorbance maximum near 785 nm in air, to provide surface-enhanced Raman scattering enhancement at the 785 nm pump laser wavelength. Solutions (1 M) of 1-decanethiol (Aldrich 96%), 1-undecanethiol (Aldrich 98%), 1-dodecanethiol (Aldrich  $\geq 98\%$ ), 1-tetradecanethiol (Fluka  $\geq 98\%$ ), 1-pentadecanethiol (Aldrich 98%), and 1-hexadecanethiol (Aldrich 92%) were prepared in absolute ethanol (200 proof, AAPER Alcohol and Chemical Co.), diluted to 100  $\mu\text{M}$  solutions with Au nanoshells in Milli-Q water (Millipore), and allowed to incubate overnight for covalent attachment. The functionalized Au nanoshells were then immobilized onto poly-L-lysine (0.1% w/v in water, Sigma) coated silicon wafer supports (Addison Engineering, Inc.), resulting in dispersed nanoshells bound to the silicon substrate. Ag deposition onto Au nanoshells was achieved following the method of Liu *et al.*,<sup>113</sup> and the samples were immediately capped with 100  $\mu\text{M}$  dodecanethiol to prevent further oxidation of Ag.<sup>114</sup>

SERS spectra were obtained using a Renishaw inVia micro-Raman spectrometer with a 785 nm excitation laser at 8 mW power across the sample with a 30  $\mu\text{m}$  by 3  $\mu\text{m}$  spot size and 20 s integration time. All spectra were acquired in ambient air. Low-frequency SERS spectra from dodecanethiol on Au nanoshells and Ag coated Au nanoshells are presented in Figure 4.5.

#### 4.1.3: Results and discussion

It has long been established that the vibrational spectra of substituted alkanes in solution show a series of low frequency peaks whose frequency varies inversely with chain length.<sup>115</sup> In Figure 4.1A, bulk Raman spectra of liquid alkanethiols are shown, clearly exhibiting this carbon-chain-length dependence in the broad Stokes mode



appearing in the  $200\text{-}300\text{ cm}^{-1}$  range. These spectral features are typically assigned as longitudinal acoustic modes, analogous to the longitudinal vibrations of an elastic rod.<sup>116</sup> They are denoted LAM- $k$ , with  $k$  designating the number of internal vibrational nodes. These features are described well by simple bond polarizability models that treat the  $n$ -carbon molecule as a one-dimensional chain of  $n$  masses.<sup>116,117</sup> For homogeneous alkane chains, only odd- $k$  modes have a nonzero Raman intensity,<sup>116</sup> a selection rule that is lifted for chains with two different end groups.<sup>117,118</sup> Bulk Raman spectra are dominated by the LAM-1 “accordion” mode: the broad peak in the bulk alkanethiol Raman spectra shown in Figure 4.1A is characteristic of the LAM-1 for liquid substituted alkanes.<sup>119</sup>

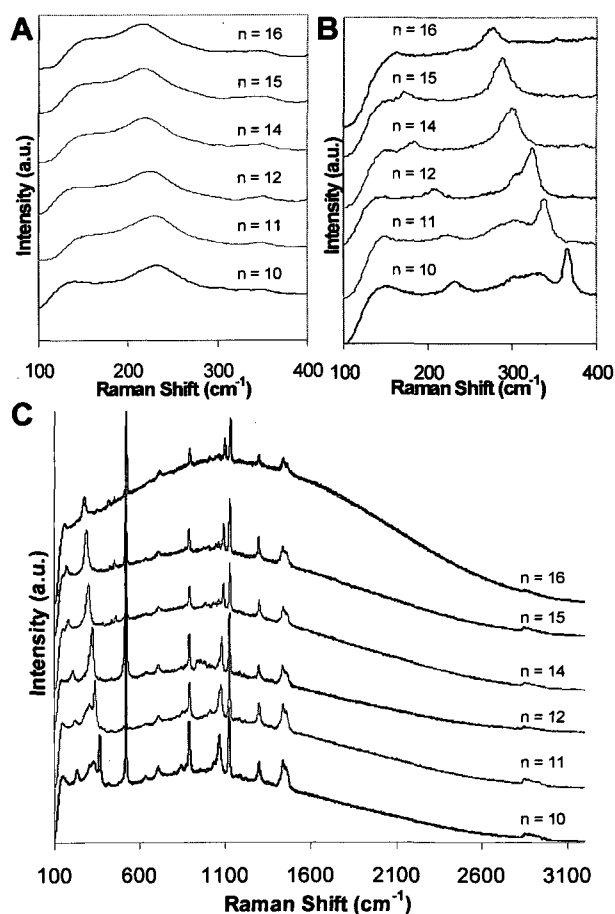


**Figure 4.1:** Experimental unenhanced liquid Raman (A) and SERS (B-C) spectra on Au nanoshells for alkanethiols  $\text{HS}-(\text{CH}_2)_n\text{-H}$ , where  $n = 10\text{-}16$  (offset for clarity).

In contrast to the Raman spectra, the low frequency SERS spectra of alkanethiol SAMs, shown in Figure 4.1B, contain two narrow, well-defined peaks that shift to lower frequencies with increasing chain length. Their intensities are characteristic of a molecule-surface bond, and their frequency shifts are characteristic of the longitudinal acoustic modes of the alkane chain. However, the more intense peak that shifts from 367 to 278  $\text{cm}^{-1}$  is at a significantly higher frequency than either the LAM-1 mode (Figure 4.1A) or previous assignments for the Au-S stretch.<sup>110-112</sup> We propose that these peaks result from coupling between the Au-S stretch and higher-order longitudinal acoustic modes of the alkanethiol molecules composing the SAMs. (The spectra shown here also contain a weak, broad shoulder at 300-350  $\text{cm}^{-1}$  appearing only for the shorter alkane chain lengths. This feature may possibly result from incomplete surface coverage, but definitive assignment is beyond the scope of the present work.)

The alkanethiol SERS spectra above 500  $\text{cm}^{-1}$  (Figure 4.1C) concur with previous assignments for alkanethiol SAMs.<sup>109</sup> The SERS spectra lack the S-H bond stretch at 2580  $\text{cm}^{-1}$  and the H-S-C bending mode at 850  $\text{cm}^{-1}$ , confirming the presence of a SAM on the Au nanoshell surface. The reduced intensities of the C-H stretching peaks (2800  $\text{cm}^{-1}$  to 3000  $\text{cm}^{-1}$ )<sup>120</sup> can be attributed to the decrease in SERS enhancement with increasing Raman shift because of the finite width of the plasmon resonance of SERS substrates.<sup>121</sup> These spectra appear quite similar, with notable differences appearing only in the low frequency region (Figure 4.1B).

To our knowledge, the only previous report of LAM-*k* modes in SERS of molecules on surfaces involved monocarboxylic acids on Ag surfaces.<sup>122</sup> A low

frequency SERS spectrum of palmitic acid ( $\text{HOOC}-(\text{CH}_2)_{15}\text{-H}$ ) on Ag does possess a peak at  $288\text{ cm}^{-1}$ , assigned to a LAM overtone.<sup>123</sup> Coupling to the substrate was not invoked to explain this observation, indeed, the suggested molecular orientation in that system, with the chain axis parallel to the surface,<sup>122</sup> may in fact preclude such coupling.

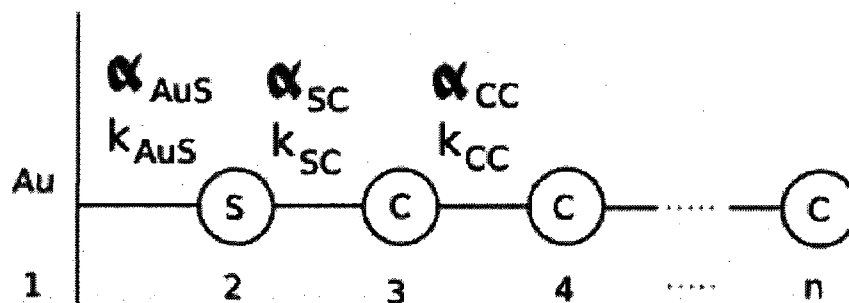


**Figure 4.2:** Schematic of the 1D model of (Au surface)-S-(CH<sub>2</sub>)<sub>n-2</sub>-H self-assembled monolayer.  $k$  and  $\alpha$  are the harmonic force constant and polarizability derivative of each bond.

We modeled the alkanethiol SERS spectra using an extension of the simple bond polarizability picture,<sup>116,117</sup> treating the [Au surface]-S-(CH<sub>2</sub>)<sub>n</sub>-H as a 1D chain of  $n + 1$  atoms attached at one end to an infinitely massive surface site. The model is shown schematically in Figure 4.2. Figure 4.3A presents the theoretical prediction of this model for the alkanethiol SERS spectrum.

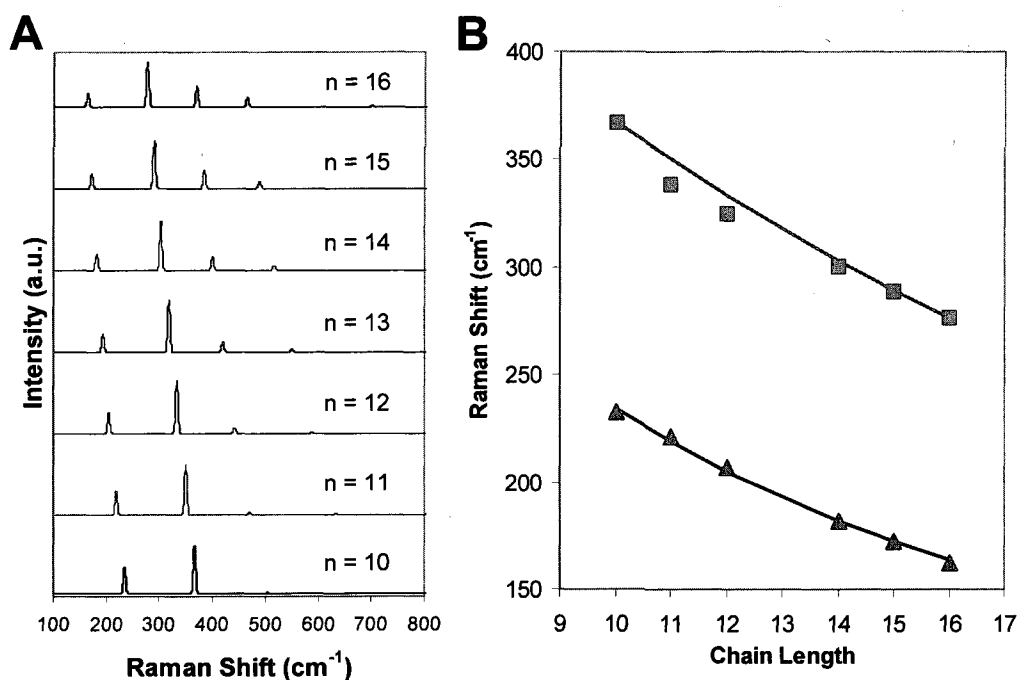


**Figure 4.3:** (A) 1D model results for SERS spectra of (Au surface)-S-(CH<sub>2</sub>)<sub>n</sub>-H, for  $n = 10$  (decanethiol, bottom) to  $n = 16$  (hexadecanethiol, top). Simulated spectra are plotted with a uniform Gaussian broadening of  $10 \text{ cm}^{-1}$ . (B) Frequencies of the two narrow, intense peaks in the Au-S-(CH<sub>2</sub>)<sub>n</sub>-H spectra of Figure 4.1B, plotted as a function of chain length (where for the LAM- $k$  peak frequencies, ▲ is  $k = 1$  and ■ is  $k = 2$  from experiment, and — is  $k = 1$  and — is  $k = 2$  obtained from the 1D model in A).

Despite its simplicity, the 1D model gives remarkably good agreement with experiment. The model gives reasonable qualitative agreement for the predicted SERS intensities (Figure 4.3A) and quantitatively reproduces the frequencies of the two intense low frequency peaks in the experimental SERS spectra (Figure 4.3B). The model also predicts significant intensity in the  $k = 0$  peak, which is near the frequency cutoff of the SERS experiment ( $150 \text{ cm}^{-1}$ ) but may be accessible using other experimental techniques.

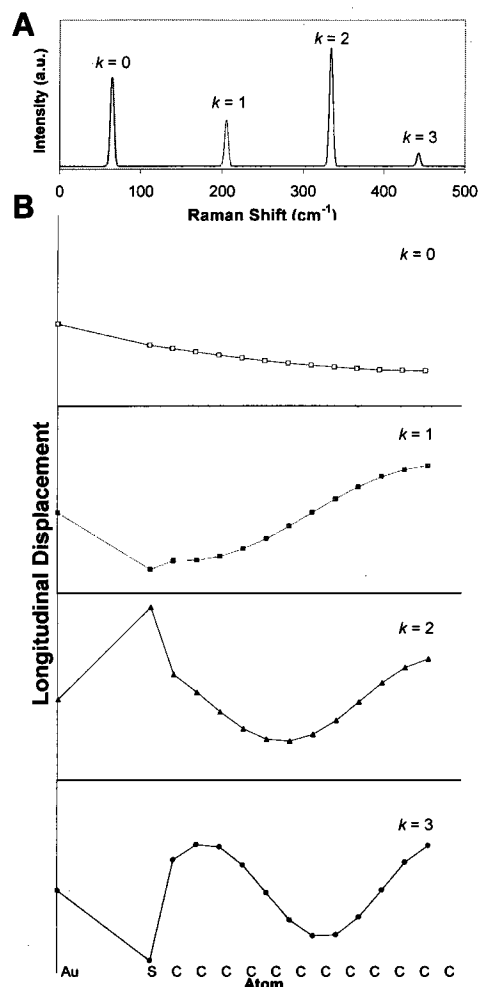


**Figure 4.4:** (A) SERS spectra of (Au surface)-S-(CH<sub>2</sub>)<sub>12</sub>-H, as predicted by the 1D model. The  $x$  axis begins at 0 cm<sup>-1</sup> in order to include the  $k = 0$  mode. (B) Normal-mode eigenvectors for the four vibrational modes shown in part A. The longitudinal displacement of each atom is plotted on the  $y$  axis. The  $k = 0$ ,  $k = 1$ ,  $k = 2$ , and  $k = 3$  modes occur at 74, 226, 373, and 519 cm<sup>-1</sup>, respectively. The Au-S bond stretch is maximized for the modes with  $k = 2$  and  $k = 3$  internal nodes ( $\square$  is  $k = 0$ ,  $\blacksquare$  is  $k = 1$   $\blacktriangle$  is  $k = 2$   $\bullet$  is  $k = 3$ ).

The 1D model predicts that the low frequency peaks in the alkanethiol SERS spectra result from coupling between the low frequency, highly polarizable Au-S bond and the LAM- $k$  modes of the alkane chain. Figure 4.4 shows the vibrational modes predicted by the 1D model for a dodecanethiol SAM ( $n = 12$ ). The largest Au-S stretches (displacements of the sulfur site 1) occur in the modes with 1 and 2 internal nodes (205

and  $333\text{ cm}^{-1}$ , respectively). These vibrational modes will dominate the low frequency SERS spectra when Au-S is the most polarizable bond in the system. This qualitative conclusion is quite robust with respect to the model's parametrization. We note that the LAM-0 mode in Figure 4.4B would have zero intensity for a homogeneous chain with two free ends; indeed, it would merely be a zero-frequency translation of the entire molecule. Fixing one end of the chain gives it both nonzero frequency and intensity.

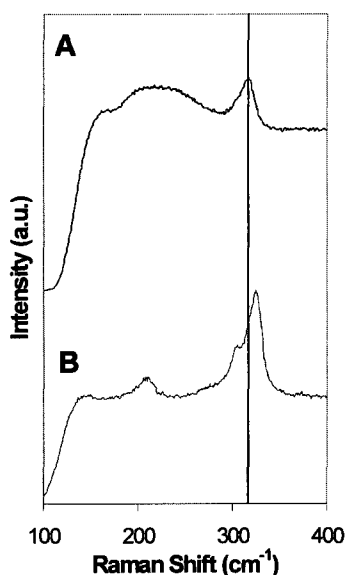


**Figure 4.5:** Experimental low frequency SERS spectra for dodecanethiol on (A) Ag coated Au and (B) Au nanoshells (offset for clarity) with line indicating the peak position shift from  $316\text{ cm}^{-1}$  on Ag coated Au nanoshells to  $326\text{ cm}^{-1}$  for Au nanoshells.

We tested our hypothesis that the experimental SERS peaks include a significant Au-S stretch component by preparing alkanethiol SAMs on Ag versus Au surfaces of nanoshells. The peaks would be expected to have smaller Raman shifts on Ag because of the smaller force constant of the S-Ag bond [methanethiol on Ag (Au) gives a metal-S stretch frequency of  $200\text{ (}279\text{) cm}^{-1}$ , for a predicted force constant of  $0.75\text{ (}1.46\text{) mdyn/\text{Å}}^{110}$ . In the experimental SERS spectrum of dodecanethiol on Au nanoshells, the

most intense low frequency peak appears at  $326\text{ cm}^{-1}$ . This peak indeed shifts to  $316\text{ cm}^{-1}$  for nanoshells with an Ag surface (Figure 4.5). Our 1D model predicts corresponding shifts for SAMs from  $333\text{ cm}^{-1}$  on Au to  $312\text{ cm}^{-1}$  on Ag. The model qualitatively agrees with experiment: the peaks shift to lower frequencies on Ag, and the shift is much smaller than the  $80\text{ cm}^{-1}$  shift seen in the metal-S stretch itself.

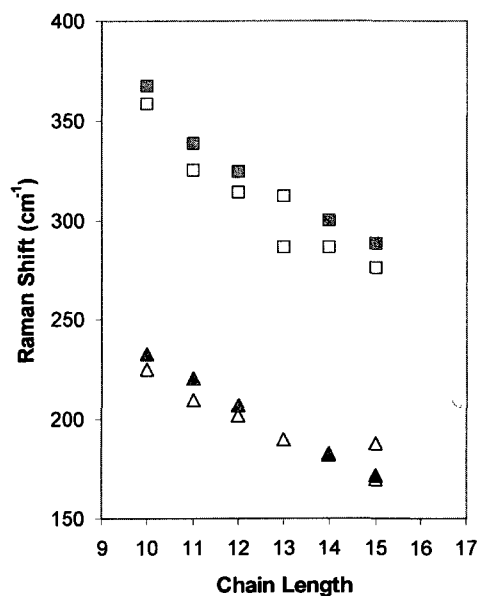


**Figure 4.6:** Results of ab initio electronic structure calculations on  $\text{Au}_3\text{-S-(CH}_2)_n\text{-H}$  (see the text). Frequencies of the two narrow, intense peaks in the  $\text{Au-S-(CH}_2)_n\text{-H}$  spectra (Figure 4.1B), plotted as a function of chain length  $n$  (where for the LAM- $k$  peak frequencies,  $\blacktriangle$  is  $k = 1$  and  $\blacksquare$  is  $k = 2$  from experiment, and  $\triangle$  is  $k = 1$  and  $\square$  is  $k = 2$  obtained from the ab initio calculations).

We also verified the predictions of the semiempirical 1D model with ab initio electronic structure calculations on adatom models of the alkanethiol SAMs. Adatom models treat the Au surface as a cluster of 1-10 Au atoms. Although ab initio calculations generally cannot reproduce experimental SERS intensities, they provide fairly reliable predictions of vibrational frequency shifts.<sup>124-127</sup> We performed PBE1PBE/Lan12DZ calculations on  $\text{Au}_3\text{-S-(CH}_2)_n\text{-H}$ , a single alkanethiol chain attached to a triangle of Au

atoms designed to model the Au(111) surface. Figure 4.6 shows the LAM-1 and LAM-2 vibrational frequencies obtained from the ab initio calculations. The predicted LAM- $k$  frequencies agree quite well with experiment, providing further support for this picture. The ab initio calculations also correct the dispersion relation of the 1D model, giving all of the LAM- $k$  modes below  $520\text{ cm}^{-1}$ . The ab initio calculations predict some spurious coupling to the higher LAM- $k$ , seen in the splitting of the LAM-1 mode for  $n = 15$ . More sophisticated models, including finite temperature, vibrational anharmonicity, and/or interactions between adjacent chains, would be needed to address these discrepancies.

#### 4.1.4: Conclusions

Our observation of coupling between molecule-surface and intramolecular (LAM) vibrational modes in alkanethiol SERS spectra presents a number of interesting avenues for further research. Although such coupling has been reported previously as a source of frequency shifts in SERS of simple molecules,<sup>125,128,129</sup> the example presented here is both novel and strikingly well-resolved. The resulting intense peaks are sensitive to the details of the gold-sulfur headgroup interaction and the local geometry of the group (-S-CH<sub>2</sub>-) mediating the vibrational coupling. SERS measurements of these modes may provide new insight into longstanding controversies over the geometry and energetics of the headgroup interaction.<sup>130</sup> The simple physical model we report here clearly illustrates a mechanism that may be important in the analysis of the SERS spectra of more complex adsorbates, including biomolecules or biologically relevant systems.<sup>7</sup> This previously unreported coupling between the longitudinal acoustic modes and substrate-adsorbate vibrational modes of the molecules of an alkanethiol SAM may be exploitable in



applications, possibly providing a signal transduction mechanism for nanomechanical sensors and actuators.

## 4.2: $\omega$ -terminated alkanethiols: acids, alcohols, and dithiols

### 4.2.1: Introduction

Monolayers formed using  $\omega$ -terminated alkanethiols ( $\text{HS}-(\text{CH}_2)_n\text{-X}$ ) rather than traditional alkanethiols ( $\text{HS}-(\text{CH}_2)_n\text{-CH}_3$ ) may offer advantages provided by their additional functional group (X). These types of organic monolayers allow for more precise engineering of the monolayer properties for various purposes. Asymmetric functionalization of gold nanoparticles using  $\omega$ -terminated alkanethiols (where X was either  $\text{NH}_2$  or  $\text{COOH}$ ) has been used for dimer formation via EDAC coupling.<sup>131</sup> Furthermore, functionalization with  $\text{NH}_2$  or  $\text{COOH}$  terminated alkanethiols is used in the adsorption of proteins.<sup>7</sup>

### 4.2.2: Results and discussion

Varying the chain termination from a simple methyl group (as in alkanethiols) to a carboxylic acid functional group results in slight changes in the Raman spectral response. There are additional peaks at 1412 and 1437, 1631, and 2725  $\text{cm}^{-1}$ , attributable to a symmetric and asymmetric  $\text{CO}_2^-$  stretch, a  $\text{C}=\text{O}$  stretch, and the CHO group, respectively in the unenhanced Raman spectrum of 11-mercaptoundecanoic acid (Figure 4.7A). In the SERS spectrum (Figure 4.7B), the  $\text{C}=\text{O}$  stretch appears weakly at 1657  $\text{cm}^{-1}$ . The weak spectral feature of this peak is not surprising since the nanoshell near-field plasmon bandwidth drops off at higher wavenumber and, while the  $\text{C}=\text{O}$  bond is known to produce strong IR bands (seen in the 1691 - 1710  $\text{cm}^{-1}$  region of Figure 4.7C), it generally shows weak Raman scattering. It should also be noted that the lower order Au-

S/LAM- $k$  modes for 11-mercaptoundecanoic acid appear at 225 and 322  $\text{cm}^{-1}$ .

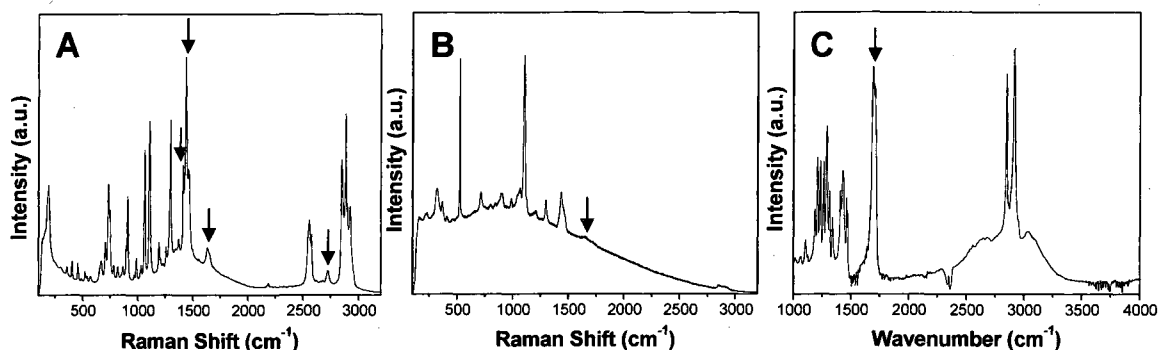


**Figure 4.7:** (A) Unenhanced Raman spectrum (powder, average of 5 scans), (B) SERS spectrum (1 mM, average of 5 scans), and (C) IR spectrum (powder, coaddition of 256 scans, 4  $\text{cm}^{-1}$  resolution) of 11-mercaptoundecanoic acid.

Changing the terminal functional group from a methyl to an alcohol fails to significantly affect the SERS spectrum, since similarly to the C=O peak, the –O-H stretch is IR active and very weak in Raman. In IR, the presence of an –OH group is indicated by a strong, broad band between 3200 and 3400  $\text{cm}^{-1}$ . The SERS spectrum for 11-mercapto-1-undecanol on Au nanoshells did not yield any additional peaks attributable to an –O-H stretch, although SAM formation was confirmed by the appearance of the low order Au-S/LAM- $k$  modes at 221 and 325  $\text{cm}^{-1}$ .

In the SERS spectra of aliphatic dithiols on Au nanoshells (Figure 4.8A), there exists a weak peak at 2575  $\text{cm}^{-1}$  attributed to the –SH stretch from unreacted, free thiols in solution. Since the spectra were obtained on quartz substrates, ruling out any attribution from a silicon phonon mode at 520  $\text{cm}^{-1}$ , the doublet at 510 and 525  $\text{cm}^{-1}$  is assigned to *gauche-gauche* and *trans-gauche* conformations about the C-S bond, which exhibit S-S stretching frequencies between 500 and 520  $\text{cm}^{-1}$  or at 525  $\text{cm}^{-1}$ , respectively.<sup>132-134</sup> These peaks indicate the presence of disulfides and confirm that not all of the S-S bonds dissociate to form Au-S. In fact, at these chain lengths, it is feasible for

either the molecules to assume an extended chain configuration with one end binding to the gold or for the thiols on both ends to coordinate to the gold surface (Figure 4.8B i,ii). Oxidation of the dithiols to disulfides increases the complexity of their adsorption, since for disulfides, either the lone pair on one or both sulfur atoms can coordinate to the gold surface (Figure 4.8B iii,iv). This complexity is shown by the two low frequency peaks that arise at 287 and 295  $\text{cm}^{-1}$  for 1,8 octanedithiol and 1,9 nonanedithiol, respectively. Compared to their monothiol counterparts (where for octanethiol and nonanethiol the Au-S/LAM- $k$  modes appear at 386  $\text{cm}^{-1}$  and 384  $\text{cm}^{-1}$ , respectively) the frequencies of these peaks are lower and broader, such that at low frequency there are no identifiable individual LAM- $k$  modes.

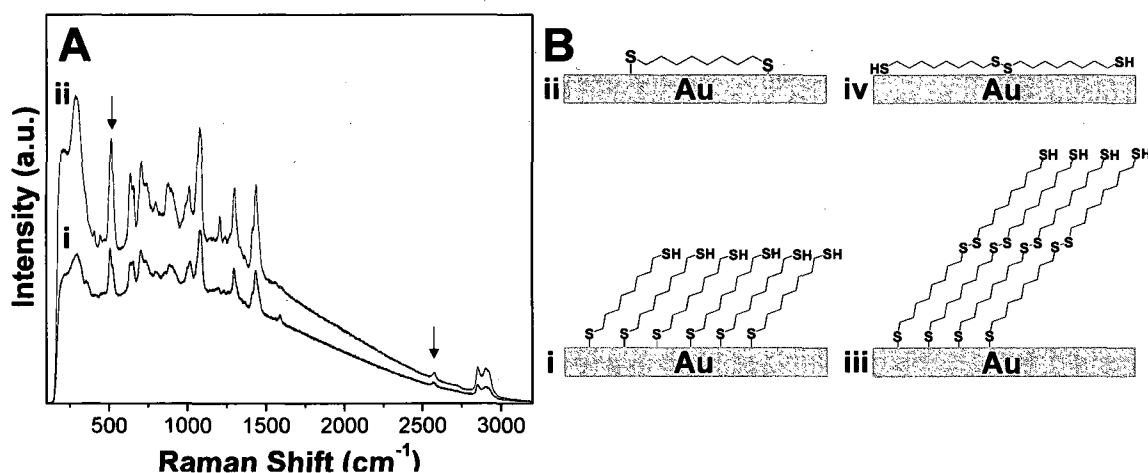


**Figure 4.8:** (A) SERS spectra of (i) 1,9 nonanedithiol (black) and (ii) 1,8 octanedithiol (red) (10 mM, offset for clarity, average of 5 scans). (B) Schematic diagram of the self-assembly process of (1,8) octanedithiol on Au. Different dithiol and disulfide conformations include: (i, iii) an extended chain configuration with one thiol end binding, and (ii, iv) coordination of two or more thiols with the Au surface.

### 4.3: Alkanethiols with a phospholipid headgroup

#### 4.3.1: Introduction

Liposome encapsulation of solid particles is of recent interest for drug delivery,<sup>135</sup> device fabrication,<sup>136</sup> local pH sensing,<sup>137</sup> and trapping of membrane bound molecules.

Compared to polymeric systems, lipids provide the advantage of low toxicity as a result of their physiological lipid composition.<sup>138</sup> Encapsulation of Au nanoparticles inside liposomes allows for a tracer of liposome-cell interactions since Au is an electron dense metal and can be easily seen by microscopic techniques.<sup>139</sup> Additionally, the proximity of the Au metal surface to the membrane and any membrane-bound molecules allows for enhanced detection via the SERS phenomenon.

Previously reported techniques for the encapsulation of hollow gold nanoshells (HGN) within liposomes include an interdigitation-fusion method<sup>140</sup> or by tethering to the liposome membrane with a Au-SH-PEG-lipid linker.<sup>141</sup> In the former method, interdigitated DPPC sheets were mixed with a solution of HGN and heated at 50 °C for 2 hours under vortex mixing, driving the sheets to close around the HGN to form interdigitation-fusion vesicles.<sup>141</sup> In the latter method, DSPE-PEG-NH<sub>2</sub> (MW 2000) was converted to thiol by mixing with 100% excess 2-iminothiolane solution so that the lipid linker could bind to the Au covalently. Liposome encapsulated Au nanoshells have also been synthesized with DPPE-PEG, where, under NIR light, they induce hyperthermia in human mammary carcinoma cells.<sup>142</sup> However, this method for attachment requires centrifuging to separate out any unencapsulated nanoshells and subsequent extrusion through a polycarbonate filter to yield liposomes with a defined pore size.

#### 4.3.2: Results and discussion

Here, the thiolated phospholipid (PL) (1,2-dipalmitoyl-*sn*-glycero-3-phosphothioethanol) (PTE) (Avanti Polar Lipids, Inc., Alabama) is chosen to stabilize the Au nanoshell suspension because of its previous success in coating small colloidal gold nanoparticles<sup>143</sup> through self-assembly without any additional required steps. The

chemical structure of PTE and schematic of nanoshell encapsulation can be found in Figure 4.9. Since the shift in the surface plasmon resonance (SPR) is a function of the refractive index ( $n$ ) at the particle surface, it provides a way to characterize local environment of a nanoparticle. Figure 4.10 shows that when the nanoshells are in an ethanolic solvent ( $n = 1.36$ ) as opposed to water ( $n = 1.22$ ), the SPR redshifts 11 nm. When PTE is added to a solution of Au nanoshells suspended in ethanol and allowed to incubate for covalent attachment, the absorbance spectrum shows a further redshift of 10 nm, indicating functionalization of the nanoshells.

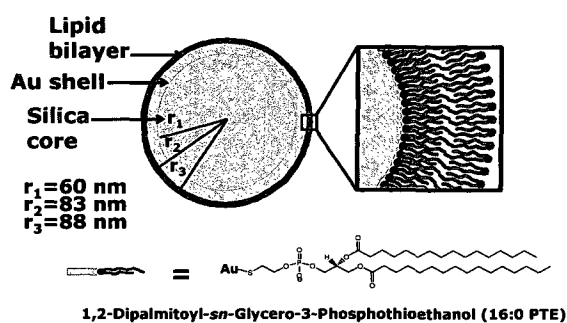


**Figure 4.9:** Schematic of liposome encapsulated nanoshells and chemical structure of 1,2-dipalmitoyl-sn-glycero-3-phosphothio-ethanol (PTE).

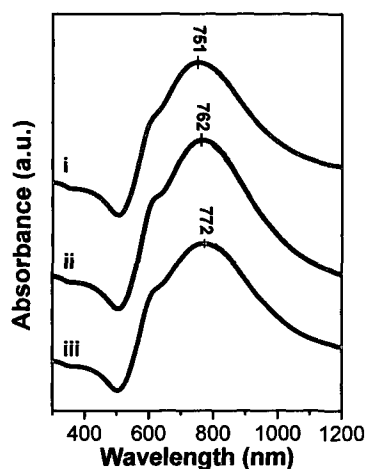


**Figure 4.10:** Extinction spectra of nanoshells  $[r_1, r_2] = [60, 83]$  nm suspended in (i) water  $n = 1.22$ , (ii) ethanol  $n = 1.36$  and (iii) functionalized with PTE lipids and suspended in ethanol (spectra offset for clarity).

There are a few observable spectroscopic differences between the thiolated lipid PTE and an alkanethiol such as hexadecanethiol. The unenhanced Raman spectra of PTE powder and neat hexadecanethiol and their respective SERS spectra on Au nanoshells can be seen in Figure 4.11A,B. For example, the normal Raman of PTE (Fig. 4.11A, ii) shows a C=O stretch found in lipids<sup>144</sup> at  $1733\text{ cm}^{-1}$  that is not present in the hexadecanethiol spectrum (Fig. 4.11A, i). Also, the shoulder around  $800\text{-}950\text{ cm}^{-1}$  in PTE SERS spectrum (Fig. 4.11B, iv) may be attributed to the phosphate O-P-O symmetric and antisymmetric stretch modes from the phospholipid headgroup,<sup>145</sup> as it is known that bands in the  $800\text{ to }900\text{ cm}^{-1}$  region in Raman spectra of phospholipids are due to the headgroup and acyl linkage moieties and are typically weaker than those from the hydrocarbon side chain.<sup>146</sup>

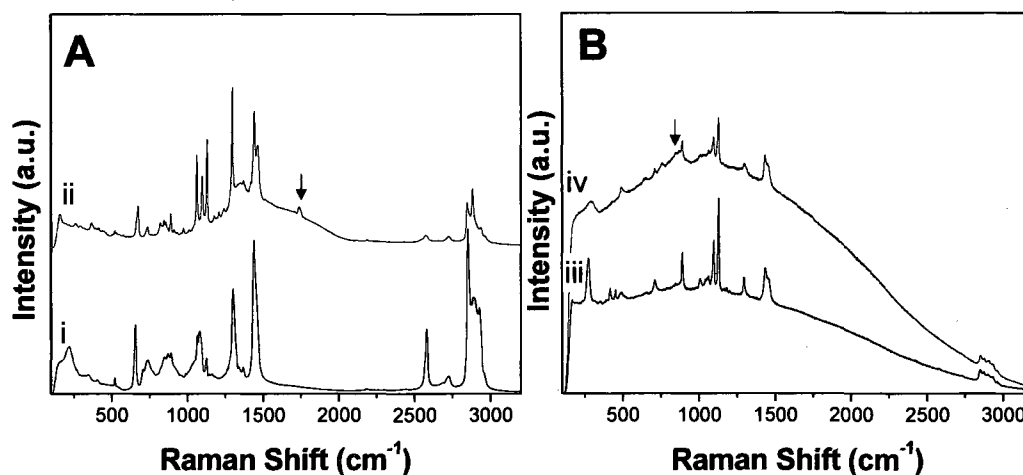


**Figure 4.11:** (A) unenhanced Raman spectra of (i) neat hexadecanethiol and (ii) PTE powder, and (B) SERS spectra of  $100\text{ }\mu\text{M}$  solutions of (iii) hexadecanethiol and (iv) PTE conjugated to Au nanoshells (spectra offset for clarity, average of 5 scans).

The S-H stretches at  $2579\text{ cm}^{-1}$  and  $2582\text{ cm}^{-1}$  in the unenhanced Raman of hexadecanethiol and PTE spectra<sup>109</sup> (Figure 4.11A) are not present in the SERS spectra (Figure 4.11B). Instead the Au-S/LAM-2 modes appear in the SERS spectra of hexadecanethiol and PTE at  $275\text{ cm}^{-1}$  and  $286\text{ cm}^{-1}$  respectively. As expected, the longitudinal acoustic modes (LAM- $k$ ) observed in SERS spectra are weaker and broadened in the lipid spectrum when compared to hexadecanethiol<sup>98</sup>, since the lipids have a  $[-\text{C}_2\text{H}_4\text{-O-PO}_2\text{-O-C}_2\text{H}_4\text{-O-}]$  linker group between the Au-S and  $(\text{CH}_2)_{16}$  groups which almost completely decouples the  $\text{C}_{16}$  LAM- $k$  from the molecule-surface vibration. The SERS spectra (Figure 4.11B) also indicate that while the hexadecanethiol sample is highly ordered on nanoshells, the PTE sample is less ordered due to the gauche to trans ratios of both the C-S and C-C modes. The ratio of the  $(\text{C-S})_{\text{T}}$  to  $(\text{C-S})_{\text{G}}$  (which appear at  $710$  and  $654\text{ cm}^{-1}$  respectively) and of the  $(\text{C-C})_{\text{T}}$  to  $(\text{C-C})_{\text{G}}$  (at  $1127$  and  $1097\text{ cm}^{-1}$ ) in the SERS spectra give values of 1.04 and 1.07 for PTE and 1.21 and 1.28 for hexadecanethiol.

## **Chapter 5: Interactions of ibuprofen with hybrid lipid bilayers probed by complementary surface-enhanced vibrational spectroscopies**

### **5.1: Introduction**

Analyte composition can be further modified by forming a phospholipid layer on top of an underlying SAM of alkanethiols. The phospholipid layer can be utilized to capture and spectroscopically examine intercalant molecules without direct attachment of the molecule to the nanoshell substrate. The work presented in this chapter discusses the formation of hybrid lipid bilayers on nanoshell substrates probed by two surface

enhanced vibrational spectroscopies: SERS and SEIRA.<sup>147</sup> These experimental observations have resulted in the first demonstration of hybrid bilayers on nanoparticle surfaces. Spectroscopic measurements were performed in collaboration with Janardan Kundu. All SERS measurements and analysis were performed by Carly Levin, while the SEIRA measurements and analysis were obtained by Janardan Kundu. Reproduced with permission from Levin, C. S.; Kundu, J.; Janesko, B. G.; Scuseria, G. E.; Raphael, R. M.; Halas, N. J. *J. Phys. Chem. B* 2008, 112, 14168-14175. Copyright 2008. American Chemical Society.

The interactions of amphiphilic molecules, such as nonsteroidal anti-inflammatory drug (NSAIDs), with cellular membranes are biologically important. The clinical use of NSAIDs for their analgesic, antipyretic and anti-inflammatory properties is extremely widespread; however, these compounds cause serious side effects such as gastrointestinal bleeding and peptic ulcer disease.<sup>148</sup> It has been postulated that these side effects occur due to the interaction of amphiphiles with phospholipid layers covering the gastrointestinal mucosa.<sup>149,150</sup> In support of this hypothesis, salicylate has been shown to interact with and change the physicochemical properties of lipid membranes in a way that enhances the formation of membrane pores.<sup>151</sup> Ibuprofen, one of the most heavily prescribed NSAIDs<sup>152</sup>, is known to partition into synthetic and biological membranes and cause changes in the permeability, fluidity, mechanical, and structural properties of the membrane.<sup>150,153</sup> It has been shown using optical-trapping confocal Raman microscopy that ibuprofen causes a high level of disorganization in lipid phosphatidylcholine (PC) acyl chains in a dose-dependent manner.<sup>154</sup>



Recently there has been growing interest in probing biological membrane function by coupling the properties of nanostructured materials with lipid membranes or membrane mimics.<sup>155-158</sup> Hybrid lipid bilayers provide a very important materials system for this approach. They typically consist of an alkanethiol self-assembled monolayer (SAM)<sup>159</sup>, bound to a noble metal substrate, with an associated outer layer of phosphatidylcholine (PC) lipids.<sup>160</sup> Phospholipids with phosphocholine headgroups are known to exist in high abundance within the plasma and intracellular membranes of eukaryotic cells.<sup>161</sup> In a hybrid lipid bilayer, the phospholipid layer assembles onto the SAM with its hydrophobic tail groups directly adjacent to the alkane chains of the SAM, forming a structural analog to the natural lipid bilayer structures found in biological systems.<sup>162</sup> Hybrid bilayers are a good composite system for investigation because they mimic the composition of biological membranes<sup>138</sup> with the additional advantages that they are robust, stable, and can be dried and rehydrated.<sup>163</sup> Additionally, they can be fabricated to cover large surface areas, are easy to form through self-assembly techniques, and have been characterized by a variety of analytical methods.<sup>164</sup>

In this work, hybrid bilayers are assembled onto Au nanoshells, whose plasmon-derived properties allow them to serve as strongly enhancing substrates for both surface enhanced vibrational spectroscopies,<sup>18</sup> surface enhanced Raman scattering (SERS) and surface enhanced infrared absorption spectroscopy (SEIRA). Au nanoshells are spherical nanoparticles consisting of a dielectric (silica) core and a thin metallic (gold) shell.<sup>28</sup> Nanoshells have the unique property that their plasmon resonance can be tuned across a broad region of the optical spectrum by varying the relative dimensions of the core and shell layers of the nanoparticle.<sup>44,165</sup> Surface enhanced spectroscopies require large local

electromagnetic fields at the substrate surface, which are an important characteristic of plasmon-resonant nanoparticles. With nanoshells, the large local electromagnetic field can be resonantly engineered in a frequency range of choice by controlling the internal nanoshell geometry,<sup>43</sup> and by forming small aggregates or arrays.<sup>46,47</sup> For SERS, the single particle plasmon resonance of the substrate is tuned near the frequency of the excitation laser, while for SEIRA, the local fields in the interparticle junctions must be intense across the entire infrared wavelength range over which the molecules will be probed. SERS and SEIRA enhancements observed with nanoshells as the plasmonic substrate are both strong and highly reproducible. By utilizing geometries with closely adjacent nanoshells, both Raman and infrared spectroscopies have been shown to be enhanced simultaneously on the same nanoshell-based substrate.<sup>22,47</sup>

Due to the complementary nature of these vibrational spectroscopies, the combination of both SERS and SEIRA provides a uniquely information-rich method for probing molecular systems at the nanoscale. Specifically, ibuprofen's aromatic ring structure is known to have strong Raman-active modes<sup>166</sup> whereas the polar headgroups of the lipid layer have strong IR-active vibrational modes. By utilizing both SERS and SEIRA, we can spectroscopically monitor both Raman and IR active functional groups of both the intercalant molecules and the hybrid bilayer. These two combined spectroscopies could be potentially used to chemically differentiate between similar analogs of an analyte molecule with high specificity.

Two different effects are thought to contribute to the total enhancement in both SERS and SEIRA: electromagnetic and chemical effects. The electromagnetic contribution consists of the enhancement associated with the local surface plasmon

excitation<sup>167</sup> while the chemical contribution is due to the electronic coupling interactions between the adsorbate molecules and the substrate<sup>168</sup>. These interactions lead to the observed changes in frequency of Stokes modes in SERS when compared to unenhanced Raman spectroscopy.<sup>169</sup> It is interesting to note that in addition to their relevance as a biological mimic, hybrid bilayers and their intercalant species also provide a simple approach for isolating electromagnetic from chemical effects in SERS<sup>170-172</sup>, since the bilayer-intercalated molecules are adjacent to, but not directly interacting with, the substrate surface.

A schematic diagram of the nanoparticle-hybrid bilayer complex is shown in Figure 5.1. The sample geometries consist of (A) ibuprofenate adsorbed onto bare nanoshells for SERS, (B) ibuprofen intercalated in hybrid bilayers for SERS (where the single particle plasmons are utilized), and (C) ibuprofen intercalated in hybrid bilayers on nanoshell aggregates for SEIRA. (Ibuprofenate adsorbed onto nanoshell aggregates for SEIRA is not shown for simplicity).

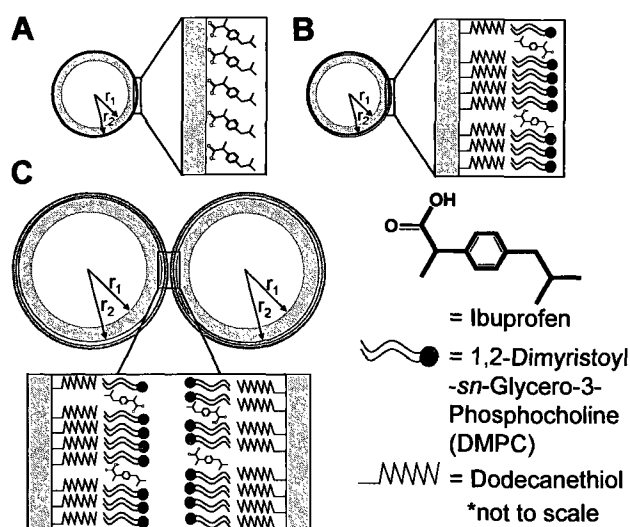


**Figure 5.1:** Schematic illustration of (A) an ibuprofenate functionalized nanoshell and (B) a hybrid bilayer with ibuprofen intercalation on a nanoshell for SERS measurements.

(C) The interparticle junction of two hybrid bilayer nanoshells with ibuprofen intercalation (dimer shown for simplicity) used for SEIRA measurements.

## 5.2: Experimental

Au nanoshells of core radius 60 nm with shell thickness 20 nm and core radius 190 nm with shell thickness 35 nm were fabricated for SERS and SEIRA measurements respectively, according to previously described protocols.<sup>28</sup> The core and shell dimensions of the nanoshells used for SERS were adjusted so that the plasmon resonance provided a near-field enhancement maximum near 785 nm in water, to provide enhancement at the 785 nm pump laser wavelength. The dimensions of the nanoshells used for SEIRA measurements were adjusted to provide a plasmon resonance absorbance maximum in air in the mid-infrared (mid-IR) region: the full SEIRA bandwidth originates from both plasmon-resonant and lightning rod effects.<sup>22</sup> The nanoshell dimensions were then confirmed by scanning electron microscopy (SEM).

The formation of a SAM on Au nanoshells requires the nanoshells to be dispersed in an ethanolic solution of dodecanethiol. The aqueous solutions of  $[r_1, r_2] = [60, 80]$  nm and  $[r_1, r_2] = [190, 125]$  nm nanoshells were centrifuged at 350 RCF for 30 minutes and 90 RCF for 20 minutes, respectively. The particles were then resuspended in absolute ethanol (200 proof, AAPER Alcohol and Chemical Co.).

Alkanethiol monolayers were first prepared on the nanoshells by separately making a solution of 10 mM 1-dodecanethiol (Aldrich  $\geq 98\%$ ) in absolute ethanol. This was diluted to 30  $\mu$ M solutions with the Au nanoshells in ethanol, and allowed to incubate overnight in the dark for covalent attachment. 30  $\mu$ M solutions were chosen based on the nanoshell surface area and concentration, and based on the size of the

dodecanethiol molecule<sup>173</sup> to provide monolayer coverage in ten times excess. After incubation, the nanoshells had settled and the supernatant was removed, so that the nanoshells were redispersed in fresh ethanol and any unreacted thiol was removed from solution. The dodecanethiol functionalized nanoshells were then allowed to dry completely.

For in solution measurements, an initial stock solution of ibuprofen sodium salt was prepared according to Du *et al.*<sup>174</sup> by dissolving ibuprofen (Sigma, USA) in sodium hydroxide (1N, Fisher Scientific) and then adjusting the pH with hydrochloric acid (1N, Fisher Scientific). Since the pKa of ibuprofen is about 4.6,<sup>175</sup> the molecule is predominantly in the ionized form under basic conditions. For the unenhanced powder measurements, the ibuprofen sodium salt utilized was purchased from Sigma.

Lipid solutions of either 1,2-dimyristoyl-sn-glycero-3-phosphocholine (DMPC) or 1,2-Dimyristoyl-D54-sn-Glycerol-3-Phosphocholine-1,1,2,2-D4-N,N,N-trimethyl-D9 (DMPC-D54) (Avanti Polar Lipids, Inc., Alabaster, AL) were prepared by solubilizing the lipids in isopropyl alcohol (Fisher Scientific) (50  $\mu$ L per 2  $\mu$ mol of lipid).<sup>162</sup> The DMPC-D54 lipids and ibuprofen stock solution were added to alkanethiol functionalized nanoshells to give a final concentration of 100  $\mu$ M DMPC lipids and final concentrations of 0.01 mM, 0.1 mM, 1 mM, 10 mM, and 100 mM ibuprofen respectively. The solutions were placed in an ultrasonicator bath (VWR Model 150D) for 30 minutes at 30 °C, above the main phase transition temperature of the DMPC lipid ( $T_m = 24$  °C)<sup>174</sup> and DMPC-D54 lipid ( $T_m = 18.7$  °C)<sup>176</sup> where the lipid is in the liquid crystalline phase and the hydrocarbon chains are more compressible and fluid.<sup>177</sup> All measurements were then performed at room temperature around 22 °C.

The hybrid bilayer phase behavior was characterized using the fluorescent probe Laurdan, following the techniques of Parasassi *et al.*<sup>178,179</sup> Bagatolli *et al.*<sup>180-182</sup> and Zhou *et al.*<sup>183</sup>. For these measurements, an appropriate amount of hybrid bilayers formed with either DMPC-D54 or DMPC were mixed with a methanolic solution of Laurdan (Sigma Aldrich) to achieve a lipid/probe ratio of 300:1. The emission spectra between 400 nm and 600 nm were obtained at a fixed excitation chosen between 320 nm and 390 nm.

SERS substrates consisted of fused quartz (Technical Glass Products, Inc., Painesville Twp., OH), while SEIRA substrates consisted of silicon (Sumco Oregon Corp., Salem, OR). Both substrates were coated with poly(4-vinylpyridine) (PVP). Substrates of this composition combine the advantages of colloidal suspensions and the stability of solid substrates.<sup>54</sup> Cut fused quartz or silicon substrates were first treated with a piranha solution (a concentrated solution of sulfuric acid and hydrogen peroxide) for two hours followed by rinsing with ethanol and drying with nitrogen. Films of poly(4-vinylpyridine) (Aldrich Chemical Company) were deposited by immersing in dilute (0.1%) solutions in absolute ethanol (AAPER Alcohol, Shelbyville, KY) for two hours followed by rinsing with ethanol, drying with nitrogen and were then allowed to cure overnight.<sup>72</sup> The hybrid bilayer ibuprofen solutions were drop dried on the functionalized fused quartz or silicon substrates and then examined with either an inVia Raman microscope (Renishaw) with a 63x water immersion objective after rehydrating the sample at the appropriate pH, or a normal incidence transmission FTIR system (Thermo Nicolet) in air using a liquid nitrogen cooled MCT detector (4 cm<sup>-1</sup> resolution, 256 scans). All IR and SEIRA spectra were background corrected using the Omni software package. Water purified by a Milli-Q water system was used throughout the experiments.

The transmission electron microscopy (TEM) images presented in Figure 5.2 were obtained with a JEM 2010 Cryo-TEM. Excitation generalized polarization spectra were obtained using a JOBIN YVON UV-vis Fluorolog.

### **5.3: Results and discussion**

Representative TEM images for both a bare nanoshell and a hybrid bilayer functionalized nanoshell are shown in Figure 5.2A and 5.2B, respectively. Additional evidence for the formation of hybrid bilayers on nanoshells is demonstrated by the optical image (Figure 5.2C), which shows nanoparticle solubility at various stages of hybrid bilayer formation. Unfunctionalized nanoshells easily disperse in aqueous solvent (Figure 5.2C, i), however, nanoshells functionalized with an alkanethiol are hydrophobic and preferentially disperse in an organic carbon disulfide phase, rather than a water phase (Figure 5.2C, ii). Once a lipid layer self-assembles atop of the alkanethiol, the nanoshells are readily dispersed back into water (Figure 5.2C, iii).

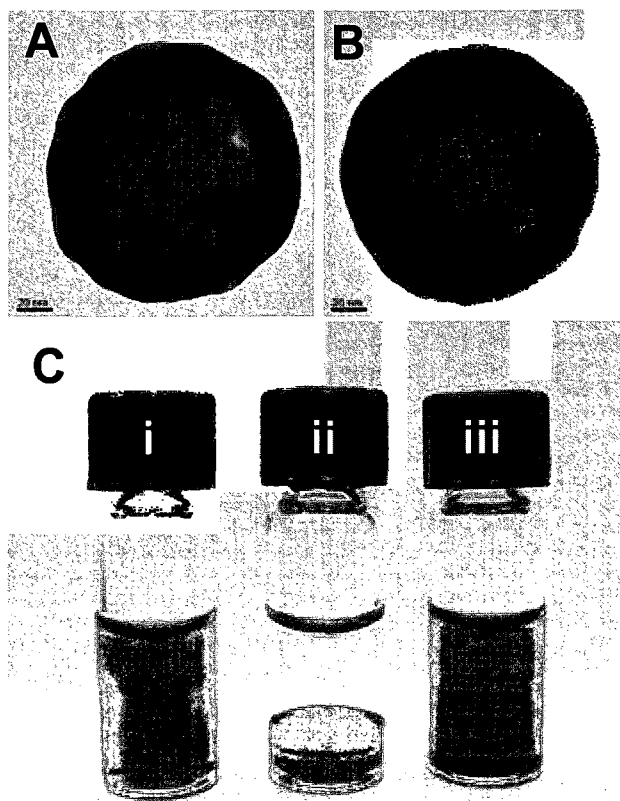


**Figure 5.2:** TEM images of (A) a bare Au nanoshell and (B) hybrid bilayer functionalized Au nanoshells deposited on TEM grids (as shown by the line and contrast in B). (C) Optical images of Au nanoshells (i) dispersed in water, (ii) functionalized with an alkanethiol (which preferentially disperse in an organic carbon disulfide layer on the bottom, rather than the top water layer), and (iii) functionalized with a hybrid lipid bilayer dispersed in water. The scale bars in A, B are 20 nm.

A phase-sensitive fluorescent probe, Laurdan, was utilized to examine possible hybrid bilayer gel-phase characteristics at both pH 3 and 10. Excitation generalized polarization is defined as

$$GP_{ex} = \left( \frac{I_{444} - I_{484}}{I_{444} + I_{484}} \right) \quad \text{Equation 2}$$

where  $I_{444}$  and  $I_{484}$  are fluorescence intensities at 444 and 484 nm, respectively. The excitation generalized polarization spectra ( $GP_{ex}$ ) can be utilized to indicate phase behavior below, near, and above the main phase transition temperatures.<sup>182</sup> The  $GP_{ex}$



spectra for hybrid bilayers with both deuterated DMPC-D54 and nondeuterated DMPC lipids are presented in Figure 5.3. Both deuterated and nondeuterated systems were probed because it has been experimentally observed that deuterating the lipid can lead to an approximate 4-5 degree decrease in the main phase transition temperature<sup>184</sup>. For hybrid bilayers formed using nondeuterated DMPC, the  $GP_{ex}$  spectra show no appreciable tilt either downward or upward, indicating that they are not affected by the excitation wavelength. This evidence suggests that hybrid bilayers formed with nondeuterated DMPC are below the main phase transition temperature and have gel phase characteristics under the employed experimental conditions at both pH 3 and 10. For the deuterated hybrid bilayers, however, a slight downward tilt of the  $GP_{ex}$  spectra is observed for both pH values. Since  $GP_{ex}$  spectra show a downward tilt above the main phase transition temperature, it is reasonable to conclude that under these experimental conditions the deuterated hybrid bilayers reside in a liquid phase. These conclusions are in accord with the established result that the  $T_m$  for a deuterated lipid is lower than its nondeuterated analog.

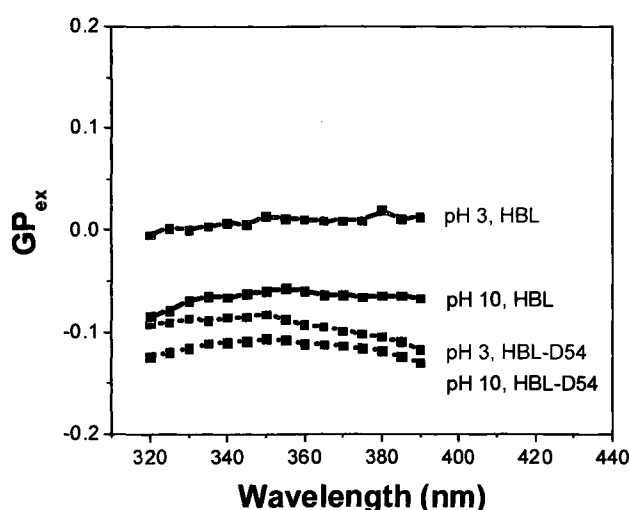


**Figure 5.3:** The excitation generalized polarization ( $GP_{ex}$ ) spectra of hybrid bilayers on nanoshells (HBL) and deuterated hybrid bilayers on nanoshells (HBL-D54) with Laurdan at pH 3 and 10.

Figure 5.4 shows the unenhanced Raman and IR spectra of sodium ibuprofenate along with the SERS and SEIRA spectra of ibuprofenate on bare nanoshells. The enhanced Raman and infrared (IR) spectra of sodium ibuprofenate differ from their respective unenhanced spectra, revealing significant chemical interaction between the molecule and the Au nanoshell surface (Fig. 5.4). The major peaks in the SERS spectrum (Figure 5.4A, iii) are attributable to the sodium ibuprofenate molecule and indicate its interaction with the surface. The intense low wavenumber peak at  $249\text{ cm}^{-1}$  has been assigned to the adsorption of ibuprofenate onto the Au nanoshell surface via the  $\text{COO}^-$  moiety, and arises from the  $\text{CO}_2\text{-Au}$  vibration.<sup>185</sup> Several peaks appear to be shifted in the SERS spectrum with respect to the unenhanced Raman spectrum. For example, the in-plane ring deformation<sup>186</sup> at  $\sim 637\text{ cm}^{-1}$  in the unenhanced spectrum shifts to  $\sim 663\text{ cm}^{-1}$  in the SERS spectrum. The peaks at  $1381$  and  $1579\text{ cm}^{-1}$  in the SERS spectrum can be attributed to the symmetric and asymmetric stretching vibrations of the  $-\text{COO}^-$  group.<sup>187</sup> The presence of the peak at  $1703\text{ cm}^{-1}$  in the SERS spectrum on bare nanoshells is assigned to the  $\text{C}=\text{O}$  stretch. The appearance of these three peaks allows us to infer that not all of the carboxylate groups of ibuprofen are in an ionized state. It is reasonable that both protonated and deprotonated forms of the molecule may be present, since the aqueous nanoshell solution ( $\text{pH} \approx 5.2$ ) to which the ibuprofenate was added was near the  $\text{pK}_a$  of ibuprofen. Additionally, the  $\sim 1185\text{ cm}^{-1}$  and  $\sim 1610\text{ cm}^{-1}$  peaks are relatively intense in the unenhanced Raman but not in the SERS spectrum, which may be due to

conformational variability of the ibuprofenate as it is adsorbed onto the Au nanoshell surface.

Although ibuprofen is a commonly prescribed analgesic, there have been few spectroscopic studies of this molecule in the literature,<sup>186-188</sup> and none reported for sodium ibuprofenate. Also, ibuprofen exhibits a strong IR spectral dependence on its degree of solvation and local environment.<sup>189-193</sup> The SEIRA spectrum (Fig. 5.4B, ii) shows several shifted and enhanced modes of ibuprofenate compared to its unenhanced spectrum. The various in-plane ring modes assigned by Jubert *et al.*<sup>186</sup> and Gordijo *et al.*<sup>187</sup> (at 847, 1090, 1365, 1466, and 1510  $\text{cm}^{-1}$ ) seen in the SEIRA spectra are shifted from their corresponding peak positions in the normal IR spectra. The significantly different spectra obtained for the unenhanced and enhanced Raman and IR cases indicate that both chemical interactions and electromagnetic effects are contributing to both SERS and SEIRA in these studies.

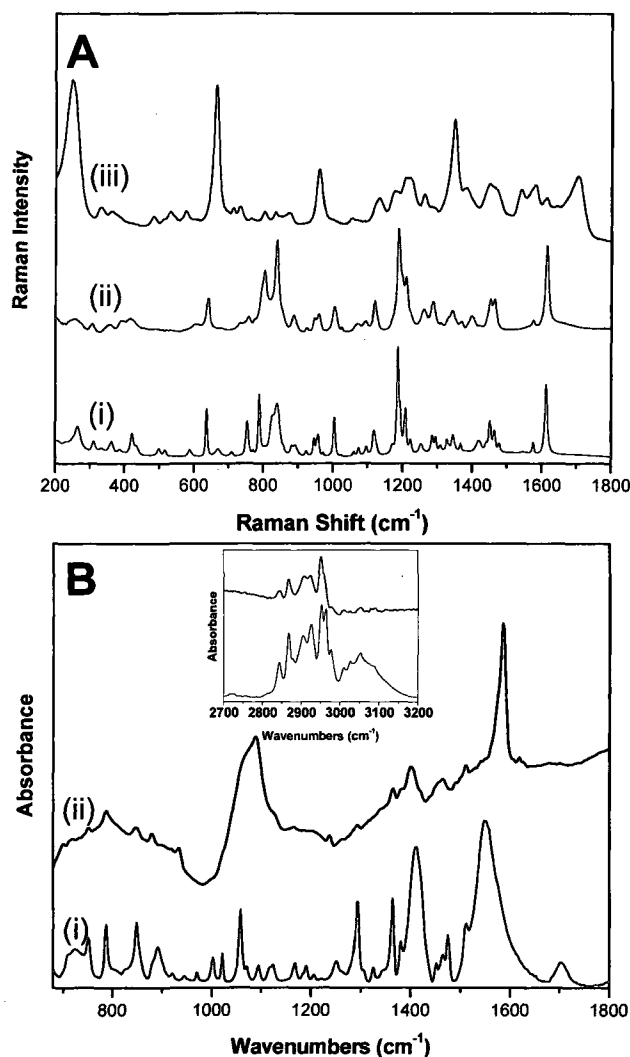


**Figure 5.4:** Raman spectra (A) of (i) ibuprofen sodium salt powder (50x objective, 25.5 mW laser power), (ii) sodium ibuprofenate in aqueous solution (2 M, 63x objective, 40.6 mW laser power), and (iii) surface enhanced Raman spectrum of sodium ibuprofenate (50 mM, 63x objective, 0.144 mW) adsorbed onto Au nanoshells. IR spectra (B) of (i) ibuprofen sodium salt powder and (ii) surface enhanced IR spectrum of sodium ibuprofenate (50 mM) adsorbed onto Au nanoshells (inset shows high frequency regime). (Spectra offset for clarity).

Hybrid bilayer-coated nanoshell substrates using a deuterated lipid (DMPC-D54) were exposed to a range of concentrations of ibuprofen at two different pH values to study its intercalation into the hybrid bilayers using SERS (Fig. 5.5A,B). The pH values three and ten were chosen so that ibuprofen remains predominantly in either the

protonated or deprotonated form. Figure 5.5A,B provides spectral evidence for the deuterated lipid where there are additional peaks that occur due to C-D stretches in the  $2000\text{ cm}^{-1}$  to  $2200\text{ cm}^{-1}$  region. These peaks reveal that the lipid component of the hybrid bilayer is present near the nanoshell surface and allow for spectral segregation of different aspects of the hybrid bilayer system under study. By increasing the ibuprofen concentration at both pH values (Fig. 5.5A,B (ii-vii)), several ring modes of the molecule at  $803$ ,  $1185$ ,  $1205$  and  $1610\text{ cm}^{-1}$  in the SERS spectra were observed to increase in intensity, confirming its presence in the lipid bilayer.<sup>186,194</sup> Figure 5.5C shows the gradual increase of ibuprofen partitioning into the bilayers for both pH values obtained by monitoring the normalized SERS intensity of the strongest mode at  $1610\text{ cm}^{-1}$ . The increase in intensity as a function of ibuprofen loading concentration displays an isotherm-like response. Interestingly, at low pH when the ibuprofen molecule is predominately protonated, the signal from ibuprofen is stronger, allowing for better detection than at high pH. The stronger ibuprofen signal intensity at low pH may result from a change in the hydrophobicity of the molecule. In the protonated form, ibuprofen is anticipated to be more hydrophobic in nature than in the dissociated form. Due to the hydrophobic effect, a decrease in pH may allow for more ibuprofen molecules to intercalate into the hybrid bilayer, increasing their local concentration and in turn, allowing for the ibuprofen molecules to get closer to the hydrophobic acyl chains.

Ibuprofen itself is a known surfactant and has a critical micelle concentration (CMC), above which it can exist in an aggregate, rather than monomeric form. The interactions between ibuprofen and lipids and its toxicity depend on the aggregation pattern of ibuprofen. High concentrations above the CMC for ibuprofen can damage the

integrity of lipid bilayers. While electrochemical studies, such as cyclic voltammetry and impedance spectroscopy, can act as a direct way to examine membrane permeability and integrity,<sup>195</sup> similar studies to characterize pore formation for this system are difficult. The system presented here is unique in that it is the first demonstration of hybrid bilayers on a nanoparticle surface, but the small size of the nanoparticles and the lack of an electrically conductive continuous film of nanoparticles hinder their use as an electrode probe, as finite interparticle separations are imperative for large spectroscopic enhancements. However, the observed gradual decrease in the C-D stretch intensity as a function of increasing ibuprofen concentration (shown in the SERS spectra in Figure 5.5A,B) may provide an indirect indication that hybrid bilayer is being disrupted by the presence of ibuprofen.

Al-Saidan *et al.* has reported a CMC value of 0.83 mM for ibuprofen solutions prepared in aqueous 0.2 M disodium hydrogen phosphate.<sup>196</sup> The 0.1 mM concentration detected at both pH 3 and 10 in the SERS measurements (Figure 5.5) is below the CMC of ibuprofen, and therefore, provides physiologically relevant information on the interaction of ibuprofen and hybrid lipid bilayers in a liquid-crystalline phase, characteristic to that of biologically functional cell membranes<sup>197</sup>.

Unlike the SERS spectra of ibuprofenate on bare nanoshells (Figure 5.4A (iii)), the SERS spectra of intercalated ibuprofen exhibit similar peak positions to the unenhanced Raman spectrum of ibuprofen (Figure 5.5A,B (i)). For example, the 1610  $\text{cm}^{-1}$  mode of ibuprofen, which was not a strong spectral feature in the SERS spectrum of ibuprofenate on nanoshells (Fig. 5.4A (iii)) is clearly visible in the SERS spectrum of the intercalated ibuprofenate (Fig. 5.5 (ii-vii)). Conversely, the spectral features in the 1165-

1230  $\text{cm}^{-1}$  region are intense in the unenhanced Raman (Fig. 5.5A,B i)) and intercalated SERS spectra (Fig. 5.5A,B (ii-vii)), but not in the SERS spectrum of ibuprofenate on bare nanoshells (Fig. 5.4A (iii)). The lack of significant spectral shifts of the ibuprofenate modes in the case of hybrid bilayer intercalation indicates negligible chemical interactions between the ibuprofenate and the nanoshell surface. However, the molecule is nonetheless in close proximity to the nanoshell surface, since strong SERS enhancement is observed.

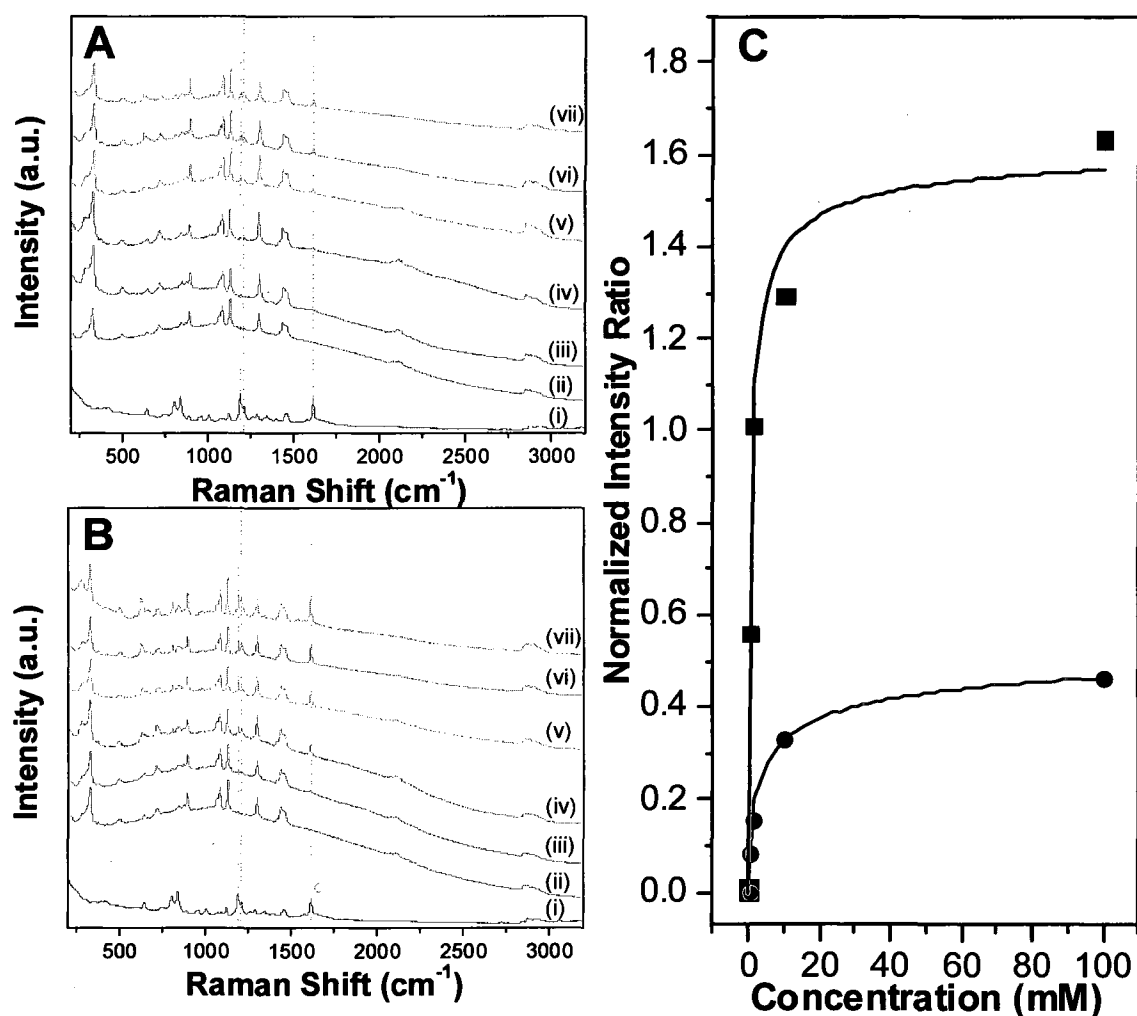


**Figure 5.5:** Raman spectra of (i) ibuprofen in aqueous solution at (A) pH 10 and (B) pH 3 and SERS spectra of hybrid bilayer functionalized nanoshells with deuterated DMPC as a function of ibuprofen concentration: (ii) 0 mM, (iii) 0.01 mM, (iv) 0.1 mM, (v) 1 mM, (vi) 10 mM, and (vii) 100 mM at (A) pH 10 and (B) pH 3. The dashed lines indicate the peaks from clearly identifiable modes of the ibuprofen, indicating its presence in the hybrid bilayer (spectra offset for clarity). (C) Normalized SERS intensity of ibuprofen ring mode ( $I_{1610-1585}/I_{1434-1388}$ ) as a function of ibuprofen concentration in hybrid bilayers at pH 3 (■) and pH 10 (●) with best-fit Langmuir isotherm (lines). The fitting equation and parameters used are  $y = (a*b*x^{(1-c)})/(1+b*x^{(1-c)})$ , where at low pH  $a = 1.64 \pm 0.22$ ,  $b = 1.53 \pm 0.87$ , and  $c = 0.42 \pm 0.21$  and at high pH  $a = 0.57 \pm 0.09$ ,  $b = 0.42 \pm 0.12$ , and  $c = 0.48 \pm 0.11$ .

To test whether the Raman scattering cross section of isolated ibuprofen can account solely for the observed signal strength under these experimental conditions (1.18 mW, 60 seconds integration, 100 mM, Figure 5.6C) the Raman spectra were acquired in solution. The Raman spectrum of 100 mM ibuprofen without nanoshells shows negligible signal, indicating the presence of significant SERS enhancements when nanoshells are utilized as substrates (Fig. 5.5A,B (ii-vii)).



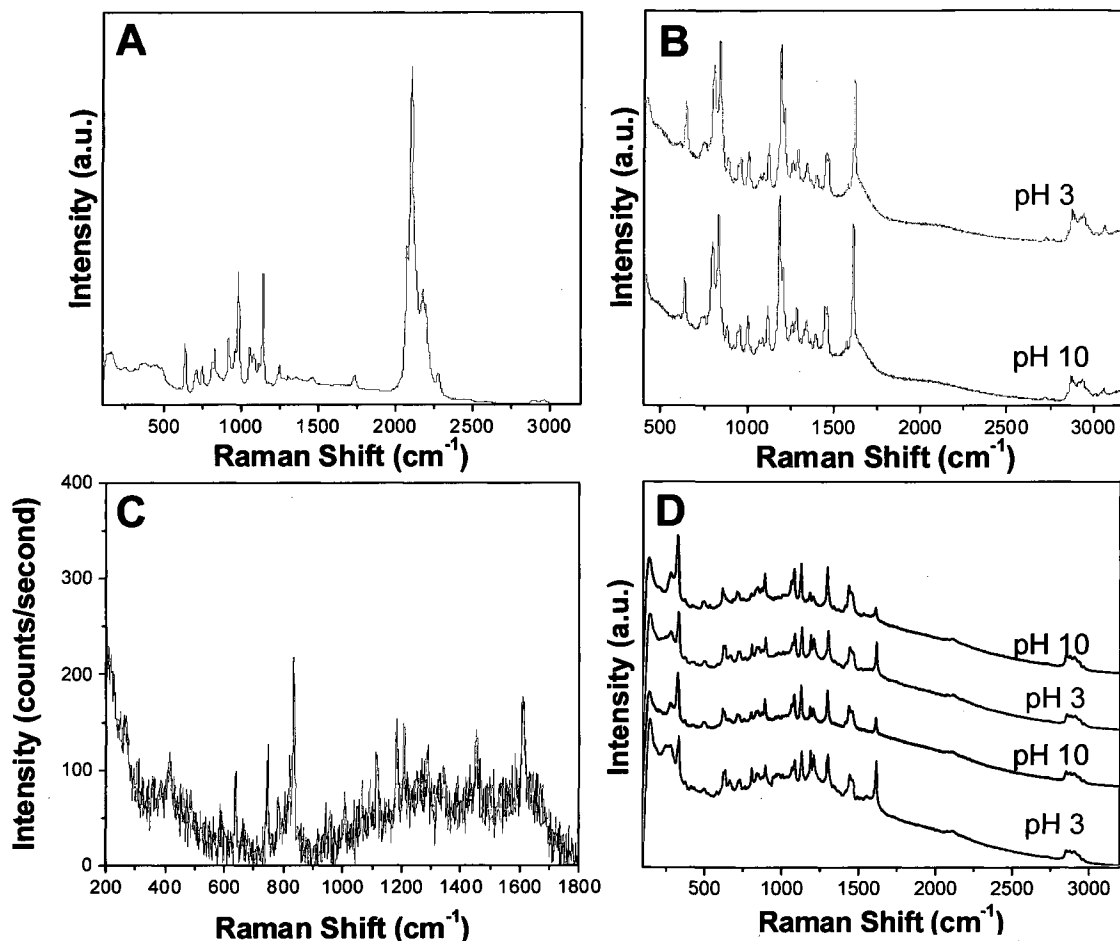


**Figure 5.6:** (A) Unenhanced Raman spectra of deuterated DMPC powder (25.5 mW power). (B) In solution unenhanced Raman spectra of ibuprofen at pH 10 and pH 3 (25.5 mW power, normalized and offset for clarity). (C) In solution unenhanced Raman spectrum of 100 mM ibuprofen at 1.18 mW and 60 second integration time (parameters equivalent to SERS measurements obtained in Figure 4). This demonstrates that electromagnetic enhancement is responsible for the observed SERS signal strength. (D) SERS spectra acquired sequentially at the same sample spot for hybrid bilayer functionalized nanoshells with deuterated DMPC and 1 mM ibuprofen for pH values cycled between 3 and 10 (spectra offset for clarity).

SEIRA provides a means to spectrally observe the effects of ibuprofen intercalation on the DMPC lipid portion (chemical structure shown in Fig. 5.7A) of the hybrid bilayer structure. Figure 5.7B (i) shows the normal incidence transmission SEIRA spectrum of hybrid bilayers on Au nanoshells. The IR absorption peaks of the hybrid bilayer are identifiable at various frequencies and are listed in Table 5.1. The methyl

symmetric and asymmetric bending modes at  $1375\text{ cm}^{-1}$  and  $1462\text{ cm}^{-1}$ , characterizing the aliphatic part of the hybrid bilayer, are all easily observable. The zwitterionic, polar headgroup of the hybrid bilayer also presents characteristic peaks (see Table 5.1). The symmetric and asymmetric  $\text{PO}_2^-$  stretches, the symmetric and asymmetric  $\text{N}(\text{CH}_3)_3^+$  stretches, and the phosphate skeletal vibration (CO-P-O-C stretch) are also all clearly observable in the SEIRA spectrum. The asymmetric CO-O-C stretch and the ester carbonyls (primary and secondary) of the lipid appear as strong features.<sup>194,198-200</sup>

Figure 5.7B (ii, iii) shows the normal incidence transmission SEIRA spectra of ibuprofen intercalated into hybrid bilayers at ibuprofen loading concentrations of 200 mM and 500 mM, respectively. In these two spectra one can observe significant differences between the SEIRA spectra of hybrid bilayers (Fig. 5.7B (i)) and ibuprofen intercalated bilayers (Fig. 5.7B (ii, iii)). The SEIRA spectra of intercalated hybrid bilayers have molecular peaks from the hybrid bilayer with additional distinct peaks attributable to the ibuprofen intercalant (Table 5.2). Various ring modes of ibuprofen are clearly seen at  $847$ ,  $1361$ ,  $1400$ , and  $1510\text{ cm}^{-1}$ . These modes grow in intensity as the concentration of the ibuprofen loading solution is increased. An asymmetric  $\text{CO}_2^-$  stretch is observable at  $1582\text{ cm}^{-1}$  and a carbonyl peak around  $1730\text{-}1740\text{ cm}^{-1}$ . The presence of the asymmetric carboxylate peak can be solely attributed to the deprotonated form of ibuprofen, since the lipid itself has a ketone rather than a carboxylate moiety. The carbonyl stretching peak, however, can be attributed to both the protonated form of ibuprofen and the lipid structure. Therefore, the presence of a protonated form of ibuprofen in the hybrid bilayers cannot be ruled out in addition to a deprotonated form interacting with the lipid. It is expected that the presence of ibuprofen would cause

changes in the packing and ordering of DMPC molecules. In fact, it causes several peaks of the hybrid bilayer system to shift when compared to the case of nonintercalated bilayers. The presence of ibuprofen is observed to primarily affect the peaks arising from the acyl linkage (CO-O) and the polar phosphocholine headgroup of the hybrid bilayer. Symmetric and asymmetric CO-C stretches have undergone a shift in the peak position from 1067 to 1057  $\text{cm}^{-1}$  and from 1175 to 1167  $\text{cm}^{-1}$ , respectively. The ester carbonyl group develops a more prominent double peak structure in the intercalated system, and the symmetric phosphate stretching mode band also undergoes a slight but readily observable broadening. These spectral changes may arise from alterations in the local chemical environment of the lipid molecules when ibuprofen is present. For example, ibuprofen may change the conformational freedom of the lipid headgroups and/or disrupt the spatial packing of the lipids. Since the observed spectral peak shifts appear primarily for the functional groups in the polar headgroup and the backbone portion of the lipid, these results indicate that the interaction of predominantly ionized ibuprofen in hybrid bilayers takes place primarily at the zwitterionic polar headgroup and acyl chain region of the lipid.

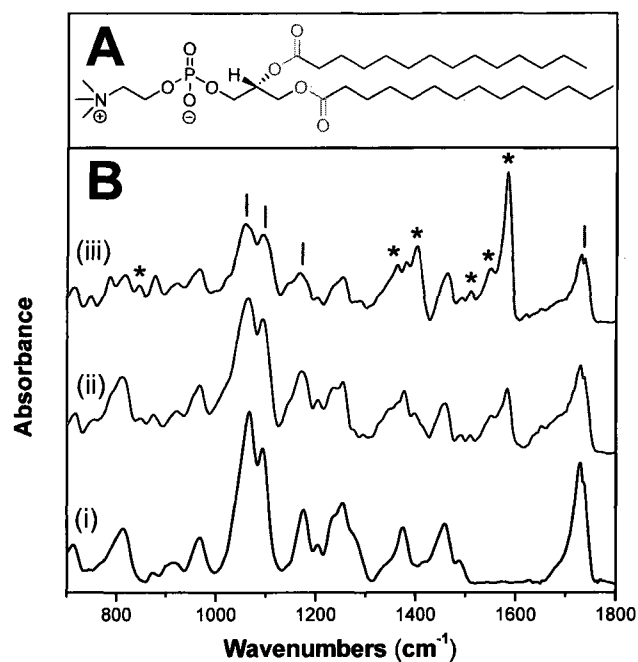


**Figure 5.5:** (A) Chemical structure of 1,2-Dimyristoyl-*sn*-Glycero-3-Phosphocholine (DMPC) highlighting the phosphate and acyl linkage groups. (B) SEIRA spectra for (i) hybrid bilayers (30  $\mu\text{M}$  dodecanethiol with 100  $\mu\text{M}$  DMPC lipids), (ii) hybrid bilayers with 200 mM, and (iii) hybrid bilayers with 500 mM ibuprofenate loading solution. The stars indicate the peaks from clearly identifiable modes of the ibuprofenate, indicating its presence in the hybrid bilayer. The lines indicate DMPC modes (spectra are offset for clarity).

**Table 5.1:** IR Peak Assignments for Hybrid Bilayers on Au Nanoshells<sup>194,198-200</sup>

Wavenumbers (cm <sup>-1</sup> )	Band assignment
1740, 1730	C=O stretch (primary, secondary)
1462	CH <sub>2</sub> scissor, Methyl asymmetric bend
1375	Methyl symmetric bend
1236	Asymmetric PO <sub>2</sub> <sup>-</sup> stretch
1175	Asymmetric CO-O-C stretch
1094	Symmetric PO <sub>2</sub> <sup>-</sup> stretch
1067	CO-P-O-C stretch
966	Asymmetric N(CH <sub>3</sub> ) <sub>3</sub> <sup>+</sup> stretch
920	Symmetric N(CH <sub>3</sub> ) <sub>3</sub> <sup>+</sup> stretch
871	Methyl rock
812	CH <sub>2</sub> rock-twist
714	C-S stretch, Methylene rocking-twisting

**Table 5.2:** IR Peak Assignments for Ibuprofen<sup>186,187</sup>

Wavenumbers (cm <sup>-1</sup> )	Band assignment
847, 1361, 1400	C4-C6 ring stretch, in plane CH ring bend, CH bend
1510, 1549	Ring vibration
1582	Asymmetric CO <sub>2</sub> <sup>-</sup> stretch

In summary, based on the following observations we can conclude that ibuprofen is most likely interacting with the lipid portion of the bilayer rather than the alkanethiol layer. First, the SERS spectra (Fig. 5.5A (ii-vii)) indicate that with increasing ibuprofen concentration in the hybrid bilayer, the trans carbon-sulfur stretch ( $\nu(\text{C-S})_{\text{T}}$ ) at 710 cm<sup>-1</sup> remains significantly stronger than the gauche carbon-sulfur stretch ( $\nu(\text{C-S})_{\text{G}}$ ) at 638 cm<sup>-1</sup>.<sup>109</sup> Second, the low-wavenumber peak at 324 cm<sup>-1</sup>, which corresponds to coupling between the gold-sulfur stretch and the longitudinal acoustic modes of the alkane chain, does not shift in frequency with increasing ibuprofen concentration.<sup>98</sup> Ibuprofen intercalation into the alkanethiol layer would disorder the alkane chain packing, a disorder that would likely shift the longitudinal acoustic mode frequencies<sup>201</sup>. These aforementioned observations indicate that the underlying alkanethiol layer remains ordered and largely unperturbed. Third, as discussed earlier, the SEIRA data (Fig. 5.7B) show significant differences in the peak positions of the lipid headgroup and acyl chain when predominately ionized ibuprofen is present in the bilayers, indicating that ibuprofenate is affecting the outer leaflet of the hybrid bilayer with a greater impact on the headgroup portion of lipid. Fourth, since the lipid headgroup is zwitterionic, when the ibuprofen is in an ionized form, it is certainly plausible for there to be electrostatic interactions between the ibuprofenate and the DMPC near the headgroup. And finally,

while the SEIRA data suggests that it is the predominantly ionized state which shows an association with the headgroup and acyl region, the SERS data indicates that the hydrophobic effect dominates for intercalation of the protonated form. Together, these two experimental findings provide a more complete picture of ibuprofen interacting with and intercalating in hybrid lipid bilayers.

#### **5.4: Conclusions**

We reported a study of ibuprofen intercalation into a hybrid bilayer structure, a membrane mimic system, using surface enhanced vibrational spectroscopies. The spectral features of ibuprofen appearing in the pH dependent SERS spectra indicate incorporation of the analyte into the bilayer. Stronger SERS signals of ibuprofen are observed at low pH, where hydrophobicity of the molecule plays a dominant role in its intercalation. Shifts in the lipid peak positions upon ibuprofen intercalation in the SEIRA spectra reveal that the headgroup portion of the lipid structure has been affected, indicating that predominantly deprotonated form interacts near the interfacial region of the hybrid bilayer. The spectroscopic results combined from SERS and SEIRA studies provide chemical insight into the nature of ibuprofen-lipid interactions and have clinical importance in understanding the effects of NSAIDs on the integrity and permeability of the gastric mucosal membrane. The plasmonic nanostructures utilized in these studies are applicable for spectroscopic investigation of other biologically relevant phenomena in membrane mimics, such as the effect of cholesterol on membrane fluidity, the role of glycolipids in membrane structure, and the binding of peripheral membrane proteins.

## Chapter 6: SERS of non-thiolated moieties

### 6.1: Au-halide complexes

#### 6.1.1: Introduction

Low frequency SERS spectra from metal-solution interfaces can also be obtained to gain insight into other types of metal-adsorbate bonding, such as Au-halogen bonding. In fact, it was the formation of halide complexes on gold electrodes that provided the first clear evidence that chemical interaction between an adsorbate and substrate is an important prerequisite for large SERS enhancement.<sup>202</sup> A clear understanding of halogen adsorption on Au is essential as these anions are frequently introduced into a system as an electrolyte solution to alter pH and/or ionic strength. Their addition can often lead to the misassignment of peaks in low frequency SERS spectra.<sup>203</sup>

It is known that gold-halide complexes have large stability (formation) constants which indicate the strong affinity of halide ions for the gold surface. Both Au(I) and Au(III) are known as B-type metal ions (where the stability of their complexes tends to decrease with increasing electronegativity of the ligand donor atom) so that the order of stability for the halogens on Au is  $I^- > Br^- > Cl^- > F^-$ .<sup>204</sup> For the case of halide chemisorption at a Au(111) surface, the polarity of the bond with Au is a function of the charge on the metal, where the bond is more polar at the negatively charged surface than at a positively charged one. This leads to an asymmetric adsorption behavior with respect to the charge on the metal.<sup>205</sup> Therefore, the surface charge on the Au substrate should be taken into consideration when conducting SERS measurements.

### 6.1.2: Results and discussion

Several halogen containing molecules have been shown to chemisorb onto dialyzed nanoshells demonstrated by their SERS response, as shown in Figure 6.1. Dialyzed nanoshells were used to eliminate any extra adsorbed species on the surface of the nanoshells. No SERS bands were experimentally observed on Au nanoshells for fluoride containing molecules, consistent with the work of Gao and Weaver and the anion's extremely weak adsorbing properties,<sup>91</sup> resulting from its high electronegativity. The experimentally observed frequencies of the Au-halide stretching vibrations decrease from chloride to bromide to iodide, and the peak width narrows. SERS spectra (Fig. 6.1) for chloride containing molecules show the most variation, where for (A) cetyltrimethylammonium chloride (CTAC), (B) NaCl, (C) chlorododecane, and (D) acetylcholine chloride, the chloride band is centered around 285, 262, 264 and 267  $\text{cm}^{-1}$ , respectively. This yields an average peak position for the gold-chloride stretch at  $270 \pm 10 \text{ cm}^{-1}$ , an approximate 5  $\text{cm}^{-1}$  difference than that reported by Gao and Weaver<sup>91</sup>. For adsorbed bromide, the peak occurred more consistently at around  $192 \pm 1 \text{ cm}^{-1}$ . This resulted in an approximate 3  $\text{cm}^{-1}$  difference from the recorded SERS spectral value of 189  $\text{cm}^{-1}$ , reported by Gao and Weaver for bromide adsorption to a gold electrode, where sample preparation included placement in a dry nitrogen atmosphere. For iodide, the gold-iodide stretch appears centered at  $165 \pm 3 \text{ cm}^{-1}$ , consistent with the literature. The compound  $[\text{Bu}_4\text{N}][\text{AuI}_2]$ <sup>206</sup> has a reported frequency at 158  $\text{cm}^{-1}$  and the Au-I stretch has been characterized by a strong band at 160  $\text{cm}^{-1}$ .<sup>91</sup> The higher frequency SERS peak at 468  $\text{cm}^{-1}$  in the iododecane and acetylcholine iodide spectra may result from a C-I stretch.<sup>120</sup>



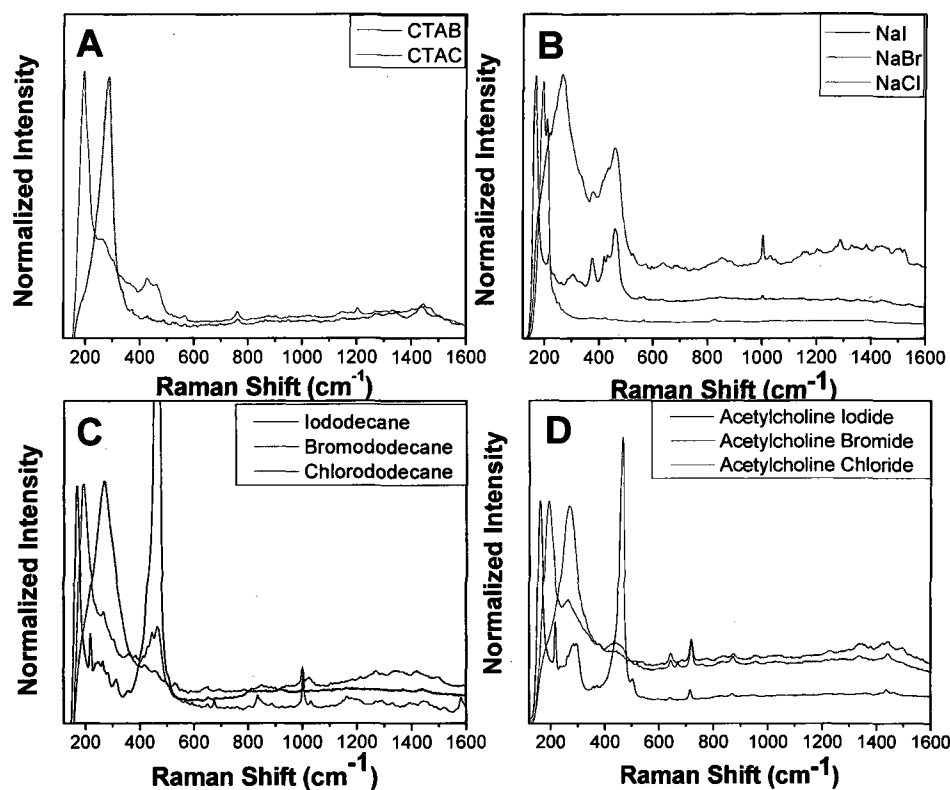


**Figure 6.1:** Normalized SERS spectra of several halogen containing molecules (40 mM, average of 5 scans): (A) cetyltrimethylammonium bromide (CTAB) and chloride (CTAC), (B) sodium iodide (NaI), bromide (NaBr), and chloride (NaCl), (C) iodododecane, bromododecane, and chlorododecane, and (D) acetylcholine iodide, bromide, and chloride.

The stretching frequencies of the Au-halide complexes can be utilized to derive their approximate force constants using Equation 3:

$$f_{M-X} = 4\pi^2 v_{M-X}^2 c^2 \mu \quad \text{Equation 3}$$

where  $c$  is the velocity of light in cm/s and  $\mu$  is the effective reduced mass of the vibrating bond in grams, which can be approximated as equal to the halide mass,  $m$ . The mass of the halide alone is used since, in this system, the Au atom is part of a whole Au nanoshell, making its mass infinitely large compared to the mass of the halide (such that  $\mu = m$ ). Here, the calculated surface-halide force constants for Au-Cl, Au-Br, and Au-I are  $1.52 \times 10^5$  dyn/cm (152 N/m),  $1.73 \times 10^5$  dyn/cm (173 N/m), and  $2.03 \times 10^5$  dyn/cm (203

N/m), respectively. These values are comparable to the force constants for Au-Cl ( $1.58 \times 10^5$  dyn/cm), Au-Br ( $1.63 \times 10^5$  dyn/cm), and Au-I ( $1.87 \times 10^5$  dyn/cm) estimated by Gao and Weaver.<sup>91</sup>

### 6.1.3: Conclusions

Since the force constant is the force necessary to stretch a bond, it is a direct measure of bond strength. Here, it is observed that as the halide ion size increases ( $\text{Cl}^- < \text{Br}^- < \text{I}^-$ ), the metal-halide force constants increase, along with increasing bond strength and covalent character<sup>207</sup>. The heavier halogens are better able to donate their  $\sigma$ -bonding electrons to the gold because of their smaller electronegativity, resulting in a more associated AuI  $\sigma$ -electron pair than the AuBr or AuCl  $\sigma$ -electron pair.<sup>208</sup> Since iodide is a better  $\sigma$ -electron donor than bromide and finally, chloride, it forms a more covalent bond with gold.

Previously, it has been observed by our group that CTAB functionalized nanoshells reshape with time, whereas CTAC functionalize nanoshells show no shell decomposition.<sup>209</sup> The strong chemical affinity of bromide over chloride to gold surfaces, along with its preference for Au{100} facets rather than Au{111},<sup>210</sup> plays a role in the observed reshaping of polycrystalline Au nanoshells in CTAB solutions. Furthermore, the chemical properties of iodide and its ability to strongly chemisorb to Au allows for its use in the removal of surface impurities, either left from substrate preparation or due to adsorbed species from the ambient environment. These impurities have limited the application of SERS for analysis of trace or unknown samples. By electrochemically oxidizing the sample after iodide chemisorption, researchers were able to clean Au nanoparticle SERS substrates to study cell membranes.<sup>211</sup> This technique may advance

the application of SERS by providing more homogeneous, impurity-free substrates for trace-analysis.

## 6.2: Au-oxygen and Au-nitrogen complexes

### 6.2.1: Introduction

In addition to metal-sulfur and metal-halogen bonding, spectral peaks in the low frequency regime can also be indicative of analyte chemisorption via oxygen and/or nitrogen functional groups. While the Au-O stretch is typically assigned *ca.*  $250\text{ cm}^{-1}$ ,<sup>212</sup> assignment of the Au-N stretch is more varied in the literature.<sup>213</sup> Some researchers have placed the Au-N stretch as high as  $470 - 550\text{ cm}^{-1}$ ,<sup>214</sup> while others report it lies within the limits of  $250-290\text{ cm}^{-1}$ .<sup>215</sup>

It is known that the Au-N bond is weaker than the Au-S bond,<sup>216</sup> and the SERS spectra of various amino derivatives differ more in appearance than analytes whose adsorption is mediated by the thioether group.<sup>217</sup> These variations and shifts in the low frequency adsorption bands are important as they allow researchers to make statements about both the nature of adsorption and the surface-adsorbate interaction.<sup>218</sup> This section discusses the SERS spectral response for several analyte molecules with oxygen and/or nitrogen functional groups.

### 6.2.2: Caffeine

Some molecules have the ability to adsorb onto metals via different moieties depending on the pH of the system, for example, caffeine (also known as 1,3,7-trimethylxanthine). Since this molecule is methylated at nitrogen 1, 3, and 7 (Figure 6.2), there is only one free site for protonation on nitrogen 9, making caffeine a monoacid base

and an ideal molecule for study. Furthermore, due to the purine structure of caffeine (a pyrimidine ring fused to an imidazole ring), the molecule contains both  $\pi$  electrons and a lone pair of electrons on the non-methylated nitrogen atom in the imidazole ring. It has been previously observed that at neutral and basic pH values, chemisorbed caffeine orients itself through these electrons in a flat orientation on the metal. However, since caffeine also contains carbonyl moieties, at low pH values, the caffeine adsorbs via either one or both oxygen atoms, with greater probability being through the oxygen of the conjugated carbonyl group (carbon 6) in an end-on orientation.<sup>219</sup> Since the  $pK_a$  of caffeine as a weak base in aqueous media at 25 °C is 3.6<sup>220-222</sup> at a pH below 3.6, the nitrogen 9 site on the molecule is in the protonated form. (Note that the literature  $pK_a$  values of 14.0 for caffeine as a weak acid are referring to the hydrogen on carbon 8).<sup>220</sup>

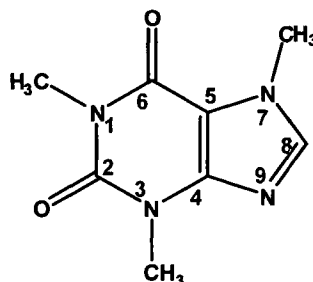


**Figure 6.2:** Chemical structure of caffeine. The molecule contains both a pyrimidine ring seen on the left side, and an imidazole ring on the right. The imidazole ring system is present in important biological building blocks such as histidine and histamine.

In order to investigate caffeine's orientation on Au nanoshells with SERS, a 100  $\mu$ M solution of caffeine (ReagentPlus, Sigma-Aldrich) and nanoshells was prepared and allowed to incubate overnight. The functionalized nanoshells were drop-dried onto clean quartz slides and investigated with the 63x immersion objective on a Renishaw microRaman. 100  $\mu$ L of water at either pH 2.0 or 9.5 (dilute NaOH or HCl were used to adjust the pH, which was then measured with pH paper) was pipetted onto the

immobilized nanoshells and incubated for ten minutes before SERS spectra were obtained. Figure 6.3 displays the (A) unenhanced Raman of powder caffeine and the (B) SERS spectra for caffeine on Au nanoshells at pH 2.0, 5.5, and 9.5.

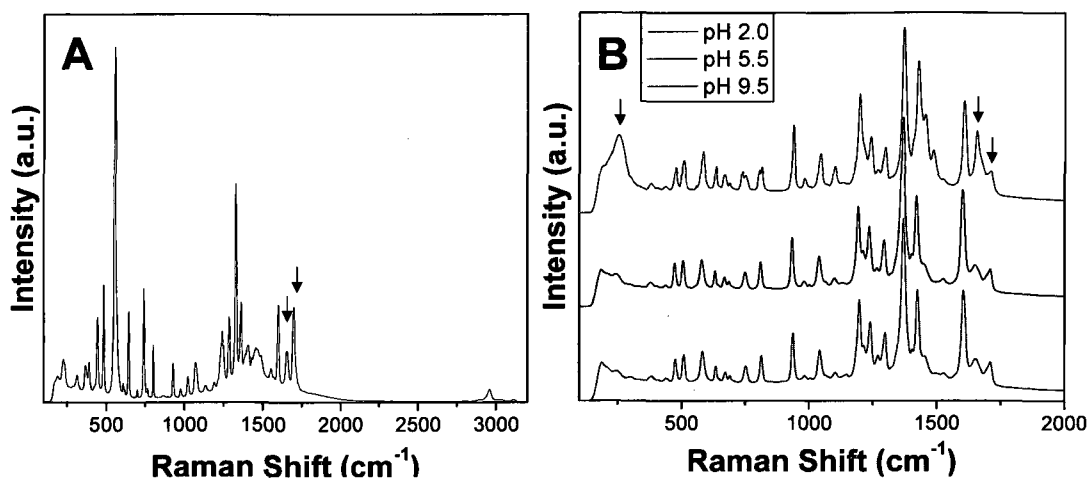


**Figure 6.3:** (A) Unenhanced Raman spectrum of caffeine powder (average of 5 scans) and (B) SERS spectra of caffeine functionalized Au nanoshells obtained at pH 2.0 (red), 5.5 (black), and 9.5 (blue) (100  $\mu$ M, offset for clarity, average of 5 scans).

At low pH (red curve), a strong, broad band at  $248\text{ cm}^{-1}$  (highlighted by the red arrow) appears in the SERS spectrum of caffeine, which is indicative of the Au-O stretching mode. This band is similar to the low wavenumber peak previously observed in the SERS spectrum of sodium ibuprofenate on Au nanoshells (see Section 5.3 and Figure 5.4), which was assigned to the adsorption of ibuprofenate onto the Au nanoshell surface via the  $\text{COO}^-$  moiety. In the case of ibuprofen, where two oxygen atoms are present, dissociation of the Na cation allows for these atoms to be chemically equivalent, resulting in a resonance structure where the double bond can be distributed among both oxygen atoms. Therefore, ibuprofen is likely chemisorbing onto the Au via both oxygen functional groups. In the case of caffeine, since a considerable amount of HCl was added to obtain such a low pH of the system, it is reasonable to consider that there may be some

contribution from the Au-Cl stretching mode, which overlaps this low spectral region (see Section 6.1).

Other differences in the spectra which occur at low, rather than neutral and high pH, are additional peaks at 735, 801, and 1480  $\text{cm}^{-1}$  and changes in the relative intensities of several peaks at 1097, 1425, 1449, and 1652  $\text{cm}^{-1}$ . The additional 735 and 801  $\text{cm}^{-1}$  peaks both have contributions from the in-plane pyrimidine ring which further support the hypothesis that the ring reorients to a more upright position at low pH. The changes in the relative intensities of the peaks at 1097, 1425, 1449, and 1652  $\text{cm}^{-1}$  also reflect caffeine's reorientation. For example, in the normal Raman of caffeine (Figure 6.3A), there are two peaks (highlighted by the red arrows) at 1655 and 1699  $\text{cm}^{-1}$  where the higher frequency peak is more than twice the intensity of the lower frequency peak. This peak intensity observation leads Pavel *et al.* to assign the 1655  $\text{cm}^{-1}$  band to an out-of-phase mode C=O stretching mode (also assigned by Falk *et al.* to the stretching of the conjugated carbonyl, carbon 6) and the 1699  $\text{cm}^{-1}$  to an in-phase stretch (also assigned to the isolated carbonyl, carbon 2).<sup>223</sup> They explain the intensity difference as a result of less energy required "to compress one carbonyl carbon atom into the ring during a cycle of the out-of-phase C=O stretching mode than is required to compress both carbonyl carbon atoms into the ring during a cycle of the in-phase C=O stretching mode." Therefore, it is reasonable to conclude that the lower and less intense frequency peak, observed here at 1655  $\text{cm}^{-1}$ , is the out-of-phase mode, and the peak at 1699  $\text{cm}^{-1}$  is the in-phase mode.

In the SERS spectra (Figure 6.3B), however, the peak at 1652  $\text{cm}^{-1}$  (the out-of-phase stretch or conjugated carbonyl) is more enhanced at low pH, while the higher frequency peak at 1706  $\text{cm}^{-1}$  (the in-phase mode or isolated carbonyl) does not show any

changes in intensity at low pH. The upshift of the in-phase stretching mode from 1699  $\text{cm}^{-1}$  in the unenhanced Raman to 1706  $\text{cm}^{-1}$  in SERS, is likely due to protonation of the nitrogen 9, as similar shifts have been observed for other purine ring systems such as adenine.<sup>224</sup>

The enhancement of the peak at 1652  $\text{cm}^{-1}$  at low pH is in agreement with the postulate that protonated caffeine chemisorbs with greater probability through the oxygen of the conjugated carbonyl group. Our results are consistent with that of Pavel *et al.* observed on Ag colloid. If the protonated caffeine were adsorbing through both carbonyl moieties, then both carbonyl modes would be of similar intensities at low pH. Furthermore, this type of adsorption is not likely since there is a methylated nitrogen in between the carbonyl groups, which may prevent this type of binding due to steric hinderence. If the caffeine were adsorbing through the isolated carbonyl on carbon 2, then the 1652  $\text{cm}^{-1}$  mode should either not be enhanced or be absent due to surface selection rules, and the 1706  $\text{cm}^{-1}$  instead would be enhanced.

### 6.2.3: Water soluble cholesterol

Water soluble cholesterol can also chemisorb onto nanoshells via the oxygen atom. This compound consists of methyl beta cyclodextrin encapsulating the cholesterol. The structure of water soluble cholesterol (Sigma, C4951) is seen in Figure 6.4. While there are no nitrogen functional groups within the structure, there are several carbonyl groups. Figure 6.5 displays the unenhanced Raman spectrum (A) and SERS spectrum (B). The low frequency peak at 242  $\text{cm}^{-1}$  is indicative of the Au-O stretch although for this system, it appears  $\sim 6 \text{ cm}^{-1}$  lower than the caffeine and ibuprofen nanoshell systems.

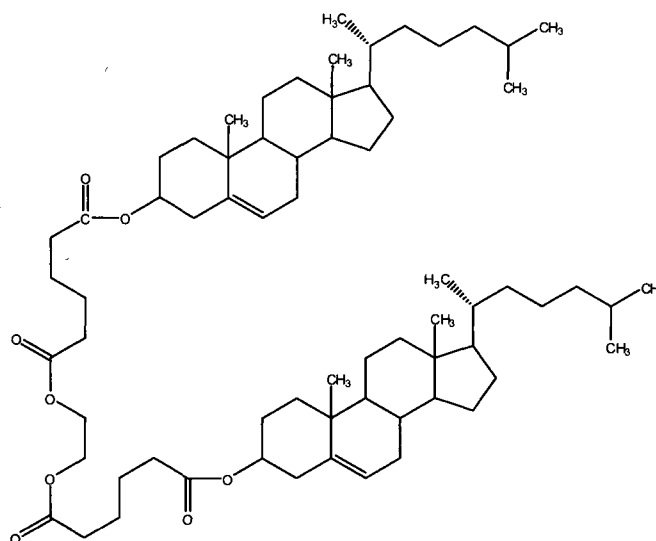


**Figure 6.4:** Chemical structure of water soluble cholesterol.

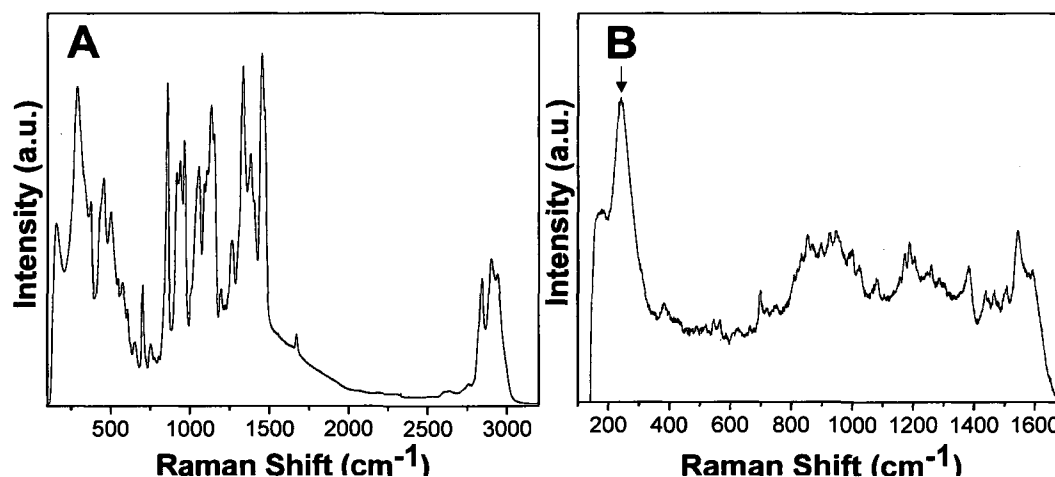


**Figure 6.5:** (A) Unenhanced Raman spectrum of water soluble cholesterol powder (average of 5 scans) and (B) SERS spectrum of water soluble cholesterol adsorbed on Au nanoshells (100  $\mu\text{M}$ , average of 10 scans).

#### 6.2.4: Pyridine

Pyridine, shown in the inset of Figure 6.6, is a water-soluble, organic molecule with a lone pair of electrons on its one nitrogen functional group. The molecule can interact with a metal surface either through its  $\pi$  electrons, where it is forced to assume a flat orientation, or via the lone pair of electrons on the nitrogen in an end-on attachment.



The simplicity of the molecule has made it attractive for study by several research groups, where it has been labeled a universal model system for SERS studies. For example, the Van Duyne research group has examined the SERS response of pyridine molecules adsorbed on silver film over nanosphere (FON) electrodes.<sup>225</sup> Here, the SERS spectrum of 10  $\mu\text{M}$  pyridine on Au nanoshells is presented in Figure 6.5. The substrate was prepared by drop drying the 10  $\mu\text{M}$  pyridine-nanoshell solution onto unfunctionalized quartz. The spectrum is dominated by the large and broad low frequency peak at around 270  $\text{cm}^{-1}$ . While Creighton *et al.* reports the N-Au stretching vibration for pyridine on Au at 260  $\text{cm}^{-1}$ ,<sup>226</sup> the lack of ring breathing modes in the spectrum presented here (typically, strongly observed for surface pyridine at 1008, 1036, 1218 and 1605  $\text{cm}^{-1}$ )<sup>9</sup> indicates that the molecule is lying in a flat configuration. Rather than being axially attached, pyridine is interacting with the Au through the  $\pi$  electron cloud. B3LYP/LANL2DZ Gaussian calculations for the SERS spectrum of pyridine on Au in the presence of NaCl (data not shown) also predict that the low-frequency region is dominated by  $\text{Cl}^-$  and that the Au-Cl stretch can yield significant Raman intensity at around 250  $\text{cm}^{-1}$ .<sup>227</sup>

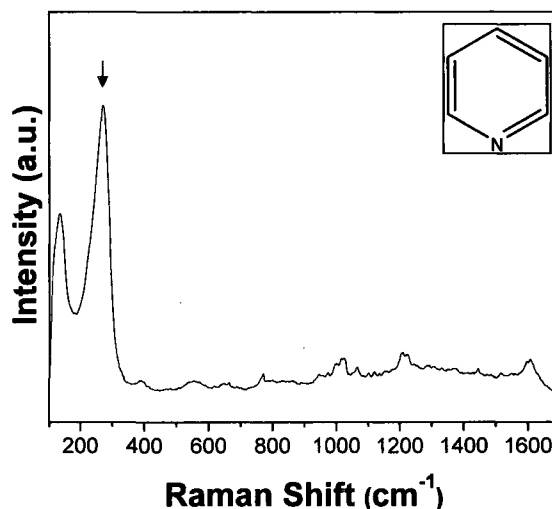


**Figure 6.6:** SERS spectrum of pyridine functionalized Au nanoshells (10  $\mu\text{M}$ , average of 5 scans, inset shows the chemical structure of pyridine).

### 6.2.5: Aniline

In contrast to pyridine, where the electron pair on the nitrogen resides in an  $sp^2$  orbital in the plane of the ring,<sup>228</sup> the nitrogen in aniline is  $sp^3$  hybridized. This dissimilar hybridization results in a different orbital arrangement, where for  $sp^2$  hybridization the  $p$  orbital is perpendicular to the plain of the ring. In the case of aniline, the simplest aromatic amine (shown in the inset of Figure 6.7), the geometry at the nitrogen is pyramidal rather than planar, which may result in different orientations and surface-adsorbate interactions between these two analyte molecules on Au nanoshells. Many researchers are interested in obtaining SERS spectra of aniline as it is a main product in the reduction of nitrobenzene<sup>229</sup> and because it is capable of forming electronically conducting polymers<sup>230-232</sup>.

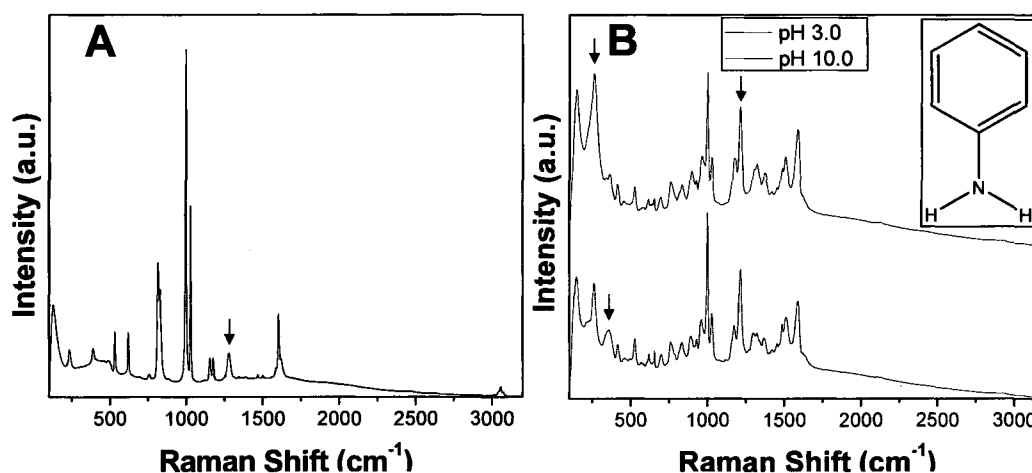


**Figure 6.7:** (A) Unenhanced Raman spectrum of neat aniline (average of 5 scans) and (B) SERS spectra of aniline functionalized Au nanoshells at pH 3.0 (red) and 10.0 (blue) (1 mM, offset for clarity, average of 5 scans, inset shows the chemical structure of aniline).

To investigate the surface-adsorbate interaction between aniline and Au nanoshells, a 1 mM solution of aniline (99.5+%, A.C.S. reagent, Sigma Aldrich) and nanoshells was prepared and allowed to incubate overnight. The functionalized nanoshells were drop-dried onto clean quartz slides and investigated with the 63x immersion objective on the Renishaw microRaman. 100 uL of water at either pH 3.0 or 10.0 (dilute NaOH or HCl were used to adjust the pH, which was then measured with pH paper) was pipetted onto the immobilized nanoshells and incubated for ten minutes before SERS spectra were obtained. Figure 6.7 shows the (A) unenhanced Raman and (B) SERS spectra of aniline adsorbed on Au nanoshells at pH 3.0 and 10.0.

The SERS spectra overall appear consistent with the work of R. Holze<sup>233</sup> in that at both acidic and basic conditions aniline appears to adsorb mostly edge-on to the nanoshells (the author had used a polycrystalline gold electrode). A strong ring deformation is observed at  $998\text{ cm}^{-1}$  and C-H in plane bending is seen at  $1026\text{ cm}^{-1}$ . The peak at  $1280\text{ cm}^{-1}$  in the unenhanced spectrum assigned to a C-N stretch (as highlighted by the red arrow) downshifts to  $1213\text{ cm}^{-1}$  in the SERS, indicating coordination of the nitrogen with a metal.<sup>234</sup> There are also two strong peaks (highlighted by red arrows) at around  $257\text{ cm}^{-1}$  and  $354\text{ cm}^{-1}$  under both pH conditions. While the peak at  $257\text{ cm}^{-1}$  grows at low pH (with increasing  $\text{Cl}^-$  concentration), the  $354\text{ cm}^{-1}$  peak is stronger at basic conditions (where the lone pair is more free to coordinate with the gold). Holze assigns the Au-N vibration at around  $347\text{ cm}^{-1}$  in the presence of  $\text{Cl}^-$ .<sup>233</sup> Therefore, it is reasonable to conclude that the  $257\text{ cm}^{-1}$  peak is a result of Au-Cl (see Section 6.1) and the  $354\text{ cm}^{-1}$  peak is due to Au-N. When the pH of the solution is raised, coordination sites on the Au previously occupied by  $\text{Cl}^-$  can instead be occupied by aniline.

### 6.2.6: Nanoshell binding peptide

Utilizing the techniques of phage display<sup>235</sup> a peptide sequence was derived by the Naik research group to bind specifically to Au nanoshells prepared with potassium carbonate plating solution. Peptides have been reportedly engineered with the abilities to reduce chloroauric acid to form Au nanoparticles which are then coated and stabilized by the peptide<sup>236</sup>, to bind to Au for surface patterning<sup>237</sup>, and for nanoshell-nanoshell and nanoshell-quantum dot assembly<sup>238</sup>. SERS presents an analytical technique for the direct detection of gold-binding peptides and eliminates the need for indirect labeling methods.<sup>239</sup>

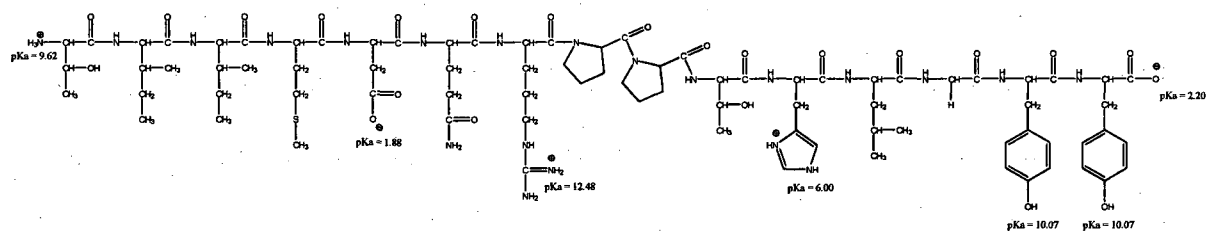


**Figure 6.8:** Sequence of the Au nanoshell binding peptide NS32Y with predicted charges on the residues in milliQ water at pH 5.5.

The sequence of the peptide for Au nanoshell binding derived from phage display is TIIMDQRPPHTL, where, for this sequence, the peptide has a pI of 6.41 and MW of 1805.08. The nanoshell binding peptide has been coined NS32Y, and two tyrosine and one glycine residue were attached at the end of the binding sequence (TIIMDQRPPHTLGYGYY) to facilitate its observation with SERS. In milliQ water, where the pH is approximately 5.5, the charges on the peptide residues can be found in Figure 6.8, where the calculated pI (the average of the pK<sub>a</sub>s for each residue) for NS32Y is 7.47.

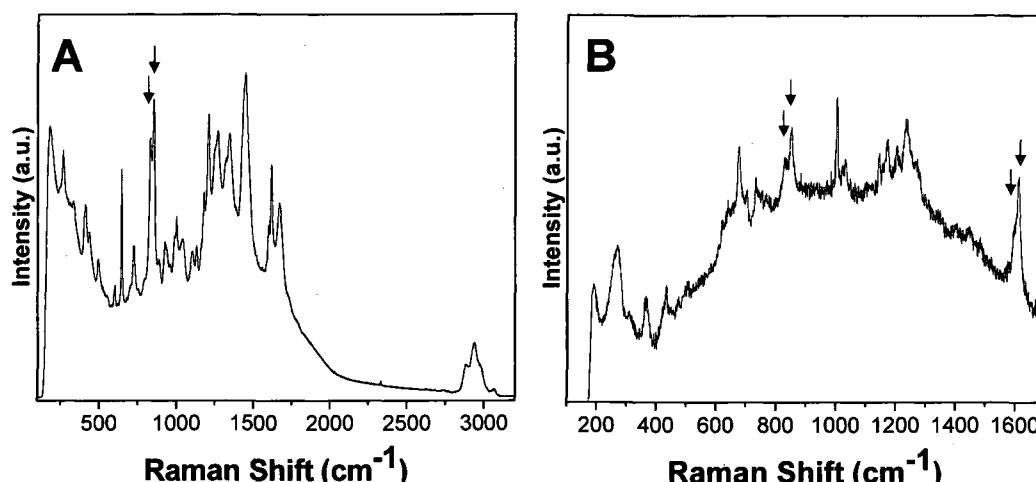


**Figure 6.9:** (A) Unenhanced Raman spectrum of NS23Y powder (average of 5 scans) and (B) SERS spectrum of NS23Y functionalized Au nanoshells (500  $\mu\text{M}$ , average of 5 scans).

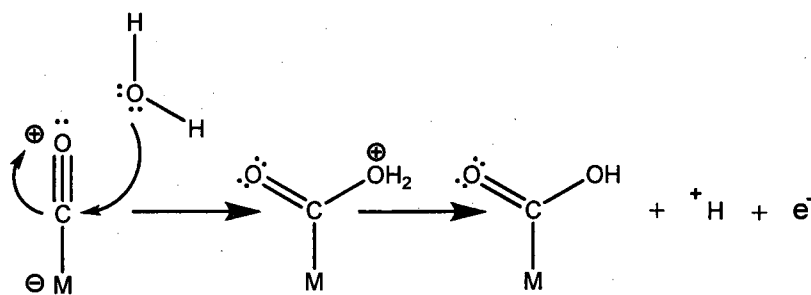
Short incubation of the NS32Y peptide with nanoshells (without thermal treatment) leads to observable functionalization, as the nanoshells attach to the sides of the glass vial. Figure 6.9 displays the unenhanced powder Raman (A) and solution SERS (B) spectra of 500  $\mu\text{M}$  NS23Y functionalized nanoshells. In both the unenhanced Raman and SERS spectra, the presence of tyrosine is indicated by the doublet at around 829 and 850  $\text{cm}^{-1}$  which occurs due to the Fermi resonance between a totally symmetric ring breathing mode and the first overtone of an out-of-plane ring vibration.<sup>240</sup> The location of the Fermi resonance peaks can provide insight into the ionization/protonation of this side chain. When the hydroxyl group of the tyrosine is ionized, it has been observed that the Fermi resonance peaks shift to 833 and 854  $\text{cm}^{-1}$ .<sup>241</sup> Also, since there is no observable down shifting of the 1595 and 1612  $\text{cm}^{-1}$  peaks to 1578 and 1545  $\text{cm}^{-1}$  in the SERS spectrum, it is suspected that the tyrosine remains protonated and is not interacting with the metal surface.<sup>242</sup> These results are consistent with that from Lee *et al.*<sup>243</sup> and, since the tyrosine residue was not part of the sequence derived from phage, it is not surprising that

peptide binding to the metal occurs via another functional group. The low frequency peaks at 270 and 366  $\text{cm}^{-1}$  may result from gold-chloride (see Section 6.1.2) and gold-nitrogen binding (see Section 6.2.5) as sodium chloride is present during nanoshell synthesis, while nitrogen is present in the histidine residue and abundant in the peptide backbone.

### 6.3: CO adsorption on Au nanoshells

Various SERS spectra obtained on Au nanoshell substrates contain a lone, high frequency peak originally coined the “mystery peak” at around 2100  $\text{cm}^{-1}$ . Depending on nanoshell preparation and age, the peak intensity varies and can be surprisingly strong considering the near-field plasmon bandwidth drop off at high frequency. This peak often appears in the background SERS spectra of bare nanoshells and can also appear in functionalized nanoshell spectra with a higher occurrence at low analyte concentrations. R. Aroca<sup>244</sup> attributes a peak at 2122  $\text{cm}^{-1}$  observed in SERS spectra on both colloids and films to CO, which has been known to be prevalent on Au and considered as a source of interference in recorded SERS spectra.

Since Au-O bands are assigned to the low frequency spectral region (see Section 6.2), the high frequency position of the peak indicates that CO is adsorbing on the metal via the carbon atom rather than through the oxygen. While electronegativity predicts that the oxygen end of CO is more negative, and that CO and metal atoms might likely react in the M-O-C geometry, nearly all known metal-carbon monoxide compounds bind in the M-C-O geometry.<sup>245</sup> Gilman describes a mechanism for CO adsorption on metals (such as platinum) under acidic conditions:<sup>246</sup>

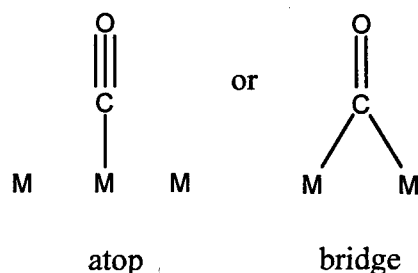


Equation 4

where M represents the metal. This suggests that CO adsorption may be thermodynamically driven by pH changes or electrical potential.

It has also been observed that CO adsorption follows the affinity trend: Pd>Pt>Au>Cu>Ag for various metals.<sup>247</sup> In the case of Au, CO adsorption has been observed on various types of surfaces ranging from nanoparticles to Au(111) and has also been shown to occur on low-coordinated Au atoms at steps and kinks.<sup>248</sup> CO has been shown to bind stronger on Au(111) at step sites rather than terraces.<sup>249</sup>

CO adsorbed on metal surfaces can occupy either atop (also known as terminal or linear-bonded) or bridge sites as seen below:



Equation 5

CO adsorption in the linear form on gold is the result of the donation of the lone pair of electrons on carbon into vacancies in the d band of gold caused by thermal promotion into the 6s level.<sup>250</sup> This electron donation makes the metal more electron rich and, in order to relieve itself of this added electron density, a filled metal d-orbital may interact with the empty pi\* orbital on the carbonyl ligand. This component of CO bonding is

known as pi-backbonding. While CO as a terminal ligand attached to a single metal is more commonly found, CO can be bridged between two or more metals.

For free carbon monoxide, the C-O stretch observed by IR is at  $2143\text{ cm}^{-1}$ .  $\sigma$ -donation by CO's bonding orbital and  $\pi$ -acceptance by the antibonding orbitals due to bonding between CO and metal atoms weaken the C-O bond and result in lower energy stretching modes.<sup>245</sup> The frequency for the atop and bridge bonded CO bands are observed in FTIR spectroscopy at  $2072$  and  $1824\text{ cm}^{-1}$  for silica-supported platinum catalyst substrates prepared by a traditional impregnation method. When the CO bridges two metal atoms, both metals contribute electron density to the  $\pi$ -orbitals which weaken the CO bond and further lower the energy of the stretch. However, for the same aforementioned catalysts prepared with a molecular-capping based synthesis, the atop and bridge bond CO bands are observed at  $2092\text{ cm}^{-1}$  ( $20\text{ cm}^{-1}$  higher) and as a broad low intensity band between  $1900$  to  $1800\text{ cm}^{-1}$ . This finding indicates that when the same catalyst is made by two different preparation methods, there is some difference in the CO surface binding sites. Additionally, temperature plays a role in the preferred binding site. Silica-supported gold catalysts display a predominant band at  $2115\text{ cm}^{-1}$  and another band at  $2047\text{ cm}^{-1}$  when treated at  $200\text{ }^{\circ}\text{C}$  whereas at  $400\text{ }^{\circ}\text{C}$ , the  $2047\text{ cm}^{-1}$  band becomes predominant.<sup>251</sup>

Aside from the above mentioned surface isomers, CO can also occupy a three-fold-hollow site. Such is the case with Pd, where an increase in coverage of adsorbed CO lead to an emergence of bridge coordinated bonding assigned at higher IR frequencies than that of the three-fold-hollow site.<sup>252</sup>



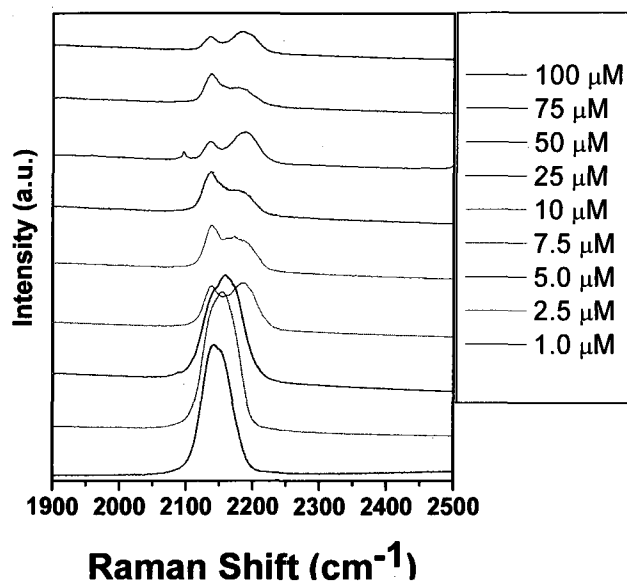


**Figure 6.10:** High frequency SERS spectra for *p*MBA functionalized nanoshells (1  $\mu\text{M}$  to 0.1 mM). At low *p*MBA concentrations a predominant peak at 2138  $\text{cm}^{-1}$  is observed and attributed to CO. As the concentration of *p*MBA is increased, the adsorbed atop bound CO is displaced and the high frequency peak decreases in intensity. The conversion to a doublet at 2136 and 2181  $\text{cm}^{-1}$  indicates that the little CO that remains occupies the atop adsorption site or consists as free CO in solution near the metal nanoshell. (Normalized intensity, spectra offset for clarity.)

Similarly, in our SERS work on Au nanoshells, we observe two CO bands at 2136  $\text{cm}^{-1}$  and 2181  $\text{cm}^{-1}$  as analyte concentrations of the molecule *p*MBA is increased (see Figure 6.7). Since CO adsorption on Au has been shown to have a high occurrence at step sites, it is likely that the CO adsorption on Au nanoshells is occurring where fissures and holes have formed as a result of nanoshell aging. Following the observed trends in IR spectroscopy, it is more likely the case that the intense peak at 2138  $\text{cm}^{-1}$  at low analyte concentration is the atop bound CO, which is displaced from the metal as *p*MBA concentration increases. It is not likely CO is on a bridge site, as this peak would be expected to occur at much lower frequencies ( $\sim 1700 - 1850 \text{ cm}^{-1}$ ). As the CO is displaced from the metal surface, a higher frequency peak at 2181  $\text{cm}^{-1}$  appears. The observed variation in peak position may result from the extent of CO backbonding, as the

transfer of electron density from the metal to a ligand antibonding orbital will weaken the energy of the carbon-oxygen bond. The degree to which backbonding occurs will be indicated by the extent of the frequency shift.<sup>253</sup>

## **Chapter 7: Magnetic-plasmonic core-shell nanoparticles**

### **7.1: Introduction**

Hybrid magnetic-plasmonic nanoparticles offer a novel, promising platform which combines the potential for magnetic manipulation with plasmonic sensing in a single nanostructure. The work presented in this chapter demonstrates the synthesis and plasmonic properties of Au coated magnetic iron oxide nanoparticles.<sup>254</sup> This system differs from those previously reported in the literature in that the nanoshell core is composed of wüstite, which has undergone slight oxidation to magnetite. Additionally, this work is significant as it provides the only known method for estimating the dielectric properties of nanoparticles around which a plasmonic shell is grown. Experimental work was performed in collaboration with Cristina Hofmann and Anna Kelly in Prof. Whitmire's lab at Rice University. Theoretical modeling of the plasmonic properties was performed in collaboration with Tamer Ali and Dr. Peter Nordlander, and examination of the magnetic properties was performed in collaboration with Dr. Emilia Morosan. Submitted for publication to ACS Nano.

Currently, there is great interest in the development of nanoparticles that combine multiple functions or properties not obtainable in individual materials.<sup>255,256</sup> New nanoparticles that combine an optical signature with other physical properties are particularly useful, enabling optical addressability for tracking or monitoring particles in

addition to other properties. A very useful strategy for imparting optical properties at the nanoscale involves the integration of noble metals, and their associated localized surface plasmons, into the particle or structure. The growth of a thin Au shell layer around a functional nanoparticle core provides a practical and highly general approach for adding optical addressability to virtually any type of nanoparticle.<sup>44,165</sup> Au shell layers provide a strong plasmon resonant optical response to the nanoparticle, with a resonant frequency determined by geometry, the dielectric properties of the nanoparticle core and the surrounding medium of the nanoparticle.<sup>257</sup> In addition, the Au shell layer provides a relatively chemically inert surface layer that can be functionalized to enhance solubility in various media, promote biocompatibility, and preserve the properties of the core material.

In this chapter, we report the combination of resonant optical and magnetic properties in a single nanostructure, accomplished by the growth of an Au shell layer around magnetic iron oxide nanoparticle cores. Previously reported studies combining plasmonic and magnetic nanostructures have focused largely on iron,<sup>258-261</sup> the thermodynamically favorable forms of iron oxides such as magnetite,<sup>262-264</sup> and silica-magnetite composites.<sup>262,265,266</sup> Generally, partial coverage of small gold nanoparticles bound to the surface of the iron oxide particles has been achieved, but attaining uniform, continuous Au layers has been a challenge.<sup>267</sup> Here we show that wüstite ( $\text{Fe}_x\text{O}$ ) nanocrystals,<sup>268-274</sup> which can also form oxides of higher oxidation states, can be used as a magnetic core material and initial precursor for continuous gold shell layer growth. Wüstite nanocrystals can be grown in a variety of shapes and sizes; however, the subsequent addition of an Au layer on the nanocrystal surface modifies the overall

nanoparticle shape, resulting in a spherical or near-spherical morphology with a nonspherical core. In addition to a complex morphology, the dielectric properties of nanocrystalline wüstite can also be complex, dependent upon other Fe oxides that may be present in the edges or corners of the nanocrystal. Optical measurements combined with theoretical analysis of the plasmon-resonant response of the wüstite core-Au shell nanostructures allow us to deduce the permittivity of the wüstite-mixed-oxide core nanocrystals. While plasmonic nanoparticles have been used extensively as localized surface plasmon resonant nanosensors of their environment, this is the first case of the use of plasmonic properties to assess the dielectric properties of an embedded nanomaterial within the nanoparticle itself.

The use of wüstite precursors as a magnetic core material offers several unique advantages in the design of multifunctional magnetic nanoparticles. The metastability of wüstite provides control over the size and shape of the nanocrystal, whose properties can also be varied with composition, by the generation of mixed phases of wüstite, magnetite, and iron in the nanocrystalline structure. This can be accomplished by annealing in inert or oxidizing atmospheres, or by heating the nanocrystals in a high boiling point solvent, such as hexadecane.<sup>275</sup> Through manipulation of the material composition in these ways, the magnetic behavior could be tailored to a specific application or device. Wüstite may provide a preferable core material for mixed magnetic-plasmonic nanoparticles since traditional magnetic nanomaterials aggregate even after Au coating due to an extremely strong magnetic attraction.<sup>276</sup>

## 7.2: Experimental

Tri-n-octylamine (TOA; 98%), oleic acid (OA; 90%), tetrachloroauric acid ( $\text{HAuCl}_4 \cdot 3\text{H}_2\text{O}$ ), Tetrakis(hydroxymethyl)phosphonium chloride (THPC, 80% solution in water), 3-Aminopropyltriethoxysilane (APTES,  $\geq 98\%$ ), and hexane were purchased from Sigma-Aldrich (St. Louis, MO). Hexane was distilled using standard procedures.<sup>277</sup> Sodium hydroxide (NaOH, 1 N), sodium chloride (NaCl, Biological, Certified), potassium carbonate ( $\text{K}_2\text{CO}_3$ , Certified A.C.S.) and formaldehyde (37%) were obtained from Fisher Scientific (Hampton, NH). 200 proof ethanol was obtained from Decon Laboratories, Inc. (King of Prussia, PA). Ultrapure water (18.2 M $\Omega$  resistivity) was obtained from a Milli-Q water purification system (Millipore, Billerica, MA).

Reactions were carried out using standard Schlenk techniques. The formation of the iron oxide nanoparticles was accomplished by the decomposition of 0.5 g iron formate ( $\text{Fe}^{\text{II}}(\text{HCOO})_2 \cdot 2\text{H}_2\text{O}$ ) in the presence of a tri-n-octylamine: oleic acid (7 mL:1 mL, TOA:OA) surfactant system with the addition of 100  $\mu\text{L}$  of HPLC grade  $\text{H}_2\text{O}$ , under inert atmosphere at elevated temperatures (*ca.* 370 °C). This protocol has been reported to yield nanoparticles composed of a wüstite core with magnetite-rich corners and edges.<sup>275</sup> The particles were then centrifuged three times for ten minutes at 2224 RCF, redispersed each time in 10 mL of dry hexane, and dried under vacuum without heating.

The precursor nanoparticle solutions used in the present study were fabricated following a similar procedure as the previously reported methods for the immobilization of Au nanoparticles on silica<sup>28,278</sup> or hematite<sup>279</sup> surfaces. The surface of the iron oxide nanoparticles was functionalized with organosilane molecules (APTES) to generate an amine terminated surface. APTES functionalization was performed by one of two

methods, either by (1) centrifuging an additional three times, redispersing in 200 proof ethanol, and under vigorous stirring, the quick addition of 600  $\mu\text{L}$  of APTES or by (2) silane ligand exchange, where in a glass container under ambient conditions, 0.5% (v/v) APTES was added to the nanoparticles in hexane containing 0.01% (v/v) acetic acid<sup>280</sup> causing precipitation of the particles. The particles were stirred overnight and then rinsed by centrifuging and redispersing with either ethanol (method 1) or water (method 2) to get rid of any excess APTES. Surface functionalization with silane ligand exchange (method 2) was used when the hydrophobic surfactant coating could not be displaced by method 1.

A colloidal gold solution yielding  $\sim 2$  nm Au particles was prepared using THPC as the reductant according to Duff *et al.*<sup>281</sup> and was refrigerated for at least two weeks before use. The precursor nanoparticle solution was made by the addition of 40 mL of the aged THPC colloidal gold solution, 4 mL of 1 M NaCl, and 500  $\mu\text{L}$  of APTES functionalized iron oxide nanoparticles and refrigerated overnight. The precursor solution was then centrifuged three times until the supernatant was colorless at 300 RCF for 30 minutes to remove excess free colloidal gold nanoparticles and was redispersed each time in Milli-Q water with a sonicating probe.

A 44  $\mu\text{M}$   $\text{HAuCl}_4$  plating solution was produced by the addition 1 wt % chloroauric acid to 1.8 mM aqueous  $\text{K}_2\text{CO}_3$ . The solution was stored for a minimum of 12 hours in the dark. Au coated iron oxide nanoparticles were synthesized by the reduction of  $\text{AuCl}_4^-$  ions in the plating solution by formaldehyde onto the precursor nanoparticles. Shell thickness was controlled by varying the ratio between the precursor

particles and aqueous  $\text{AuCl}_4^-$  ions. Complete shell growth took about 10 minutes and was monitored by solution extinction measurements.

Transmission electron microscope (TEM) micrographs were obtained using a JEOL 2010 TEM. Scanning electron microscope (SEM) images were obtained on a FEI Quanta 400 environmental SEM at an accelerating voltage of 20 kV. Extinction spectra were obtained using a Cary 5000 UV/Vis/NIR spectrophotometer. X-ray diffraction (XRD) patterns were obtained using a Rigaku Ultima II vertical  $\theta$ - $\theta$  powder diffractometer ( $\text{CuK}\alpha$ ,  $\lambda = 1.5418 \text{ \AA}$ ). XRD patterns between  $20^\circ < 2\theta < 70^\circ$  were collected. Materials Data, Inc., (MDI) JADE8 software was used to subtract the background. Raman spectra were collected on a Renishaw inVia Microscope, using a 785 nm excitation source with a 1.5 mW laser power. Magnetization measurements as a function of applied field and temperature  $M(H,T)$  were performed in a Quantum Design Magnetic Properties Measurement System (QD MPMS) ( $T = 1.8 \text{ K} - 400 \text{ K}$ ,  $H_{\text{max}} = 7.0 \text{ T}$ ).

### 7.3: Results and discussion

Au shell layer growth on wüstite nanocrystals is a relatively straightforward synthetic procedure.<sup>28,278,279</sup> Various stages of the growth process are depicted in schematic form (Fig. 7.1 A,D). The nanoparticle morphologies at various stages of the growth process are imaged using transmission electron microscopy (Fig. 7.1 B,C and E,F). To grow the Au shell layer on the nanocrystals, we began with monodisperse wüstite nanocrystals of either faceted (Fig. 7.1 B,C i) or tetracubic (Fig. 7.1 E,F i) shape, with approximate radii of  $31.5 \pm 9.7 \text{ nm}$  and  $28.5 \pm 7.3 \text{ nm}$ , respectively. The synthesized particles were surfactant stabilized, which presents a noticeable thin, almost

transparent layer around the particles in the TEM images in Figure 1. The nanocrystals were then functionalized with an amine-terminated linker molecule which displaces the surfactant and allows for the attachment of  $\sim 2$  nm Au colloid to the nanocrystal surface (Fig. 1 B,C and E,F ii). The immobilized colloidal gold acts as nucleation sites for electroless gold plating onto the precursor nanoparticles to form a continuous gold shell (Fig. 7.1 B,C and E,F iii, shown here with an approximate 27 nm shell thickness). The thickness of the gold shell layer can be controlled by varying the concentration of  $\text{AuCl}_4^-$  in the final reduction step. Although the nanocrystalline cores are faceted or tetracubic in shape, the Au shell layer growth results in spherically shaped particles.

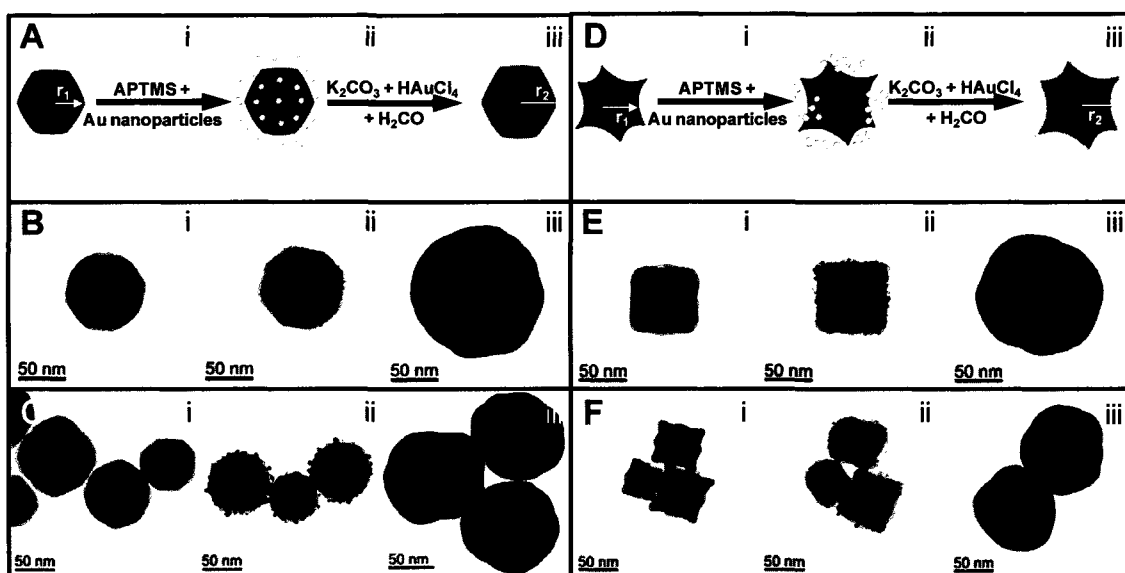


**Figure 7.1:** Schematic of Au coated iron oxide synthesis for (A) faceted and (D) tetracubic (i) unfunctionalized core, (ii) Au decorated precursor, and (iii) Au coated iron oxide nanoparticles. TEM images representing various stages of synthesis for (B, C) faceted and (E, F) tetracubic (i) unfunctionalized core (with average  $r_1 = 31.5 \pm 9.7$  nm and  $28.5 \pm 7.3$  nm), (ii) Au nanoparticle decorated precursor, and (iii) Au coated iron oxide nanoparticles.

The core-shell geometry of the fabricated nanoparticles supports a plasmon resonant response dependent upon nanocrystalline core size, Au shell layer thickness, and



the dielectric properties of the core, shell, and embedding medium.<sup>257</sup> Silica core-Au shell nanoshells<sup>282</sup> demonstrate strong resonance absorption in the visible and near-infrared (NIR). For the silica-Au nanoshell structure, the plasmon absorption band shifts to shorter wavelengths as the thickness of the gold shell is increased. In contrast, it has been observed that magnetite iron oxide cores with Au shell layers show a redshifted plasmon absorption peak with increasing shell thickness.<sup>283</sup>

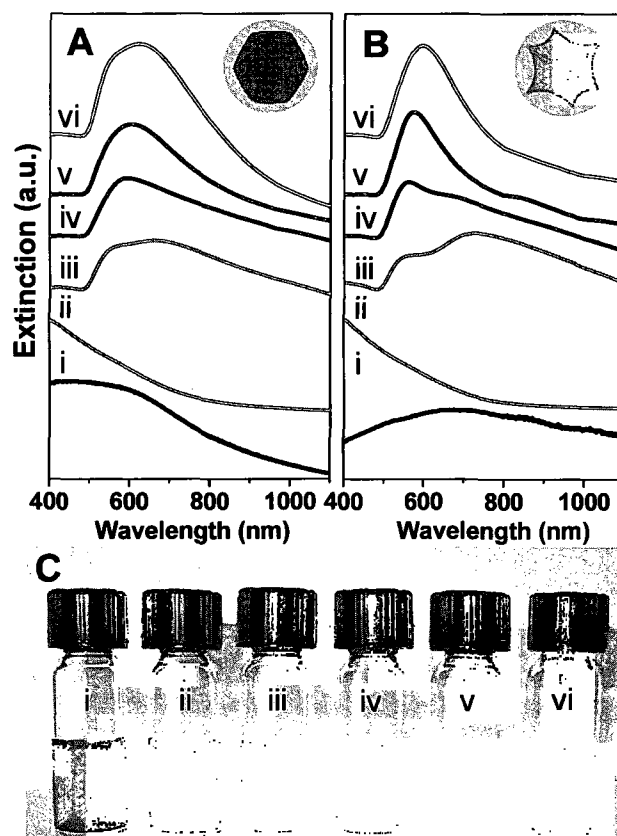


**Figure 7.2:** Solution extinction measurements of (A) faceted (B) and tetracubic gold coated iron oxide (i) ethanolic uncoated cores ( $r_1 = 31.5 \pm 9.7$  and  $28.5 \pm 7.3$  nm), (ii) Au-decorated precursor nanoparticles ( $r_1 = 32.6 \pm 9.0$  and  $28.6 \pm 8.5$  nm) in aqueous solution, and (iii-vi) Au coated nanoparticles with increasing Au thicknesses (number of particles sized is 100,  $r_2$  is  $59.9 \pm 12.4$ ,  $65.0 \pm 19.9$ ,  $73.1 \pm 11.7$ , and  $76.6 \pm 9.8$  nm for the faceted cores and  $40.0 \pm 6.7$ ,  $49.1 \pm 10.7$ ,  $53.8 \pm 4.6$ , and  $66.4 \pm 5.0$  nm for the tetracubic cores in aqueous solution. (Spectra offset for clarity.) (C) Optical image of particles shown in A.

Extinction spectra of the wüstite core-Au shell nanoparticles in solution are shown in Figure 7.2 A,B. The large core size of the nanoparticles (average approximate radii 32 and 29 nm, respectively) and the thick Au shell layers (from 11 to 45 nm) allow for a prominent surface plasmon resonance peak. As the shell thickness increases (Fig. 7.2 A,B iii-vi), the plasmon peaks shift to longer wavelengths. An optical image (Fig. 7.2C) of the particles represented in Figure 7.2A shows the corresponding change in color of the nanoparticles suspended in aqueous solution with increasing shell layer thickness. The wide range of colors displayed resulting from the variation in Au shell layer thickness allows for the potential use of these nanoparticles for spectroscopic or colorimetric labeling.<sup>284,285</sup>

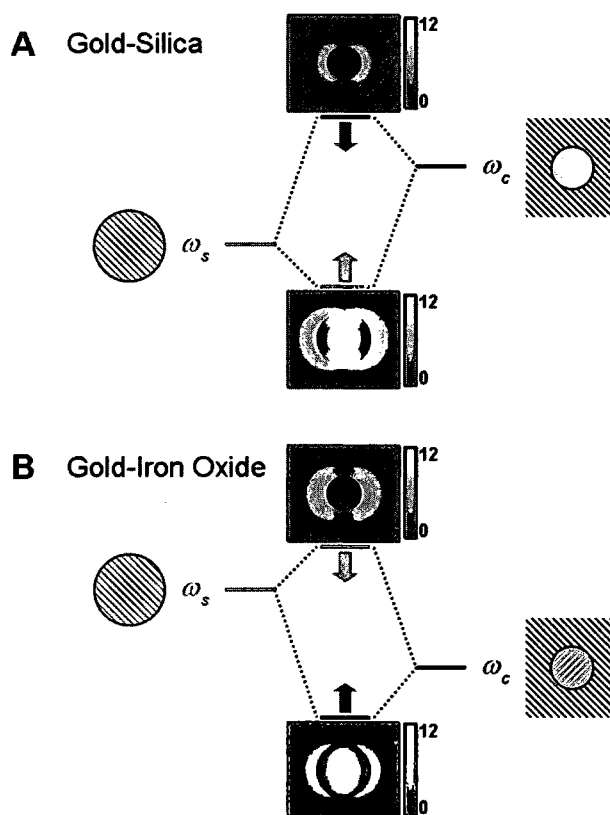


**Figure 7.3:** Hybridization in a nanoshell (A) with a low permittivity core, *e.g.*, silica, and (B) with a high permittivity core, *e.g.*, iron oxide. Dark (black) and bright (red) plasmon modes are shown in each case. Arrows show the shift of the hybridized plasmon

modes with increasing shell layer thickness. The colored insets show local electric field enhancements distributions for the spherical-core geometries in Figure 4A,B. A silica core is selected for insets in (A) showing dark (A-upper) and bright (A-lower) modes. A high permittivity core ( $\epsilon = 12.0$ ) is selected for insets in (B) showing bright (B-upper) and dark (B-lower) modes. The inner radius of the core is  $r_1 = 32$  nm and the outer radius of the shell is  $r_2 = 50$  nm. A drude model is used to represent the gold material dielectric properties.

The anomalous plasmon redshift with increasing Au shell layer thickness observed for iron oxide cores can be understood in terms of plasmon hybridization.<sup>29,31</sup> In this picture, the sphere plasmons associated with the outer surface of the shell layer interact with the cavity plasmons associated with the inner surface of the shell (Fig. 7.3). Two hybridized plasmons result from this interaction, a “bright” or “bonding” plasmon that couples strongly to the incoming and outgoing light waves and a “dark” or “antibonding” nanoshell plasmon mode that couples poorly to the electromagnetic far field. The coupling of a plasmon mode to incident electromagnetic radiation is proportional to the square of the dipole moment of the plasmon mode. A bright plasmon mode is a plasmon mode with a large dipole moment and a dark plasmon mode is a plasmon mode with a small dipole moment. For the case of a nanoshell composed of a core nanoparticle with a low dielectric permittivity such as vacuum or silica, the cavity plasmon is at a higher energy than the sphere plasmon. In this case the low energy hybridized plasmon is a bright plasmon, being more “spherelike”, and the high energy hybridized plasmon is a dark plasmon, being more “cavitylike”. In this low permittivity regime, the extinction spectrum is dominated entirely by the low energy bonding nanoshell plasmon. For increasing shell thickness, the interaction between the cavity and sphere modes decreases, resulting in a blueshift of the bonding mode and a redshift of the antibonding mode (Fig. 7.3A). For the case of a high permittivity core material such as

iron oxide, the cavity plasmon is redshifted to an energy below that of the sphere plasmon (Fig. 7.3B). In this regime the higher energy antibonding nanoshell plasmon will have the largest excitation cross-section, since it consists primarily of the dipole-active sphere plasmon. However, the lower energy bonding plasmon with its dominant contribution of the cavity plasmon will also be present in the spectrum. The primitive cavity plasmon acquires a dipole moment in the presence of the core. For increasing shell thickness, the high energy bright antibonding plasmon will redshift and the low energy bonding plasmon will blueshift. The experimentally observed spectral redshift with increasing shell layer thickness is, therefore, consistent with the case of a nanoshell with a large permittivity core material, and agrees with the plasmonic properties of other iron oxide core-Au shell nanoparticles that have been reported.<sup>279,283</sup>

To better understand the plasmonic properties of our wüstite-core Au-shell nanoparticles, we investigated the effects of the various core shapes fabricated on the plasmonic properties of spherical core-shell nanoparticles using the Finite-Difference Time-Domain (FDTD) method. A realistic gold dielectric function was used in these calculations.<sup>51,286</sup> A comparison of the extinction spectra for nanoshells of spherical, cubic, and concave cubic cores which have the same core and shell volumes is shown in Figure 7.4A, for the case of a low permittivity core (silica), and Figure 7.4B, for a model high permittivity core case ( $\epsilon = 12.0$ ). For a silica core material (Fig. 7.4A), the dipolar resonances for the nanoparticles with cubic and concave cubic cores are slightly redshifted compared to the nanoshell with a spherical core. For the cubic core, and more strongly for the concave cubic core, an additional quadrupolar plasmon resonance appears at nominally 540 nm. Figure 7.4B shows the calculated spectra for the same

structures in Figure 7.4A, but with cores filled with an  $\epsilon = 12.0$  artificial material. In this case, the bonding modes of the cubic and concave cubic cores are damped and higher order modes are excited. The experimentally observed plasmon mode is the antibonding dipolar resonance, which is the main resonance in the concave cubic core case.

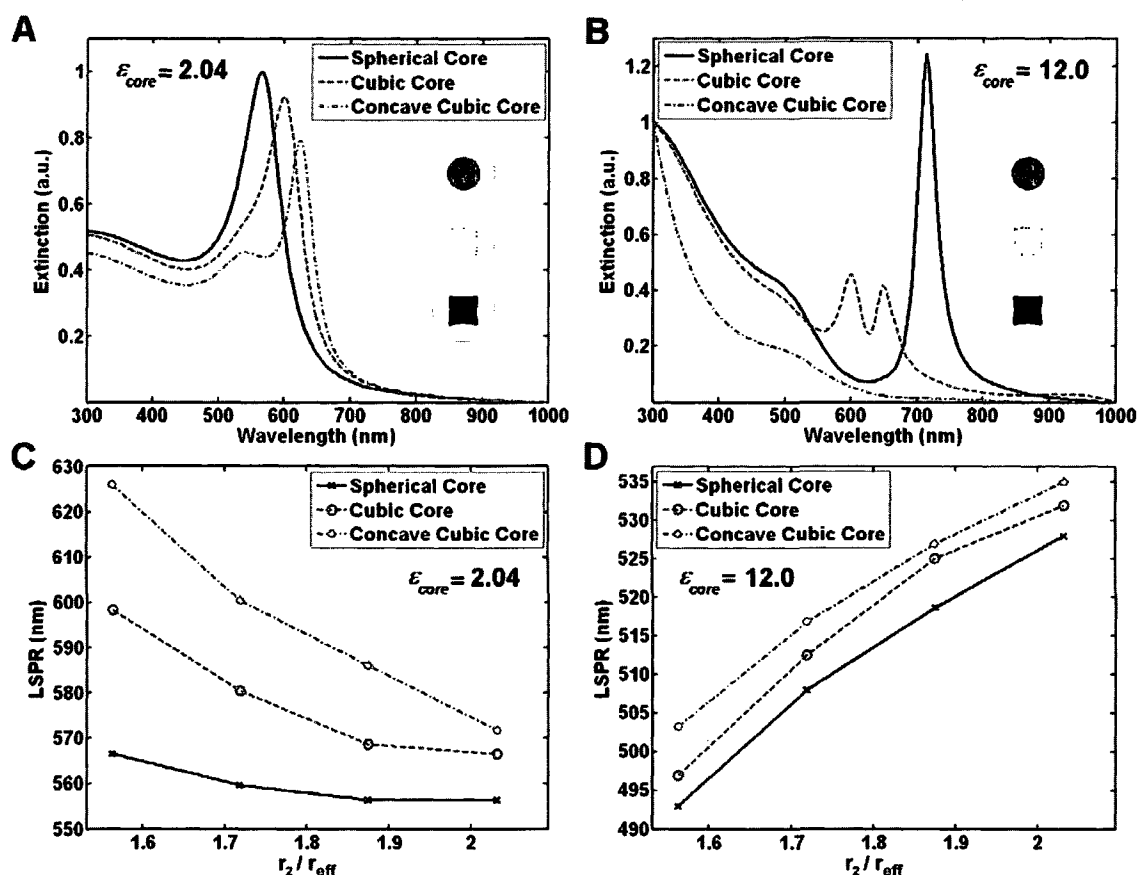


**Figure 7.4:** (A,B) Theoretical comparison of extinction spectra for nanoshells with cores of different shapes: spherical (blue solid line), cubic (red dashed line), and concave cubic (green dash-dotted line). The outer radius of the shell is  $r_2 = 50$  nm and the effective radius of the core is  $r_{\text{eff}} = 32$  nm. The core dielectrics are (A) silica ( $\epsilon = 2.04$ ) and (B) an artificial material with  $\epsilon = 12.0$ . (C,D) Calculated LSPR shifts of the (C) bonding dipolar nanoshell resonances for a silica core and (D) antibonding dipolar nanoshell resonances for an artificial core with  $\epsilon = 12.0$ , as a function of the ratio of the outer radius of the shell,  $r_2$ , to the effective core radius  $r_{\text{eff}} = 32$  nm.

The differences in the optical properties of core-shell plasmonic nanoparticles introduced by a nonspherical core are due to the reduction of symmetry introduced by the

variations in core geometries. For a system of spherical symmetry, only primitive plasmons of the same multipolar symmetry interact and hybridize.<sup>287,288</sup> The spectrum for the spherical core in Figure 7.4A, for example, displays only dipolar nanoshell resonances due to the hybridization of the dipolar sphere plasmon mode with the dipolar cavity plasmon mode. When the spherical symmetry of the core is broken, however, primitive plasmons of different multipolar symmetry can interact, resulting in the appearance of new modes in the spectrum due to the mixing of, for example, dipolar sphere plasmon modes with higher order cavity plasmon modes. This additional interaction also leads to larger shifts of the hybridized plasmon resonances. For the cubic silica core spectrum shown in Figure 7.4A, the symmetry breaking is relatively weak and results in a redshift of the dipole resonance and the appearance of a weak quadrupolar resonance discerned as a slight shoulder at 540 nm on the short wavelength side of the dipolar resonance. For the concave cubic core, this effect is stronger, resulting in a more significant redshift of the dipolar mode and the appearance of a clearly distinguishable quadrupolar plasmon resonance at 540 nm. The calculated localized surface plasmon resonance (LSPR) shifts of the bonding dipolar nanoshell resonance as a function of shell thickness for the three different silica core shapes is shown in Figures 7.4C,D, for low (*e.g.*, silica) and high permittivity cores, respectively. To allow for a meaningful comparison of the optical properties of nanoshells of different core shapes, an effective core radius  $r_{\text{eff}}$ , defined as the radius of a spherical core of the same volume as the actual core, is used. For the silica permittivity case, a blueshift of the bonding nanoshell resonance is clearly observed with increasing shell thickness: for the high permittivity case, the opposite trend is observed. The qualitative features of these wavelength shifts

do not depend strongly on the detailed shape of the core. (Local field enhancements for the lowest order dipolar modes of the structures depicted in Figure 7.4 are shown in Figure 7.5) This analysis reveals that the shape of the dielectric core has only a minor influence on the extinction spectra and that core geometry does not affect the experimentally observed shell thickness dependent plasmon wavelength shifts.

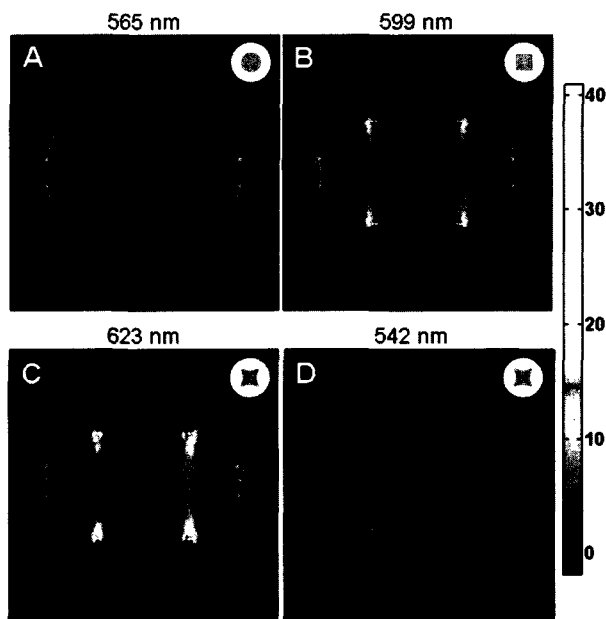


**Figure 7.5:** Comparison of the electric field enhancement distribution in an equatorial plane through the center of the three different nanoshells. The dipolar modes ( $l = 1$ ) are shown for (A) spherical, (B) cubic, and (C) concave cubic cores at 565 nm, 599 nm, and 623 nm, respectively. (D) The quadrupole mode ( $l = 2$ ) is shown for the concave cubic core geometry at 542 nm. The parameters used in this simulations are the same as Figure 7.4A. Inset shows the nanoparticle shape.

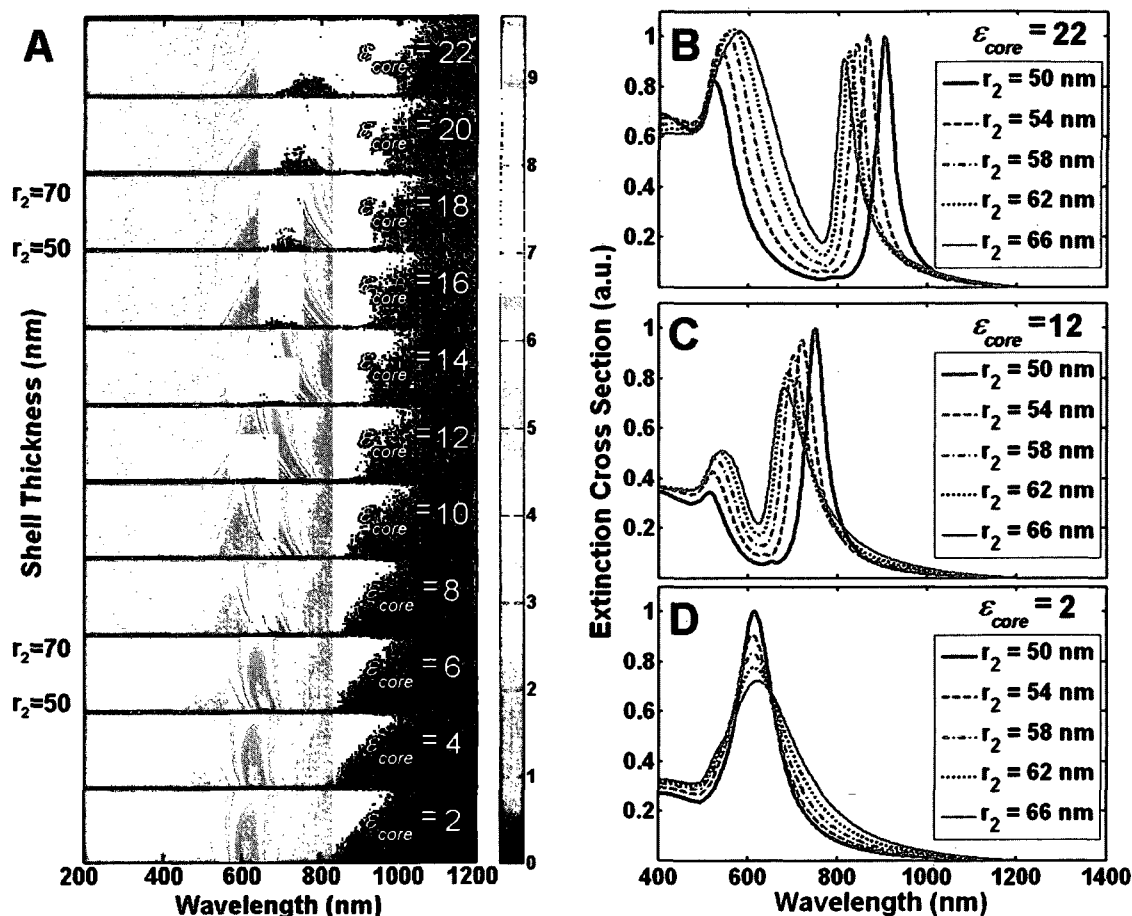


**Figure 7.6:** (A) Theoretical color contour representation of the extinction spectra for different core dielectric permittivities and shell thicknesses for the same effective core radius of  $r_{eff} = r_1 = 36$  nm. Each panel shows the extinction spectra for a fixed  $\epsilon_{core}$  with the shell radius increasing from  $r_2 = 50$  to  $r_2 = 70$  nm. The color corresponds to the extinction cross-section values normalized to the maximum extinction value. The surrounding medium is water (dielectric constant of 1.77). (B-D) Theoretically calculated extinction spectra for spherical nanoshells with different shell thicknesses (where  $r_{eff} = r_1 = 36$  nm) normalized to the thinnest shell extinction peak, using a (B) high core dielectric permittivity of 22, (C) core dielectric permittivity of 12, and (D) low core dielectric permittivity of 2. The bright mode does not significantly shift in (D) and redshifts in (B) to higher wavelengths. The best match to the experimental data behavior is shown in (C).

Based on this analysis, the dielectric permittivity of the core material, not the shape of the core, is a major controlling factor in the plasmon resonant response of core-shell nanoparticles. We can take advantage of the dependence of the plasmonic



properties on core permittivity to estimate the dielectric properties of the core nanomaterial. This is important, since it provides a method for measuring the dielectric permittivity of nanocrystals or nanoparticles. This method is limited to study dielectrics around which a plasmonic shell is grown. Despite the limited accuracy of this approach, it is to our knowledge the only available method for estimating the dielectric properties of nanocrystals or nanoparticles, which may differ significantly from the dielectric properties of the bulk phases of the material. This is particularly of interest for the case of exotic nanomaterials, such as wüstite nanocrystals, where mixed oxidation states of iron oxide may be intentionally or unintentionally introduced into the nanostructure. To examine the core permittivity dependence of the plasmonic properties, the plasmon resonant response of Au nanoshells with a spherical core for a large range of core permittivities was calculated using Mie theory (Fig. 7.6). Core permittivities ranging from  $\epsilon = 2$  to  $\epsilon = 22$  were calculated for the same size core-shell nanostructures. In each case, the core radius was  $r_1 = 36$  nm, and the outer radius of the nanoparticle  $r_2$  was varied between 50 and 70 nm (Fig. 7.6A). From this comprehensive mapping of the plasmonic properties of the core-shell structure, we can clearly observe the thickness-dependent plasmon resonant wavelength shifts and their dependence on core permittivity. From the waterfall plots of Figure 7.6A, we see that for lower values of the core permittivity there is essentially no wavelength shift of the plasmon resonance for the  $r_1$  and  $r_2$  values studied. As the core permittivity is increased, however, several changes in the plasmonic properties are introduced. Figures 7.6B, C, and D show representative spectra extracted from the waterfall plots of Figure 7.6A for cores with  $\epsilon = 2$ , 12, and 22, for qualitative comparison to our experimental spectra. In these spectra we see that for core

permittivities smaller than 8, the low energy bonding mode always blueshifts and is attenuated with increasing shell thickness. For core permittivities larger than 8, the antibonding mode becomes visible, and a strong redshift of this mode with increasing shell thickness is apparent for core permittivities of 10 and above. Although the experimentally determined permittivities for bulk wüstite and magnetite are smaller than 8 in the wavelength region of interest,<sup>289</sup> simulations modeling the core using bulk permittivity values, or a combination of both, do not show qualitative agreement with our experimental observations. The best match to our experimental data is found for  $\epsilon = 12$  (Fig. 7.6C). From these observations we conclude that the effective permittivity of our nanocrystalline cores is quite likely in the  $\epsilon = 10$ -14 range, significantly larger than bulk permittivity measurements which range from  $\epsilon = 4.8$  to 5.8 for wüstite and  $\epsilon = 5.5$  to 6.1 for magnetite in our wavelength range.<sup>289,290</sup>

To determine the crystallinity and structure of the iron oxide core nanoparticles in the nanoshell composites, powder X-ray diffraction (XRD) was utilized. As shown in Figure 7.7, the peak position and relative intensity of all diffraction peaks for the three products match well with standard powder diffraction data. The wüstite peaks correlate with a cubic phase with cell parameters  $a = c = 4.32 \text{ \AA}$  and space group  $Fm\bar{3}m$  (225) (JCPDS card no. 98-000-0464). The presence of additional peaks in the XRD spectra (Fig. 7.7 A,B) shows a slight oxidation of wüstite to magnetite. The existence of magnetite in the XRD spectra of the particles is due to mild oxidation of the outermost layer of the originally formed metastable wüstite nanoparticles. After decomposition, these particles are exposed to air, which results in the formation of a thin layer of magnetite on the surface and edges of the particles. Since both magnetite and maghemite

( $\gamma$ -Fe<sub>2</sub>O<sub>3</sub>; P4<sub>3</sub>32; no.212; a = 8.346 Å) have the same cubic inverse spinel structure and unit cells with only *ca.* 1% difference,<sup>291</sup> Raman spectroscopy (Fig. 7.8) was used to confirm that maghemite was not present.<sup>292</sup> The magnetite crystals present in the iron oxide cores have a cubic phase with cell parameters a = c = 8.3969 Å and space group  $Fd\bar{3}m$  (227) (JCPDS card no. 98-000-0294). Our group has previously published detailed characterization including dark field TEM images and selected area electron diffraction patterns for single crystals prepared under the same reaction conditions in Hofmann *et al.*<sup>275</sup> The reported data presents unequivocal evidence that the core of the nanoparticle is composed of wüstite and the distribution of magnetite is concentrated to the corners and edges. Interestingly, the Fe<sub>3</sub>O<sub>4</sub> domains exist within the predominant Fe<sub>x</sub>O crystal lattice of the nanoparticle and remain aligned with it. Once the iron oxide is functionalized and decorated with small Au nanoparticles for Au shell layer growth, a small peak attributed to gold can be observed (Fig. 7.7A ii). When a continuous Au shell is formed on the particles (with a thickness of 10.9 nm), the diffraction from Au dominates the pattern (Fig. 7.7A iii), due to its high electron density.<sup>293</sup> The Au diffraction peaks indicate a cubic phase of Au with cell parameters a = c = 4.0786 Å and space group  $Fm\bar{3}m$  (225) (JCPDS card no. 98-000-0230).

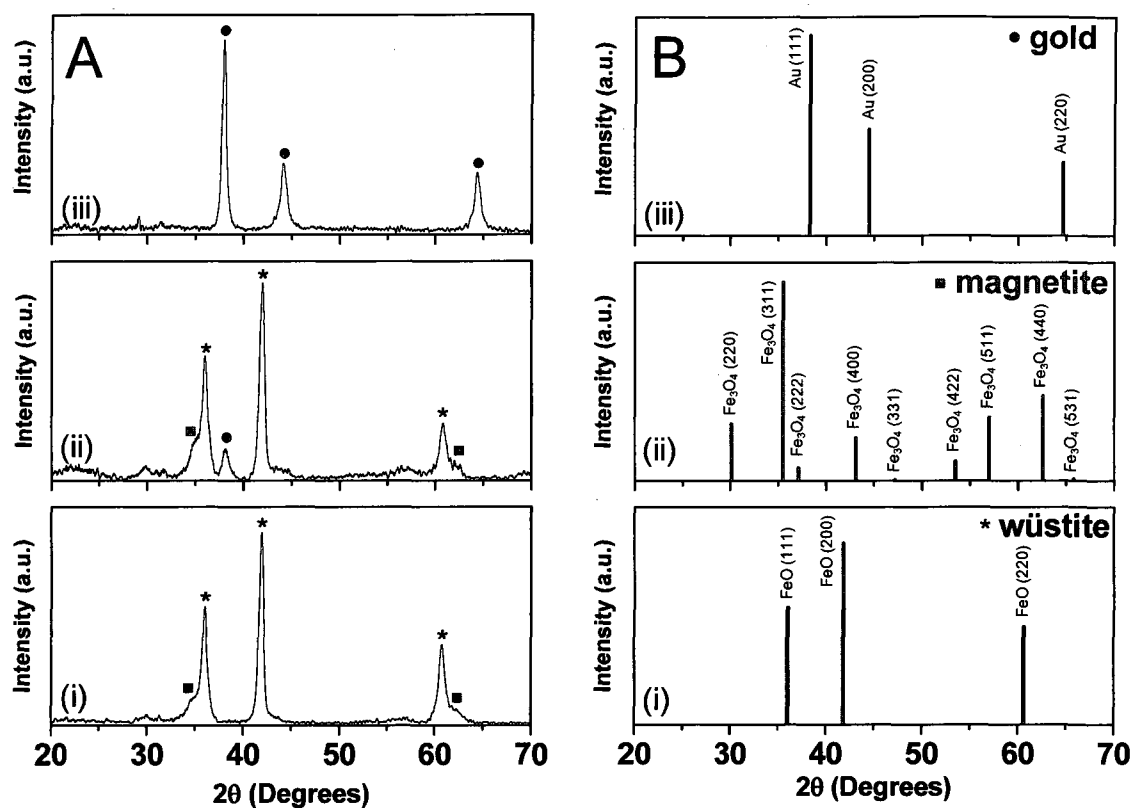


**Figure 7.7:** Powder X-ray diffraction patterns for (i) iron oxide core nanoparticles (tetracubes), (ii) Au nanoparticle decorated precursors, and (iii) Au coated iron oxide nanoparticles (with 10.9 nm shell thickness). (B) XRD peak positions for (i) wüstite, (ii) magnetite, and (iii) gold.

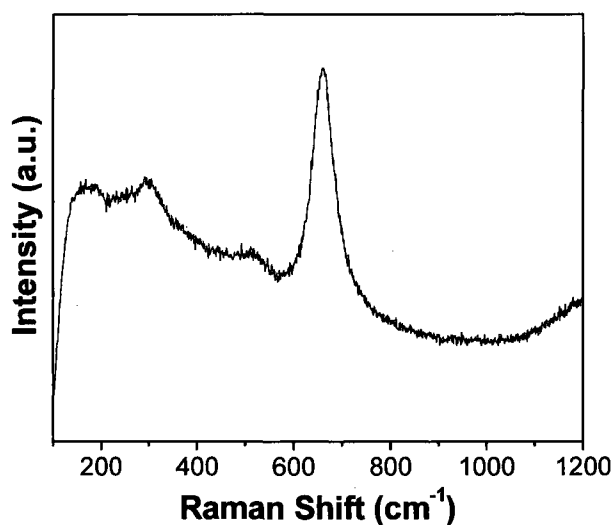


**Figure 7.8:** Raman spectrum of iron oxide nanoparticles (785 nm, 1.5 mW). The wüstite (Fe<sub>x</sub>O) phase undergoes mild oxidation to magnetite (Fe<sub>3</sub>O<sub>4</sub>).<sup>292</sup>

To test if the particles were macroscopically magnetic, a permanent magnet was placed adjacent to the vials of Au-decorated iron oxide precursors and Au-coated iron oxide nanoparticles (Fig. 7.9A). The materials were attracted to the magnet, leaving the solutions transparent. A high magnification SEM image (Fig. 7.9B), representative of the nanoparticles shown in Figure 7.9A, verifies that the particles are magnetic even with a complete, continuous Au coating.

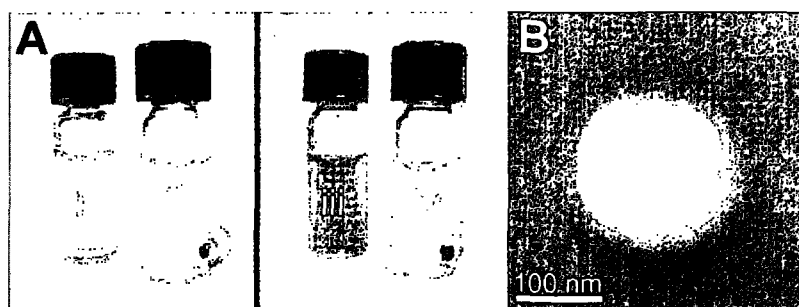


**Figure 7.9:** (A) Optical images of (i) Au-decorated iron oxide precursor particles, (ii) Au-decorated iron oxide precursor particles with magnet, (iii) Au coated nanoparticles, and (iv) Au coated nanoparticles with magnet. (B) Representative SEM image of the shells shown in (iv).

Since the various iron oxides possess different magnetic properties, magnetic measurements were performed to better characterize the magnetic properties of this mixed oxide system. Magnetite is a well-known ferrimagnetic material, while wüstite is antiferromagnetic or weakly ferrimagnetic. In ferrimagnetic materials, the magnetic moments of the two sublattices align antiparallel, but do not cancel. This type of magnetic ordering differs from ferromagnetism and antiferromagnetism, where in the former, all of the magnetic ions align parallel to each other, and in the latter, there are two sublattices with magnetic moments exactly equal but which align antiparallel, and the net

moment is zero in zero magnetic field. Alignments of these sublattices occur below a certain critical temperature, called the Curie temperature  $T_C$  (for ferromagnets and ferrimagnets) or the Néel temperature  $T_N$  (for antiferromagnets).

Magnetite has a Curie temperature ( $T_C$ ) of 858 K,<sup>294</sup> where  $T_C$  is defined as the temperature above which a ferromagnetic or ferrimagnetic material becomes paramagnetic.<sup>295</sup> A paramagnetic material requires an externally applied magnetic field to retain any magnetization. Wüstite has a Néel temperature ( $T_N$ ) of  $\sim 195$  K,<sup>296</sup> where  $T_N$  is defined as the temperature above which an antiferromagnetic material becomes paramagnetic.<sup>297</sup> For wüstite, this change from an antiferromagnetic or weakly ferrimagnetic material to a paramagnetic material is accompanied by a change in crystal structure from monoclinic or rhombohedral to a cubic phase.<sup>269</sup> When an external field is applied to an antiferromagnetic material, a slow increase of the magnetic moment with field is to be expected; however, in a ferrimagnetic material, the magnetic moments align with the external field and cause a net magnetization. Therefore, any magnetic behavior of these nanoparticles below  $T_C$  is expected to be dominated by the presence of magnetite, which will have the largest magnetization.

Field-dependent magnetization measurements  $M(H)$  were performed at two temperatures,  $T = 100$  K and 250 K, (Fig. 7.10) chosen to confirm that at different temperatures below the  $T_C = 858$  K, similar results are observed. Zero field-cooled (ZFC) magnetization measurements as a function of temperature  $M(T)$  (Fig. 7.11) show that at 300 K there is still an increase in magnetization. Above a temperature where the system enters the superparamagnetic state (known as the blocking temperature) a maximum should be expected in  $M(T)$ . The absence of such a local maximum in our

M(T) data (Fig. 7.11) indicates that the material has not yet entered a superparamagnetic state. The magnetization measurements M(H) shown in Figure 7.10 indicate that there is no significant change in the coercivity of uncoated and coated iron oxide particles. The coercivity of the materials is  $58.5 \pm 3.7$  mT at 100 K and  $35.7 \pm 0.2$  mT at 250 K for the uncoated particles and  $51.7 \pm 1.7$  mT at 100 K and  $33.9 \pm 0.2$  mT at 250 K for those coated with an Au shell layer. At the maximum field for these measurements ( $H = 5$  T), the magnetization still has a small positive slope, and, therefore, the saturation magnetization can be expected to be slightly higher than that at 5 T. The remanent magnetization of the iron oxide nanoparticles is  $0.837 \pm 0.0523$  emu/g at 100 K and  $0.866 \pm 0.00424$  emu/g at 250 K for the uncoated particles and  $0.0371 \pm 0.000848$  emu/g at 100 K and  $0.0343 \pm 0.000495$  emu/g at 250 K for the Au coated nanoparticles. The decrease in the remanent magnetization results from the addition of a non-magnetic mass, that is, the Au layer.

While ultrasmall Au nanoparticles have demonstrated ferromagnetism,<sup>298</sup> at diameters larger than 4 nm, the magnetism reverts back to that of the bulk state Au,<sup>299</sup> where Au is known to have diamagnetic properties. For thin Au films on glass and polypropylene, a diamagnetic response is characterized by a linear relationship between magnetization and applied field:  $M \propto -H$ .<sup>300</sup> However, for these gold coated iron oxide nanoparticles, a hysteresis loop can be observed as shown in the insets of Figure 7.10 A,B. Therefore, the typical magnetic behavior of bulk gold is not observed in these samples, and after Au coating, the nanoparticle still exhibits ferrimagnetic behavior.

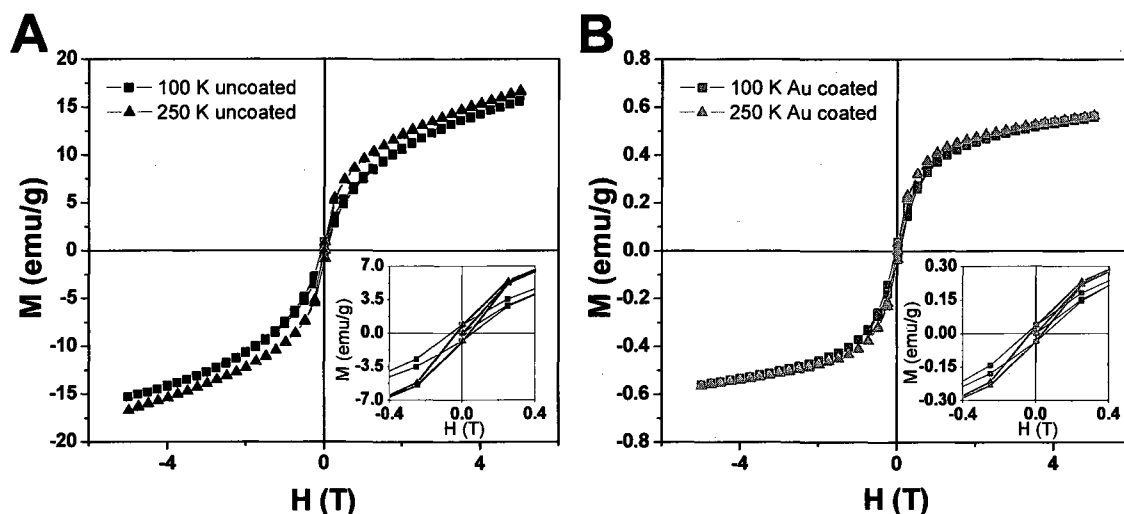


**Figure 7.10:** Magnetization as a function of magnetic field at constant temperature (100 K or 250 K) for (A) uncoated and (B) Au coated iron oxide nanoparticles (tetragonal, with 10.9 nm shell thickness, where insets show the magnetic hysteresis).

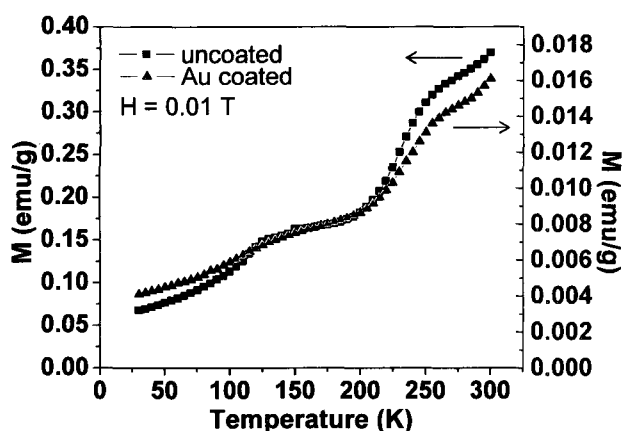


**Figure 7.11:** Magnetization measurements as a function of temperature for uncoated and Au coated iron oxide nanoparticles (tetragonal with 10.9 nm shell thickness).

## 7.4: Conclusions

We have shown that nanoparticles consisting of a wüstite core with magnetite-rich corners and edges can be coated with a continuous gold shell in aqueous solution at room temperature. The procedure converts hydrophobic iron oxide nanoparticles to water soluble Au coated bifunctional nanoparticles and can be extended to the immobilization of other noble metals. The Au shell provides a surface for chemical



functionality and long-term stabilization of the core material. Additionally, controlled oxidation of metastable wüstite by varying exposure of the particles to different environmental conditions allows for tunability over the materials' magnetic properties while varying the Au shell thickness provides tunability of the plasmonic properties. Theoretical analysis of the plasmonic properties of these nanoparticles suggests that the plasmonic redshift that occurs with increasing Au shell thickness is due to a large dielectric permittivity of the core. Based on our simulations we estimate the core nanocrystal permittivity to be in the  $\epsilon = 10-14$  range, larger than the bulk permittivities of wüstite and magnetite previously reported. The exhibited ferrimagnetic properties of the composites before and after Au coating can be quite useful in biomedical applications, for separation processes and as MRI contrast agents. Since magnetic core-shell nanostructures have been shown to assemble under an applied magnetic field,<sup>301</sup> assembly of the nanoparticles into arrays or superlattices could be utilized to study plasmon coupling in long-range periodic structures, which may lead to the development of new types of photonic-magnetic nanodevices.

## **Chapter 8: Summary**

SERS has proven to be a highly useful tool to probe the structure and organization of molecules adsorbed on nanoshells. Silica-Au nanoshell substrates were chosen due to their well-controlled and reproducible geometry as well as their ability to generate large electromagnetic fields near the nanoshell plasmon resonance frequency on their surface. This intense near field, along with the inherent roughness of nanoshells resulting from the fabrication process, provide the necessary enhancement mechanism to achieve strong SERS signals.

In this thesis, nanoshell-based SERS substrates were explored for a variety of potential uses. In the case of a modified PEG linker, a method for determining molecular conformation of molecules on nanoparticle surfaces, based on quantifying adsorbate coverage on the nanoshell surface using SERS, was demonstrated. Au nanoshells modified with a pH sensitive molecular adsorbate molecule were shown to function as an optical nano pH meter. While Au nanoshells functionalized with alkanethiol-based monolayers resulted in intense SERS spectra peaks that depend on the chain length of the molecule and are due to the coupling of the gold-sulfur bond stretch with the longitudinal acoustic mode of the molecular alkane chain. Phospholipid monolayers deposited on top of alkanethiol monolayers chemisorbed on nanoshells, known as hybrid bilayers, mimic biological membranes and were proven useful for the spectral monitoring of membrane intercalants.

In the examination of non-thiolated analyte molecules, the SERS response was exploited to determine the analyte's preferred adsorption and orientation on Au nanoshells. Molecules containing the three halides: chloride, bromide, and iodide, exhibited low frequency stretching vibrations that were used to calculate the approximate force constants for these Au-halide complexes. Aromatic probes containing oxygen and nitrogen functional groups were shown to chemisorb onto nanoshells and interact with the metal surface either through their  $\pi$  electrons, assuming a flat orientation, or via their lone pair electrons in end-on attachment. High frequency SERS spectra of analytes with submonolayer coverages on Au nanoshells displayed evidence for the atop adsorption of carbon monoxide. Overall, the SERS spectral response of molecules on Au nanoshell

substrates has yielded vibrational peak intensities and shifts which provide good indicators of surface bound species and their structure.

Future directions for this work are many, ranging from developing new plasmonic substrate geometries that cooperatively optimize SERS and SEIRA enhancements to inventing new instrumentation for rapid, combined SERS and SEIRA detection. As our understanding and ability to control various nanoscale parameters improves, we will increase our capability to generate plasmonic devices designed to elicit a strong spectroscopic response.

More immediate SERS related research projects include assignment of the broad shoulder around  $300\text{-}350\text{ cm}^{-1}$  in the spectra of short chain alkanethiols and theoretical modeling of the SERS spectra for different dithiol conformations on Au surfaces. Temperature controlled SERS measurements above and below the lipid main phase transition temperature may show spectral differences in analyte partitioning into hybrid bilayers. SERS spectral mapping of CO adsorption on nanoshells along with corresponding topographic images could lead to the local assignment of CO bonding to nanoshell defect sites. Finally, angle-resolved and single particle SERS measurements in addition to theoretical simulations will allow for more correlations to be made between plasmon resonances and Raman enhancements.

The demonstrated synthesis and plasmonic properties of bifunctional nanoshells containing a magnetic iron oxide core may lead to hybrid plasmonic magnetic materials for combined multimodal imaging and photothermal therapy. Future work includes varying the thickness of the oxide layer to tune the magnetic properties and optimize their application in MRI imaging, drug delivery, or data storage. Two- or three- dimensional

alignment of the synthesized particles provides other avenues to investigate plasmonic coupling in this mixed iron oxide system.

Interactions between molecules and materials form the basis for a number of applications in the scientific field. These broadly range from environmental and biomedical applications to detection, defense, and security. The desire for researchers to fundamentally understand and characterize the interactions between molecules and nanostructures will make the emerging field of plasmonics a mature interdisciplinary area of research that exploits the exciting phenomena associated with surface plasmons.

## References

- (1) Raman, C. V.; Krishnan, K. S. *Nature* **1928**, *122*, 169.
- (2) Harris, D. C.; Bertolucci, M. D. *Symmetry and Spectroscopy: An Introduction to Vibrational and Electronic Spectroscopy*; Dover Publications, 1989.
- (3) Gardiner, D. J. *Practical Raman Spectroscopy*; Springer-Verlag, 1989.
- (4) Haynes, C. L.; McFarland, A. D.; Van Duyne, R. P. *Anal. Chem.* **2005**, *77*, 338A-346A.
- (5) Kneipp, J.; Kneipp, H.; Kneipp, K. *Proc. Nat. Acad. Sci. U.S.A.* **2006**, *103*, 17149-17153.
- (6) Rusakova, I.; Ould-Ely, T.; Hofmann, C.; Prieto-Centurion, D.; Levin, C. S.; Halas, N. J.; Luttge, A.; Whitmire, K. H. *Chem. Mater.* **2007**, *19*, 1369-1375.
- (7) Kudelski, A. *Vib. Spec.* **2005**, *39*, 200-213.

- (8) Jeanmaire, D. L.; Van Duyne, R. P. *J. Electroanal. Chem.* **1977**, *84*, 1-20.
- (9) Albrecht, M. G.; Creighton, J. A. *J. Am. Chem. Soc.* **1977**, *99*, 5215-5217.
- (10) Campion, A.; Kambhampati, P. *Chem. Soc. Rev.* **1998**, *27*, 241-250.
- (11) Jensen, T. R.; Malinsky, M. D.; Haynes, C. L.; Van Duyne, R. P. *J. Phys. Chem. B* **2000**, *104*, 10549-10556.
- (12) Kreibig, U.; Vollmer, M. *Optical Properties of Metal Clusters*; Springer-Verlag: Heidelberg, Germany, 1995; Vol. 25.
- (13) Raether, H. *Surface Plasmons*; Springer: Berlin, 1988.
- (14) Baumberg, J. J.; Kelf, T. A.; Sugawara, Y.; Cintra, S.; Abdelsalam, M. E.; Bartlett, P. N.; Russell, A. E. *Nano Lett.* **2005**, *5*, 2262-2267.
- (15) Kneipp, K.; Kneipp, H.; Itzkan, I.; Dasari, R. R.; Feld, M. S. *Chem. Rev.* **1999**, *99*, 2957-2976.
- (16) Wang, H.; Levin, C. S.; Halas, N. J. *J. Am. Chem. Soc.* **2005**, *127*, 14992-14993.
- (17) Ward, D. R.; Grady, N. K.; Levin, C. S.; Halas, N. J.; Wu, Y.; Nordlander, P.; Natelson, D. *Nano Lett.* **2007**, *7*, 1396-1400.
- (18) Lal, S.; Grady, N. K.; Kundu, J.; Levin, C. S.; Lassiter, J. B.; Halas, N. J. *Chem. Soc. Rev.* **2008**, *37*, 898-911.
- (19) Wanzenböck, H. D.; Mizaikoff, B.; Weissenbacher, N.; Kellner, R. *Fresenius J. Anal. Chem.* **1998**, *362*, 15-20.
- (20) Osawa, M.; Ataka, K.; Yoshii, K.; Nishikawa, Y. *Appl. Spectrosc.* **1993**, *47*, 1497-1502.
- (21) Enders, D.; Rupp, S.; Küller, A.; Pucci, A. *Surf. Sci.* **2006**, *600*, L305-L308.

- (22) Le, F.; Brandl, D. W.; Urzhumov, Y. A.; Wang, H.; Kundu, J.; Halas, N. J.; Aizpurua, J.; Nordlander, P. *ACS Nano* **2008**, *2*, 707-718.
- (23) Pelton, M.; Aizpurua, J.; Bryant, G. *Laser & Photon. Rev.* **2008**, *2*, 136-159.
- (24) Lassiter, J. B.; Aizpurua, J.; Hernandez, L. I.; Brandl, D. W.; Romero, I.; Lal, S.; Hafner, J. H.; Nordlander, P.; Halas, N. J. *Nano Lett.* **2008**, *8*, 1212-1218.
- (25) Osawa, M. *Topics Appl. Phys.* **2001**, *81*, 163-187.
- (26) Schatz, G. C. *Acc. Chem. Res.* **1984**, *17*, 370-376.
- (27) Averitt, R. D.; Sarkar, D.; Halas, N. J. *Phys. Rev. Lett.* **1997**, *78*, 4217-4220.
- (28) Oldenburg, S. J.; Averitt, R. D.; Westcott, S. L.; Halas, N. J. *Chem. Phys. Lett.* **1998**, *288*, 243-247.
- (29) Prodan, E.; Radloff, C.; Halas, N. J.; Nordlander, P. *Science* **2003**, *302*, 419-422.
- (30) Prodan, E.; Nordlander, P. *Nano Lett.* **2003**, *3*, 543-547.
- (31) Prodan, E.; Nordlander, P. *J. Chem. Phys.* **2004**, *120*, 5444-5454.
- (32) Tam, F.; Chen, A. L.; Kundu, J.; Wang, H.; Halas, N. J. *J. Chem. Phys.* **2007**, *127*.
- (33) Hirsch, L. R.; Jackson, J. B.; Lee, A.; Halas, N. J.; West, J. L. *Anal. Chem.* **2003**, *75*, 2377-2381.
- (34) Sershen, S.; Westcott, S. L.; Halas, N. J.; West, J. L. *J. Biomed. Mater. Res.* **2000**, *51*, 293-298.

(35) Hirsch, L. R.; Stafford, R. J.; Bankson, J. A.; Sershen, S. R.; Rivera, B.; Price, R. E.; Hazle, J. D.; Halas, N. J.; West, J. L. *Proc. Nat. Acad. Sci. U.S.A.* **2003**, *100*, 13549-13554.

(36) Loo, C.; Lin, A.; Hirsch, L.; Lee, M. H.; Barton, J.; Halas, N.; West, J.; Drezek, R. *Technol Cancer Res T* **2004**, *3*, 33-40.

(37) Loo, C.; Lowery, A.; Halas, N.; West, J.; Drezek, R. *Nano Lett.* **2005**, *5*, 709-711.

(38) O'Neal, D. P.; Hirsch, L. R.; Halas, N. J.; Payne, J. D.; West, J. L. *Cancer Lett.* **2004**, *209*, 171-176.

(39) Bickford, L. R.; Chang, J.; Fu, K.; Sun, J.; Hu, Y.; Gobin, A.; Yu, T.-K.; Drezek, R. A. *NanoBioTechnology* **2008**, 1-8.

(40) Choi, M.-R.; Stanton-Maxey, K. J.; Stanley, J. K.; Levin, C. S.; Bardhan, R.; Akin, D.; Badve, S.; Sturgis, J.; Robinson, J. P.; Bashir, R.; Halas, N. J.; Clare, S. E. *Nano Lett.* **2007**, *7*, 3759-3765.

(41) Sarkar, D.; Halas, N. J. *Phys. Rev. E* **1997**, *56*, 1102-1112.

(42) Jackson, J. B.; Westcott, S. L.; Hirsch, L. R.; West, J. L.; Halas, N. J. *Appl. Phys. Lett.* **2003**, *82*, 257-259.

(43) Jackson, J. B.; Halas, N. J. *Proc. Nat. Acad. Sci. U.S.A.* **2004**, *101*, 17930-17935.

(44) Halas, N. J. *MRS Bulletin* **2005**, *30*, 362-367.

(45) Talley, C. E.; Jackson, J. B.; Oubre, C.; Grady, N. K.; Hollars, C. W.; Lane, S. M.; Huser, T. R.; Nordlander, P.; Halas, N. J. *Nano Lett.* **2005**, *5*, 1569-1574.

(46) Kundu, J.; Le, F.; Nordlander, P.; Halas, N. J. *Chem. Phys. Lett.* **2008**, *452*, 115-119.

(47) Wang, H.; Kundu, J.; Halas, N. J. *Angew. Chem. Int. Ed.* **2007**, *46*, 9040.

- (48) Moskovits, M. *Rev. Mod. Phys.* **1985**, *57*, 783-826.
- (49) Moskovits, M. *J. Chem. Phys.* **1982**, *77*, 4408-4416.
- (50) Stöber, W.; Fink, A.; Bohn, E. *J. Colloid and Interface Sci.* **1968**, *26*, 62-69.
- (51) Johnson, P. B.; Christy, R. W. *Phys. Rev. B* **1972**, *6*, 4370-4379.
- (52) Van Helden, A. K.; Jansen, J. W.; Vrij, A. *J. Colloid and Interface Sci.* **1981**, *81*, 354-368.
- (53) van Blaaderen, A.; Vrij, A. *J. Colloid and Interface Sci.* **1993**, *156*, 1-18.
- (54) Chumanov, G.; Sokolov, K.; Gregory, B. W.; Cotton, T. M. *J. Phys. Chem.* **1995**, *99*, 9466-9471.
- (55) Levin, C. S.; Bishnoi, S. W.; Grady, N. K.; Halas, N. J. *Anal. Chem.* **2006**, *78*, 3277-3281.
- (56) Crawford, J. *Cancer Treat. Rev.* **2002**, *A*, 7-11.
- (57) Harris, J. M.; Martin, N. E.; Modi, M. *Clin. Pharmacokinet.* **2001**, *40*, 539-551.
- (58) Hafner, J., personal communication.
- (59) Marsh, D.; Bartucci, R.; Sportelli, L. *Biochim. Biophys. Acta* **2003**, *1615*, 33-59.
- (60) Mohri, N.; Matsushita, S.; Inoue, M. *Langmuir* **1998**, *14*, 2343-2347.
- (61) Demers, L. M.; Mirkin, C. A.; Mucic, R. C.; Reynolds, R. A.; Letsinger, R. L.; Elghanian, R.; Viswanadham, G. *Anal. Chem.* **2000**, *72*, 5535-5541.



- (62) Malicka, J.; Gryczynski, I.; Gryczynski, Z.; Lakowicz, J. R. *Anal. Biochem.* **2003**, *315*, 57-66.
- (63) Dulkeith, E.; Ringler, M.; Klar, T. A.; Feldmann, J.; Muñoz Javier, A.; Parak, W. J. *Nano Lett.* **2005**, *5*, 585-589.
- (64) Hermanson, G. T. *Bioconjugate Techniques*; Academic Press: San Diego, CA, 1996.
- (65) Haugland, R. P. *Handbook of Fluorescent Probes and Research Products, Ninth Edition*; Molecular Probes, Inc.: Eugene, OR, 2002.
- (66) Osawa, M.; Matsuda, N.; Yoshii, K.; Uchida, I. *J. Phys. Chem.* **1994**, *98*, 12702-12707.
- (67) Michota, A.; Bukowska, J. *J. Raman Spectrosc.* **2003**, *34*, 21-25.
- (68) Park, H.; Lee, S. B.; Kim, K.; Kim, M. S. *J. Phys. Chem.* **1990**, *94*, 7576-7580.
- (69) Wang, L.; Roitberg, A.; Meuse, C.; Gaigalas, A. K. *Spectrochim. Acta, Part A* **2001**, *57*, 1781-1791.
- (70) Attard, G.; Barnes, C. *Surfaces*; Oxford University Press: New York, NY, 2003.
- (71) Zhang, X.; M.A., Y.; Lyandres, O.; Van Duyne, R. P. *J. Am. Chem. Soc.* **2005**, *127*, 4484-4489.
- (72) Roth, P. G.; Boerio, F. J. *J. Polym. Sci., Part B: Polym. Phys.* **1987**, *25*, 1923-1933.
- (73) Gearheart, L. A.; Ploehn, H. J.; Murphy, C. J. *J. Phys. Chem. B* **2001**, *105*, 12609-12615.
- (74) Bedrov, D.; Pekny, M.; Smith, G. D. *J. Phys. Chem. B* **1998**, *102*, 996-1001.

(75) Wuelfing, W. P.; Gross, S. M.; Miles, D. T.; Murray, R. W. *J. Am. Chem. Soc.* **1998**, *120*, 12696-12697.

(76) Bishnoi, S. W.; Rozell, C. J.; Levin, C. S.; Gheith, M. K.; Johnson, B. R.; Johnson, D. H.; Halas, N. J. *Nano Lett.* **2006**, *6*, 1687-1692.

(77) Clark, H. A.; Barker, S. L. R.; Brasuel, M.; Miller, M. T.; Monson, E.; Parus, S.; Shi, Z.-Y.; Song, A.; Thorsrud, B.; Kopelman, R.; Ade, A.; Meixner, W.; Athey, B.; Hoyer, M.; Hill, D.; Lightle, R.; Philbert, M. A. *Sens. Actuators, B* **1998**, *51*, 12-16.

(78) Michalet, X.; Pinaud, F. F.; Bentolila, L. A.; Tsay, J. M.; Doose, S.; Li, J. J.; Sundaresan, G.; Wu, A. M.; Gambhir, S. S.; Weiss, S. *Science* **2005**, *307*, 538-544.

(79) Chen, J.; Saeki, F.; Wiley, B. J.; Cang, H.; Cobb, M. J.; Li, Z.-Y.; Au, L.; Zhang, H.; Kimmey, M. B.; Li, X. D.; Xia, Y. *Nano Lett.* **2005**, *5*, 473-477.

(80) Huang, X. H.; El-Sayed, I. H.; Qian, W.; El-Sayed, M. A. *J. Am. Chem. Soc.* **2006**, *128*, 2115-2120.

(81) Xu, S.; Ji, X.; Xu, W.; Zhao, B.; Dou, X.; Bai, Y.; Ozaki, Y. *J. Biomed. Opt.* **2005**, *10*, 031112.

(82) Lee, S. B.; Kim, K.; Kim, M. S. *J. Raman Spectrosc.* **1991**, *22*, 811-817.

(83) Talley, C. E.; Jusinski, L.; Hollars, C. W.; Lane, S. M.; Huser, T. *Anal. Chem.* **2004**, *76*, 7064-7068.

(84) Clark, H. A.; Hoyer, M.; Philbert, M. A.; Kopelman, R. *Anal. Chem.* **1999**, *71*, 4831-4836.

(85) Burges, C. J. C. In *Data Mining and Knowledge Discovery Handbook: A Complete Guide for Practitioners and Researchers*; Rokach, L., Maimon, O. S., Eds.; Springer Science & Business Media: New York, 2005, p 59-92.

(86) Ramakrishna, R. S.; Fernandopulle, M. E. *J. Inorg. Nucl. Chem.* **1971**, *33*, 1940-1942.

- (87) Martell, A. E.; Smith, R. M. *In Critical Stability Constants*; Plenum Press: New York, 1977.
- (88) Joo, T. H.; Kim, K.; Kim, M. S. *J. Phys. Chem.* **1986**, *90*, 5816-5819.
- (89) Moskovits, M.; Suh, J. S. *J. Phys. Chem.* **1984**, *88*, 1293-1298.
- (90) Wells, M.; Dermody, D. L.; Yang, H. C.; Kim, T.; Crooks, R. M.; Ricco, A. J. *Langmuir* **1996**, *12*, 1989-1996.
- (91) Gao, P.; Weaver, M. J. *J. Phys. Chem.* **1986**, *90*, 4057-4063.
- (92) Kwon, Y. J.; Son, D. H.; Ahn, S. J.; Kim, M. S.; Kim, K. *J. Phys. Chem.* **1994**, *98*, 8481-8487.
- (93) Varsanyi, G. *Assignments for Vibrational Spectra of Seven Hundred Benzene Derivatives*; Wiley: New York, 1974.
- (94) Smallbone, K.; Gavaghan, D. J.; Gatenby, R. A.; Maini, P. K. *J. Theor. Bio.* **2005**, *235*, 476-484.
- (95) Roweis, S. T.; Saul, L. K. *Science* **2000**, *290*, 2323-2326.
- (96) Hardle, W. *Applied Nonparametric Regression*; Cambridge University Press: Cambridge, U. K. , 1990.
- (97) Vaupel, P.; Kallinowski, F.; Okunieff, P. *Cancer Res.* **1989**, *49*, 6449-6465.
- (98) Levin, C. S.; Janesko, B. G.; Bardhan, R.; Scuseria, G. E.; Hartgerink, J. D.; Halas, N. J. *Nano Lett.* **2006**, *6*, 2617-2621.
- (99) Ullman, A. *Chem. Rev.* **1996**, *96*, 1533-1554.
- (100) Bain, C. D.; Troughton, E. B.; Tao, Y.-T.; Evall, J.; Whitesides, G. M.; Nuzzo, R. G. *J. Am. Chem. Soc.* **1989**, *111*, 321-335.

- (101) Yamada, R.; Uosaki, K. *Langmuir* **1998**, *14*, 855-861.
- (102) Chidsey, C. E. D.; Liu, G.-Y.; Rowntree, P.; Scoles, G. *J. Chem. Phys.* **1989**, *91*, 4421-4423.
- (103) Ulman, A.; Eilers, J. E.; Tillman, N. *Langmuir* **1989**, *5*, 1147-1152.
- (104) Beardmore, K. M.; Kress, J. D.; Grønbech-Jensen, N.; Bishop, A. R. *Chem. Phys. Lett.* **1998**, *286*, 40-45.
- (105) Gronbeck, H.; Curioni, A.; Andreoni, W. *J. Am. Chem. Soc.* **2000**, *122*, 3839-3842.
- (106) Krüger, D.; Fuchs, H.; Rousseau, R.; Marx, D.; Parrinello, M. *J. Chem. Phys.* **2001**, *115*, 4776-4786.
- (107) Zhang, L.; Goddard III, W. A.; Jiang, S. *J. Chem. Phys.* **2002**, *117*, 7342-7349.
- (108) Yourdshahyan, Y.; Rappe, A. M. *J. Chem. Phys.* **2002**, *117*, 825-833.
- (109) Bryant, M. A.; Pemberton, J. E. *J. Am. Chem. Soc.* **1991**, *113*, 8284-8293.
- (110) Cho, S. I.; Park, E. S.; Kim, K.; Kim, M. S. *J. Mol. Struct.* **1999**, *479*, 83-92.
- (111) Murty, K. V. G.; Venkataramanan, M.; Pradeep, T. *Langmuir* **1998**, *14*, 5446-5456.
- (112) Nuzzo, R. G.; Dubois, L. H.; Allara, D. L. *J. Am. Chem. Soc.* **1990**, *112*, 558-569.
- (113) Liu, M.; Guyot-Sionnest, P. *J. Phys. Chem. B* **2004**, *108*, 5882-5888.
- (114) Heath, J. R.; Knobler, C. M.; Leff, D. V. *J. Phys. Chem. B* **1997**, *101*, 189-197.

- (115) Mizushima, S.; Simanouti, T. *J. Am. Chem. Soc.* **1949**, *71*, 1320-1324.
- (116) Schaufele, R. F.; Shimanouchi, T. *J. Chem. Phys.* **1967**, *47*, 3605-3610.
- (117) Minoni, G.; Zerbi, G. *J. Phys. Chem.* **1982**, *86*, 4791-4798.
- (118) Soutzidou, M.; Glezakou, V.-A.; Viras, K.; Helliwell, M.; Masters, A. J.; Vincent, M. A. *J. Phys. Chem. B* **2002**, *106*, 4405-4411.
- (119) Snyder, R. G. *J. Chem. Phys.* **1982**, *76*, 3921-3927.
- (120) Dollish, F. R.; Fateley, W. G.; Bentley, F. F. *Characteristic Raman Frequencies of Organic Compounds*; John Wiley & Sons, Inc.: New York, 1974.
- (121) McFarland, A. D.; Young, M. A.; Dieringer, J. A.; Van Duyne, R. P. *J. Phys. Chem. B* **2005**, *109*, 11279-11285.
- (122) Moskovits, M.; Suh, J. S. *J. Am. Chem. Soc.* **1985**, *107*, 6826-6829.
- (123) Suh, J. S. *Chem. Phys. Lett.* **1992**, *193*, 327-330.
- (124) Aroca, R. F.; Clavijo, R. E.; Halls, M. D.; Schlegel, H. B. *J. Phys. Chem. A* **2000**, *104*, 9500-9505.
- (125) Vivoni, A.; Birke, R. L.; Foucault, R.; Lombardi, J. R. *J. Phys. Chem. B* **2003**, *107*, 5547-5557.
- (126) Arenas, J. F.; Soto, J.; Pelaez, D.; Fernandez, D. J.; Otero, J. C. *Int. J. Quant. Chem.* **2005**, *104*, 681-694.
- (127) Zhao, L. L.; Jensen, L.; Schatz, G. C. *J. Am. Chem. Soc.* **2006**, *128*, 2911-2919.
- (128) Suzuki, S.; Orville-Thomas, W. J. *J. Mol. Struct.* **1977**, *37*, 321-327.
- (129) Mizutani, G.; Ushioda, S. *J. Chem. Phys.* **1989**, *91*, 598-602.

(130) Braden, D. A.; Parker, S. F.; Tomkinson, J.; Hudson, B. S. *J. Chem. Phys.* **1999**, *111*, 429-437.

(131) Sardar, R.; Heap, T. B.; Shumaker-Parry, J. S. *J. Am. Chem. Soc.* **2007**, *129*, 5356-5357.

(132) Nash, C. P.; Olmstead, M. M.; Weiss-Lopez, B.; Musker, W. K.; Ramasubbu, M.; Parthasarathy, R. *J. Am. Chem. Soc.* **1985**, *107*, 7194-7195.

(133) Van Wart, H. E.; Scheraga, H. A. *Proc. Nat. Acad. Sci. U.S.A.* **1986**, *83*, 3064-3067.

(134) Parker, F. S. *Applications of Infrared, Raman, and Resonance Raman Spectroscopy in Biochemistry*; Springer, 1983.

(135) Huang, Y.-Z.; Gao, J.-Q.; Liang, W.-Q.; Nakagawa, S. *Biol. Pharm. Bull.* **2005**, *28*, 387-390.

(136) Tresset, G.; Takeuchi, S. *Anal. Chem.* **2005**, *77*, 2795-2801.

(137) Shankar, S. S.; Ahmad, A.; Pasricha, R.; Khan, M. I.; Kumar, R.; Sastry, M. *J. Colloid and Interface Sci.* **2004**, *274*, 69-75.

(138) Heurtault, B.; Saulnier, P.; Pech, B.; Proust, J.-E.; Benoit, J.-P. *Biomaterials* **2003**, *24*, 4283-4300.

(139) Hong, K.; Friend, D. S.; Glabe, C. G.; Papahadjopoulos, D. *Biochim. Biophys. Acta* **1983**, *732*, 320-323.

(140) Boyer, C.; Zasadzinski, J. A. *ACS Nano* **2007**, *1*, 176-182.

(141) Wu, G.; Mikhailovsky, A.; Khant, H. A.; Fu, C.; Chiu, W.; Zasadzinski, J. *A. J. Am. Chem. Soc.* **2008**, *130*, 8175-8177.

(142) Kasili, P. M.; Vo-Dinh, T. *Int. J. Nanotechnology* **2005**, *2*, 397-410.

(143) He, P.; Urban, M. W. *Biomacromolecules* **2005**, *6*, 1224-1225.

- (144) Barry, B. W.; Edwards, H. G. M.; Williams, A. C. *J. Raman Spectrosc.* **1992**, *23*, 641-645.
- (145) Movileanu, L.; Benevides, J. M.; Thomas, G. J. *J. Raman Spectrosc.* **1999**, *30*, 637-649.
- (146) Bicknell-Brown, E.; Brown, K. G.; Person, W. B. *J. Raman Spectrosc.* **1981**, *11*, 356-362.
- (147) Levin, C. S.; Kundu, J.; Janesko, B. G.; Scuseria, G. E.; Raphael, R. M.; Halas, N. J. *J. Phys. Chem. B* **2008**, *112*, 14168-14175.
- (148) Lichtenberger, L. M. *Annu. Rev. Physiol.* **1995**, *57*, 565-583.
- (149) Lichtenberger, L. M.; Wang, Z. M.; Romero, J. J.; C., B. J. *Gastroenterology* **1994**, *106*, A125.
- (150) Lichtenberger, L. M.; Zhou, Y.; Dial, E. J.; Raphael, R. M. *J. Pharm. Pharmacol.* **2006**, *58*, 1-8.
- (151) Zhou, Y.; Raphael, R. M. *Biophys. J.* **2005**, *89*, 1789-1801.
- (152) Jones, R. *Am. J. Med.* **2001**, *110*, 4S-7S.
- (153) Zhou, Y., Rice University, 2007.
- (154) Fox, C. B.; Horton, R. A.; Harris, J. M. *Anal. Chem.* **2006**, *78*, 4918-4924.
- (155) Brinker, C. J.; Lu, Y. F.; Sellinger, A.; Fan, H. Y. *Adv. Mater.* **1999**, *11*, 579-585.
- (156) Yang, T.-H. C.; Yee, C. K.; Amweg, M. L.; Singh, S.; Kendall, E. L.; Dattelbaum, A. M.; Shreve, A. P.; Brinker, C. J.; Parikh, A. N. *Nano Lett.* **2007**, *7*, 2446-2451.
- (157) Soten, I.; Ozin, G. A. *Curr. Opin. Colloid Interface Sci.* **1999**, *4*, 325-337.

- (158) Bishop, A. R.; Nuzzo, R. G. *Curr. Opin. Colloid Interface Sci.* **1996**, *1*, 127-136.
- (159) Whitesides, G. M.; Mathias, J. P.; Seto, C. T. *Science* **1991**, *254*, 1312-1319.
- (160) Twardowski, M.; Nuzzo, R. G. *Langmuir* **2003**, *19*, 9781-9791.
- (161) Garrett, R. H.; Grisham, C. M. *Biochemistry 3rd edition*; Harris, D., 2005.
- (162) Meuse, C. W.; Niaura, G.; Lewis, M. L.; Plant, A. L. *Langmuir* **1998**, *14*, 1604-1611.
- (163) Castellana, E. T.; Cremer, P. S. *Surf. Sci. Rep.* **2006**, *61*, 429-444.
- (164) Anderson, N. A.; Richter, L. J.; Stephenson, J. C.; Briggman, K. A. *J. Am. Chem. Soc.* **2007**, *129*, 2094-2100.
- (165) Wang, H.; Brandl, D. W.; Nordlander, P.; Halas, N. J. *Acc. Chem. Res.* **2007**, *40*, 53-62.
- (166) Kagan, M. R.; McCreery, R. L. *Langmuir* **1995**, *11*, 4041-4047.
- (167) Schatz, G. C.; Van Duyne, R. P. In *Handbook of Vibrational Spectroscopy*; Chalmers, J. M., Griffiths, P. R., Eds.; John Wiley & Sons Ltd Chichester, 2002, p 1-16.
- (168) Doering, W. E.; Nie, S. *J. Phys. Chem. B* **2002**, *106*, 311-317.
- (169) Schwartzberg, A. M.; Grant, C. D.; Wolcott, A.; Talley, C. E.; Huser, T. R.; Bogomolni, R.; Zhang, J. Z. *J. Phys. Chem. B* **2004**, *108*, 19191-19197.
- (170) Dieringer, J. A.; McFarland, A. D.; Shah, N. C.; Stuart, D. A.; Whitney, A. V.; Yonzon, C. R.; Young, M. A.; Zhang, X.; Van Duyne, R. P. *Faraday Discuss.* **2005**, *132*, 1-18.
- (171) Jiang, X.; Campion, A. *Chem. Phys. Lett.* **1987**, *140*, 95-100.



(172) Yonzon, C. R.; Zhang, X.; Van Duyne, R. P. In *Proc. of SPIE Nanomaterials and Their Optical Applications*; Cao, G., Xia, Y., Braun, P. V., Eds. Bellingham, WA, 2003; Vol. 5224, p 78-85.

(173) Porter, M. D.; Bright, T. B.; Allara, D. L.; Chidsey, C. E. D. *J. Am. Chem. Soc.* **1987**, *109*, 3559-3568.

(174) Du, L.; Liu, X.; Huanga, W.; Wang, E. *Electrochim. Acta* **2006**, *51*, 5754-5760.

(175) Ridell, A.; Evertsson, H.; Nilsson, S.; Sundelöf, L. O. *J. Pharm. Sci.* **1999**, *88*, 1175-1181.

(176) Henkel, T.; Mittler, S.; Pfeiffer, W.; Rötzer, H.; Apell, H.-J.; Knoll, W. *Biochimie* **1989**, *71*, 89-98.

(177) Koynova, R.; Caffrey, M. *Biochim. Biophys. Acta* **1998**, *1376*, 91-145.

(178) Parasassi, T.; de Felip, E.; Lepore, F.; Conti, F. *Cell. Mol. Biol.* **1986**, *32*, 261-266.

(179) Parasassi, T.; De Stasio, G.; d'Ubaldo, A.; Gratton, E. *Biophys. J.* **1990**, *57*, 1179-1186.

(180) Bagatolli, L. A.; Gratton, E.; Fidelio, G. D. *Biophys. J.* **1998**, *75*, 331-341.

(181) Bagatolli, L. A.; Gratton, E. *Biophys. J.* **1999**, *77*, 2090-2101.

(182) Bagatolli, L. A.; Gratton, E. *Biophys. J.* **2000**, *78*, 290-305.

(183) Zhou, Y.; Raphael, R. M. *Biophys. J.* **2007**, *92*, 2451-2462.

(184) Kouaouci, R.; Silvius, J. R.; Graham, I.; Pézolet, M. *Biochemistry* **1985**, *24*, 7132-7140.

(185) Wang, Y.; Ying-Sing, L.; Zhang, Z.; An, D. *Spectrochim. Acta, Part A* **2003**, *59*, 589-594.

(186) Jubert, A.; Legarto, M. L.; Massa, N. E.; Tévez, L. L.; Okulik, N. B. *J. Mol. Struct.* **2006**, *783*, 34-51.

(187) Gordijo, C. R.; Barbosa, C. A. S.; Da Costa Ferreira, A. M.; Constantino, V. R. L.; de Oliveira Silva, D. *J. Pharm. Sci.* **2005**, *94*, 1135-1148.

(188) Garrigues, S.; Gallignani, M.; De La Guardia, M. *Talanta* **1993**, *40*, 89-93.

(189) Bondesson, L. M., K. V.; Luo, Y.; Garberg, P.; Agren, H. *Spectrochim. Acta, Part A* **2007**, *66*, 213-224.

(190) Chan, K. L. A.; Kazarian, S. G. *J. Comb. Chem.* **2006**, *8*, 26-31.

(191) Khan, G. M.; Jiabi, Z. *Drug Dev. Ind. Pharm.* **1998**, *24*, 463-471.

(192) Shakhtshneider, T. P.; Vasilchenko, M. A.; Politov, A. A.; Boldyrev, V. *V. Int. J. Pharm.* **1996**, *130*, 25-32.

(193) Kazarian, S. G.; Martirosyan, G. G. *Int. J. Pharm.* **2002**, *232*, 81-90.

(194) Hübner, W.; Mantsch, H. H. *Biophys. J.* **1991**, *59*, 1261-1272.

(195) Wilkop, T.; Xu, D.; Cheng, Q. *Langmuir* **2008**, *24*, 5615-5621.

(196) Al-Saidan, S. M. *J. Controlled Release* **2004**, *100*, 199-209.

(197) Bergethon, P. R. *The Physical Basis of Biochemistry: The Foundations of Molecular Biophysics*; Springer, 1998.

(198) Hostetler, M. J.; Stokes, J. J.; Murray, R. W. *Langmuir* **1996**, *12*, 3604-3612.

(199) Tamm, L. K.; Tatulian, S. A. *Q. Rev. Biophys.* **1997**, *30*, 365-429.

(200) Blume, A.; Hübner, W.; Messner, G. *Biochemistry* **1988**, *27*, 8239-8249.

- (201) Reneker, D. H.; Fanconi, B. J. *J. Appl. Phys.* **1975**, *46*, 4144.
- (202) Loo, B. H. *J. Phys. Chem.* **1982**, *86*, 433-437.
- (203) Wetzell, H.; Gerischer, H. *Chem. Phys. Lett.* **1980**, *73*, 460-464.
- (204) Finkelstein, N. P.; Hancock, R. D. *Gold Bull.* **1974**, *7*, 72-77.
- (205) Shi, Z.; Lipkowski, J. *J. Electroanal. Chem.* **1996**, *403*, 225-239.
- (206) Braunstein, P.; Clark, R. J. H. *J. Chem. Soc., Dalton Trans.* **1973**, 1845-1848.
- (207) Chen, A.; Shi, Z.; Bizzotto, D.; Lipkowski, J.; Pettinger, B.; Bilger, C. *J. Electroanal. Chem.* **1999**, *467*, 342-353.
- (208) Jones, L. H. *Inorg. Chem.* **1964**, *3*, 1581-1586.
- (209) Aguirre, C. M.; Kaspar, T. R.; Radloff, C.; Halas, N. J. *Nano Lett.* **2003**, *3*, 1707-1711.
- (210) Gao, J.; Bender, C. M.; Murphy, C. J. *Langmuir* **2003**, *19*, 9065-9070.
- (211) Li, M.-D.; Cui, Y.; Gao, M.-X.; Luo, J.; Ren, B.; Tian, Z.-Q. *Anal. Chem.* **2008**, *80*, 5118-5125.
- (212) Delgado, J. M.; Orts, J. M.; Pérez, J. M.; Rodes, A. *J. Electroanal. Chem.* **2008**, *617*, 130-140.
- (213) Jang, N. H. *Bull. Korean Chem. Soc.* **2002**, *23*, 1790-1800.
- (214) Gutiérrez, M. D.; López, R.; Romero, M. A.; Salas, J. M. *Can. J. Chem.* **1988**, *66*, 249-255.
- (215) Radanović, D. J.; Matović, Z. D.; Ponticelli, G.; Scano, P.; Efimenko, I. A. *Transition Met. Chem.* **1994**, *19*, 646-650.

- (216) Xu, B.; Xiao, X.; Tao, N. *J. Am. Chem. Soc.* **2003**, *125*, 16164-16165.
- (217) Sauer, G.; Brehm, G.; Schneider, S. *J. Raman Spect.* **2004**, *35*, 568-576.
- (218) Bron, M.; Holze, R. *J. Electroanal. Chem.* **1995**, *385*, 105-113.
- (219) Pavel, I.; Szeghalmi, A.; Moigno, D.; Cîntă, S. K., W. *Biopolymers (Biospectroscopy)* **2003**, *72*, 25-37.
- (220) Martin, A.; Bustamante, P.; Chun, A. H. C. *Physical Pharmacy, 4th ed.*; Lea & Febiger: Philadelphia, 1993.
- (221) Gutterson, M.; Ma, T. S. *Microchim. Acta* **1960**, *48*, 1-11.
- (222) Yan, H.; Jin, L.; Row, K. H. *J. Liq. Chromatogr. Related Technol.* **2005**, *28*, 3147-3155.
- (223) Falk, M.; Gil, M.; Iza, N. *Can. J. Chem.* **1990**, *68*, 1293-1299.
- (224) Angell, C. L. *J. Chem. Soc.* **1961**, 504-515.
- (225) Dick, L. A.; McFarland, A. D.; Haynes, C. L.; Van Duyne, R. P. *J. Phys. Chem. B* **2002**, *106*, 853-860.
- (226) Creighton, J. A.; Blatchford, C. G.; Albrecht, M. G. *J. Chem. Soc., Faraday Trans. 2* **1979**, *75*, 790-798.
- (227) Janesko, B. G.; Scuseria, G. E., personal communication.
- (228) Loudon, G. M. *Organic Chemistry 4th Edition*; Oxford University Press, 2002.
- (229) Shindo, H. *J. Chem. Soc., Faraday Trans. 1* **1986**, *82*, 45-51.
- (230) Baibarac, M.; Mihut, L.; Louarn, G.; Lefrant, S.; Baltog, I. *J. Polym. Sci., Part B: Polym. Phys.* **2000**, *38*, 2599-2609.

- (231) Roth, E.; Engert, C.; Kiefer, W. *J. Mol. Struct.* **1995**, *349*, 89-92.
- (232) Ilic, M.; Koglin, E.; Pohlmeier, A.; Narres, H. D.; Schwuger, M. J. *Langmuir* **2000**, *16*, 8946-8951.
- (233) Holze, R. *J. Electroanal. Chem.* **1988**, *250*, 143-157.
- (234) Holze, R. *Electrochim. Acta* **1987**, *32*, 1527-1532.
- (235) Whaley, S. R.; English, D. S.; Hu, E. L.; Barbara, P. F.; Belcher, A. M. *Nature* **2000**, *405*, 665-668.
- (236) Slocik, J. M.; Stone, M. O.; Naik, R. R. *Small* **2005**, *1*, 1048-1052.
- (237) Xiong, X.; Gungormus, M.; Tamerler, C.; Sarikaya, M.; Parviz, B. A. *Proc. Of 2005 IEEE conference on Nanotechnology Nagoya, Japan* **2005**, 0-7803-9199-3.
- (238) Slocik, J. M.; Tam, F.; Halas, N. J.; Naik, R. R. *Nano Lett.* **2007**, *7*, 1054-1058.
- (239) Tullman, J. A.; Finney, W. F.; Lin, Y.-J.; Bishnoi, S. W. *Plasmonics* **2007**, *2*, 119-127.
- (240) McHale, J. L. *J. Raman Spectrosc.* **1982**, *13*, 21-24.
- (241) Lord, R. C.; Yu, N.-T. *J. Mol. Biol.* **1970**, *51*, 203-213.
- (242) Herne, T. M.; Ahern, A. M.; Garrell, R. L. *Anal. Chim. Acta* **1991**, *246*, 75-84.
- (243) Lee, H. I.; Suh, S. W.; Kim, M. S. *J. Raman Spectrosc.* **1988**, *19*, 491-495.
- (244) Ricardo, A. In *Surface Enhanced Vibrational Spectroscopy*; Wiley: 2006.

(245) Miessler, G. L.; Tarr, D. A. *Inorganic Chemistry 2nd edition*; Prentice Hall: New Jersey 1998.

(246) Gilman, S. J. *J. Phys. Chem.* **1964**, *68*, 70-80.

(247) Joshi, A. M.; Tucker, M. H.; Delgass, W. N.; Thomson, K. T. *J. Chem. Phys.* **2006**, *125*, 194707.

(248) Yim, W.-L.; Nowitzki, T.; Necke, M.; Schnars, H.; Nickut, P.; Biener, J.; Biener, M. M.; Zielasek, V.; Al-Shamery, K.; Kluner, T.; Baumer, M. *J. Phys. Chem. C* **2007**, *111*, 445-451.

(249) Mavrikakis, M.; Stoltze, P.; Nørskov, J. K. *Catalysis Lett.* **2000**, *64*, 101-106.

(250) Farrugia, T. R.; Fredlein, R. A. *Aust. J. Chem.* **1984**, *37*, 2415-20.

(251) Mott, D.; Luo, J.; Smith, A.; Chan, W.-P.; Bozza, W.; Sarkhel, A.; Park, S.; Zhong, C.-J. *MRS Proceedings* **2005**, *900E*, 0900-O01-06.1.

(252) Wadayama, T.; Abe, K.; Osano, H. *Appl. Surf. Sci.* **2006**, *253*, 2540-2546.

(253) Park, E. J., Texas Tech University, 2002.

(254) Levin, C. S.; Hofmann, C.; Ali, T. A.; Kelly, A. T.; Morosan, E.; Nordlander, P.; Whitmire, K. H.; Halas, N. J. *ACS Nano* **2009**, *Submitted*.

(255) Insin, N.; Tracy, J. B.; Lee, H.; Zimmer, J. P.; Westervelt, R. M.; Bawendi, M. G. *ACS Nano* **2008**, *2*, 197-202.

(256) Weng, K. C.; Noble, C. O.; Papahadjopoulos-Sternberg, B.; Chen, F. F.; Drummond, D. C.; Kirpotin, D. B.; Wang, D.; Hom, Y. K.; Hann, B.; Park, J. W. *Nano Lett.* **2008**, *8*, 2851-2857.

(257) Prodan, E.; Nordlander, P.; Halas, N. J. *Chem. Phys. Lett.* **2003**, *368*, 94-101.

- (258) Chiang, I.-C.; Chen, D.-H. *Adv. Funct. Mater.* **2007**, *17*, 1311-1316.
- (259) Carpenter, E. E.; Kumbhar, A.; Wiemann, J. A.; Srikanth, H.; Wiggins, J.; Zhou, W. L.; O'Connor, C. J. *Mater. Sci. Eng., A* **2000**, *286*, 81-86.
- (260) Chen, M.; Yamamuro, S.; Farrell, D.; Majetich, S. A. *J. Appl. Phys.* **2003**, *93*, 7551-7553.
- (261) Cho, S.-J.; Jarrett, B. R.; Louie, A. Y.; Kauzlarich, S. M. *Nanotechnology* **2006**, *17*, 640-44.
- (262) Lim, J.; Tilton, R. D.; Eggeman, A.; Majetich, S. A. *J. Magn. Magn. Mater.* **2007**, *311*, 78-83.
- (263) Mikhaylova, M.; Kim, D. K.; Bobrysheva, N.; Osmolowsky, M.; Semenov, V.; Tsakalatos, T.; Muhammed, M. *Langmuir* **2004**, *20*, 2472-2477.
- (264) Shevchenko, E. V.; Bodnarchuk, M. I.; Kovalenko, M. V.; Talapin, D. V.; Smith, R. K.; Aloni, S.; Heiss, W.; Alivisatos, A. P. *Adv. Mater.* **2008**, *20*, 4323-4329.
- (265) Stoeva, S. I.; Huo, F.; Lee, J.-S.; Mirkin, C. A. *J. Am. Chem. Soc.* **2005**, *127*, 15362-15363.
- (266) Salgueiriño-Maceira, V.; Correa-Duarte, M. A.; Farle, M.; López-Quintela, A.; Sieradzki, K.; Diaz, R. *Chem. Mater.* **2006**, *18*, 2701-2706.
- (267) Schotter, J.; Bethge, O.; Maier, T.; Brueckl, H. *Appl. Phys. Lett.* **2008**, *93*, 144105.
- (268) Yin, M.; O'Brien, S. *J. Am. Chem. Soc.* **2003**, *125*, 10180-10181.
- (269) Redl, F. X.; Black, C. T.; Papaefthymiou, G. C.; Sandstrom, R. L.; Yin, M.; Zeng, H.; Murray, C. B.; O'Brien, S. *J. Am. Chem. Soc.* **2004**, *126*, 14583-14599.
- (270) Yin, M.; Chen, Z.; Deegan, B.; O'Brien, S. *J. Mater. Res.* **2007**, *22*, 1987-1989.

(271) Park, J.; An, K.; Hwang, Y.; Park, J.-G.; Noh, H.-J.; Kim, J.-Y.; Park, J.-H.; Hwang, N.-M.; Hyeon, T. *Nat. Mater.* **2004**, *3*, 891-895.

(272) Palnichenko, A. V.; Rossolenko, A. N.; Kopylov, V. N.; Zver'kova, I. I.; Aronin, A. S. *Chem. Phys. Lett.* **2005**, *410*, 436-440.

(273) Emel'yanov, D. A.; Korolev, K. G.; Mikhailenko, M. A.; Knot'ko, A. V.; Oleinikov, N. N.; Tret'yakov, Y. D.; Boldyrev, V. V. *Inorg. Mater.* **2004**, *40*, 632-635.

(274) Matteazzi, P.; Le Caër, G. *Mater. Sci. Eng., A* **1991**, *149*, 135-142.

(275) Hofmann, C.; Rusakova, I.; Ould-Ely, T.; Prieto-Centurión, D.; Hartman, K. B.; Kelly, A. T.; Lüttge, A.; Whitmire, K. H. *Adv. Funct. Mater.* **2008**, *18*, 1661-1667.

(276) Gould, P. *Mater. Today* **2004**, *7*, 36-43.

(277) Perrin, D. D.; Armarego, W. L. *Purification of Laboratory Chemicals*; 5th ed.; Pergamon Press: New York, 1993.

(278) Brinson, B. E.; Lassiter, J. B.; Levin, C. S.; Bardhan, R.; Mirin, N.; Halas, N. J. *Langmuir* **2008**, *24*, 14166-14171.

(279) Wang, H.; Brandl, D. W.; Le, F.; Nordlander, P.; Halas, N. J. *Nano Lett.* **2006**, *6*, 827-832.

(280) De Palma, R.; Peeters, S.; Van Bael, M. J.; Van den Rul, H.; Bonroy, K.; Laureyn, W.; Mullens, J.; Borghs, G.; Maes, G. *Chem. Mater.* **2007**, *19*, 1821-1831.

(281) Duff, D. G.; Baiker, A.; Edwards, P. P. *Langmuir* **1993**, *9*, 2301-2309.

(282) Oldenburg, S. J.; Jackson, J. B.; Westcott, S. L.; Halas, N. J. *Appl. Phys. Lett.* **1999**, *75*, 2897-2899.

(283) Xu, Z.; Hou, Y.; Sun, S. *J. Am. Chem. Soc.* **2007**, *129*, 8698-8699.

(284) Taton, T. A.; Lu, G.; Mirkin, C. A. *J. Am. Chem. Soc.* **2001**, *123*, 5164-5165.



- (285) Cao, Y. C.; Jin, R.; Mirkin, C. A. *J. Am. Chem. Soc.* **2001**, *123*, 7961-7962.
- (286) Hao, F.; Nordlander, P. *Chem. Phys. Lett.* **2007**, *446*, 115-118.
- (287) Wang, H.; Wu, Y.; Lassiter, B.; Nehl, C. L.; Hafner, J. H.; Nordlander, P.; Halas, N. J. *Proc. Natl. Acad. Sci. U.S.A.* **2006**, *103*, 10856-10860.
- (288) Wu, Y. P.; Nordlander, P. *J. Chem. Phys.* **2006**, *125*, 124708.
- (289) Querry, M. R.; University of Missouri: 1985.
- (290) Henning, T.; Begemann, B.; Mutschke, H.; Dorschner, J. *Astron. Astrophys. Suppl. Ser.* **1995**, *112*, 143-149.
- (291) Gole, A.; Stone, J. W.; Gemmill, W. R.; zur Loye, H.-C.; Murphy, C. J. *Langmuir* **2008**, *24*, 6232-6237.
- (292) de Faria, D. L. A.; Silva, S. V.; de Oliveira, M. T. *J. Raman Spec.* **1997**, *28*, 873-878.
- (293) Cullity, B. D.; Stock, S. R. *Elements of X-ray Diffraction*; Prentice Hall: Upper Saddle River, NJ, 2001.
- (294) Stöhr, J.; Siegmann, H. C. *Magnetism*; Springer: New York.
- (295) Kittel, C. *Introduction to Solid State Physics*; John Wiley & Sons, Inc.: Hoboken, NJ, 2005.
- (296) Fjellvåg, H.; Hauback, B. C.; Vogt, T.; Stølen, S. *Am. Mineral.* **2002**, *87*, 347-349.
- (297) Morrish, A. H. *The Physical Principles of Magnetism* John Wiley & Sons, Inc., 1965.

(298) Crespo, P.; Litrán, R.; Rojas, T. C.; Multigner, M.; de la Fuente, J. M.; Sánchez-López, J. C.; Garcíá, M. A.; Hernando, A.; Penadés, S.; Fernández, A. *Phys. Rev. Lett.* **2004**, *93*, 087204-1-4.

(299) Hori, H.; Yamamoto, Y.; Iwamoto, T.; Miura, T.; Teranishi, T.; Miyake, M. *Phys. Rev. B* **2004**, *69*, 174411-1-5.

(300) Reich, S.; Leitus, G.; Feldman, Y. *Appl. Phys. Lett.* **2006**, *88*, 222502-1-3.

(301) Zhou, W. L.; Carpenter, E. E.; Lin, J.; Kumbhar, A.; Sims, J.; O'Connor, C. J. *Eur. Phys. J. D* **2001**, *16*, 289-292.

(302) Roberts, R. M.; Gilbert, J. C.; Martin, S. F. *Experimental Organic Chemistry: A Miniscale Approach*; Saunders College Publishing: Orlando, FL, 1994.

## Appendix A: TEOS purification by simple distillation

Illustrated in Figure A1 is the setup for a simple distillation apparatus.<sup>302</sup> After thorough cleaning and drying of the glassware (which may be rinsed with acetone for faster drying), the ground glass joints are greased. The distillation setup is connected to the house vacuum line and cold water flows through the condenser. The distillation flask and still head are wrapped with glass wool for even heating. Boiling chips are not needed. Tetraethylorthosilicate (TEOS, 99.999%, Sigma Aldrich) is removed from the glovebox shortly before the reaction and slightly more than the desired amount is placed into the distillation (round bottom) flask.

The heating mantle is connected to a variable autotransformer (Staco Energy Products Co., Dayton, Ohio), which is plugged into a standard wall outlet. Typical settings for this procedure are 140 Volts for the output switch and 70 Volts for the maximum output voltage knob. The distillation is stopped before all of the TEOS has condensed into the

receiving flask so that a few milliliters remain in the distillation flask and any remaining impurities are removed.

After distillation, the TEOS is added to a combined solution of ethanol (200 Proof, Pharmco-Aaper) and ammonium hydroxide (28%  $\text{NH}_3$  in water, Sigma Aldrich). Ammonium hydroxide over six months old cannot be used. The materials are combined in dry glassware with a Teflon coated stir bar in the fume hood, as ammonium hydroxide has a pungent smell and may be harmful if inhaled. The flask is then covered and allowed to stir overnight or for at least 8 hours.

Some example Stöber recipes include: 45 mL of ethanol, 1.7 mL of TEOS, and 4.0 mL of ammonium hydroxide to yield 270 nm particles and 45 mL of ethanol, 1.5 mL of TEOS, and 3.6 mL of ammonium hydroxide to yield 130 nm particles. Making an array of several 125 mL Erlenmeyer flasks with various TEOS and ammonia hydroxide concentrations can help when aiming for a specific particle size.

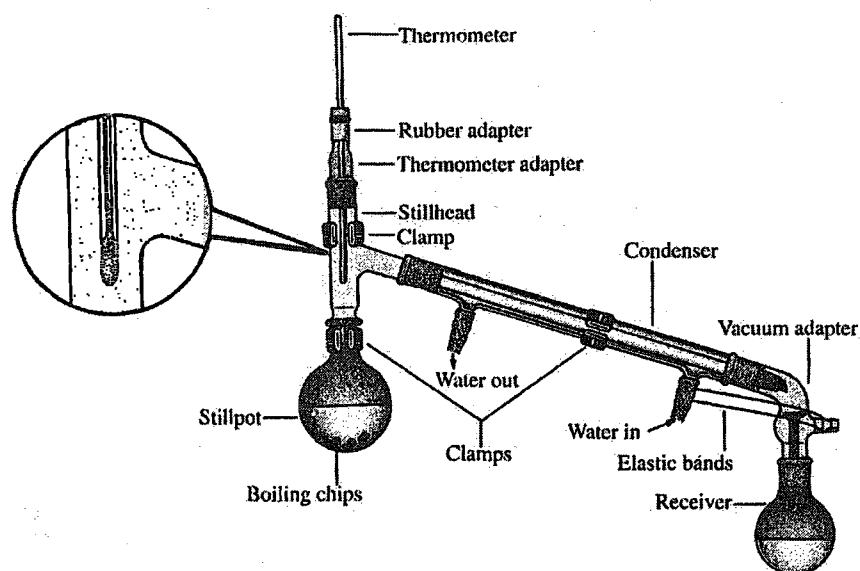


**Figure 0.1:** Typical apparatus for simple distillation at atmospheric temperature or under vacuum. Inset shows correct placement of thermometer in stillhead.

## **Appendix B: Image processing and nanoshell sizing using the Scion Image program**

The Scion Image program for Windows is available free of charge and can be downloaded through the NIST and Scion Corp websites. A current link to download the program is: [http://www.scioncorp.com/pages/scion\\_image\\_windows.htm](http://www.scioncorp.com/pages/scion_image_windows.htm)

Once downloaded and installed, the image files to be processed should be saved directly to the desktop as a .tiff file, otherwise an error can occur that reads the program is “unable to open the selected file”. After opening the file with the Scion Image software, the scale for the image is set. A simple way to determine the equivalent length scale of the image scale bar to that in pixels is to draw a line using the line tool on top of the scale bar in the image and reading the pixel number shown in the info window. Next, the scale can be set by going to the menu bar analyze and selecting set scale. The units should be set to that of the image scale bar, typically micrometers or nanometers, the known distance of the scale bar entered, and the measured distance in pixels entered, obtained earlier from the info window. If the image was obtained using an SEM and has a black background, the image should be inverted by clicking on the image, selecting edit from the menu bar and then invert. Next, select options threshold to convert the image from grayscale to black and white. The threshold can be adjusted accordingly by clicking in the LUT window. Note that adjustment of threshold is a source of error in the particle measurement.

Any particle aggregates, irregularities in the background, and SEM information can be erased using the eraser tool. Under analyze options, the area, mean density, and include interior holes boxes should be selected and the digits right of the decimal point should be changed from 2 to a larger number, such as 5. The particles can now be

measured by selecting analyze, analyze particles and the minimum particle size should be changed to a reasonable number like 20. Select analyze show results and then file export. Remove the .tif extension and save the file as a text file.

The text file can now be opened in Excel. When opening the file select delimited and then tab so that the data appears in two separate columns. The first column is the particle area and the second is the mean. Once a column of over 100 particle sizes has been generated, an average and standard deviation of the cells can be obtained. The units for the average will be equivalent to the units selected when the scale was set. If, for example, the average is in microns, then a conversion needs to be performed to calculate the radius in nanometers. Since the image is two dimensional, the radius in nanometers for a spherical particle can be calculated using the equation for the area of a circle, where here,  $r = (A/\pi)^{1/2} * 1000$ . If the particles were sputter coated, then the thickness of the sputter coating in nanometers obtained from the thickness monitor should then be subtracted from the calculated radius. The surface area of the particles in  $\text{nm}^2$  can be calculated using the equation for spherical particles, where,  $A = 4\pi r^2$ . Also, the standard deviation in the radius in microns can be obtained, where,  $\text{stdev in the } r = 1000 * \text{stdev in } A/(2\pi r)$ . This value can be then converted to nanometers by multiplying by 1000.

### **Appendix C: Calculating nanoshell concentration using the Beer-Lambert law**

Once the nanoshell extinction spectra and experimentally determined radii are compared with that obtained using Mie theory, the Beer-Lambert law can be used to calculate nanoparticle concentration. The Beer-Lambert law states:

$$A = -\log_{10} \left( \frac{I}{I_0} \right) = \epsilon l c \quad \text{Equation 6}$$

where  $A$  is the absorbance (unitless),  $I_0$  and  $I$  are the intensity of the incident light and the intensity of the light after the material,  $\epsilon$  is the molar absorptivity ( $\text{L mol}^{-1} \text{cm}^{-1}$ ),  $l$  is the path length of the sample (cm), and  $c$  is the concentration in solution ( $\text{mol L}^{-1}$ ). Since the molar absorptivity,  $\epsilon$ , is directly related to the absorption cross section,  $\sigma$ , and the concentration,  $c$ , is related to the number of particles in solution, the equation above can be rearranged and expressed as:

$$N = \frac{A_{EXP} * 2.303}{\sigma * A_{particle} * l} \quad \text{Equation 7}$$

where  $N$  is the number of particles per mL of solution,  $A_{EXP}$  is the experimentally measured peak absorption efficiency (unitless), 2.303 is a conversion factor between a natural log and a base 10 log,  $\sigma$  is the absorption cross section,  $A_{particle}$  is the area of the particle ( $\text{cm}^2$ ), and  $l$  is the path length (cm). Therefore, the number of particles per mL of solution can be calculated once both the experimental and theoretical spectra have been normalized at the maximum absorption values and the area of the particle has been determined. More details on calculating nanoshell density can be found in Brinson *et al.*<sup>278</sup>

## Appendix D: SERS substrate development

There are various substrate choices for nanoparticle placement when performing SERS measurements using a microRaman geometry. It is important to obtain a Raman scan of the substrate alone to get an idea of how it may contribute to the signal. Previously utilized substrates include cut pieces of glass (Gold Seal, Portsmouth, NH), quartz (Technical Glass Products, Inc., Painesville Twp., OH), or silicon (Addison Engineering, Inc., San Jose, CA). While glass is an inexpensive, transparent substrate, it

has a fluorescence signal (a broad peak between  $1000\text{ cm}^{-1}$  and  $2000\text{ cm}^{-1}$ ) that will contribute to the background. Quartz, however, has a much lower intensity background and can be easily cleaned with acetone and reused. Silicon also has a low overall background, but it has sharp peaks present at  $304\text{ cm}^{-1}$ ,  $520\text{ cm}^{-1}$  (the first order phonon mode),  $944\text{ cm}^{-1}$ , and a broad peak at around  $2400\text{ cm}^{-1}$ .

The substrates are cut to the desired size using a diamond edge glass cutter and cleaned with piranha by slow, complete immersion in a solution of 1:3  $\text{H}_2\text{O}_2$  in conc.  $\text{H}_2\text{SO}_4$  for 1-2 hours. (If desired, once the solution has stabilized and cooled it can be heated on a hotplate with low heat, around 70 degrees, for a few minutes). Substrates are then rinsed thoroughly with MilliQ water, to bring the pH back to normal (around 5 for milliQ, which can be tested with pH paper), rinsed again with ethanol, and dried with nitrogen.

Cleaned substrates may be functionalized with an adhesion layer. It is generally a good idea to take a Raman scan of just the substrate with an adhesion layer and a scan of the substrate, adhesion layer, and nanoparticles to see if there are any consistent SERS signals from the adhesion later. A few examples of previously utilized adhesion layers are 3-Aminopropyltriethoxysilane (APTES), poly(4-vinylpyridine) (PVP), and poly-L-lysine.

Details regarding APTES functionalization can be found in the chapter titled “tailoring the surface with silanes” in the Gelest Catalog. For dry samples, APTES works well, but the nanoparticles may “jump off” the substrate when hydrated under the immersion objective. For PVP functionalization, a 1% (or 0.1% for a thinner adhesion layer) (w/w) solution of PVP (average mol. wt.  $\sim 160,000$ , Aldrich) was prepared in 200 proof ethanol. Substrates were either spin coated with the polymer (for more even

deposition) or immersed in a Petri dish of the solution for two hours. The substrates are then rinsed with 200 proof ethanol, dried with nitrogen, and allowed to cure either in the oven for a few hours or overnight at room temperature to allow for crosslinking of the polymer. This deposition technique allows for many single distributed nanoparticles as opposed to nanoparticle aggregates. For poly-L-lysine functionalization, the substrates were immersed in poly-L-lysine solution (0.01 % (w/v) in water, mol. wt. 150,000-300,000, Sigma) for 20 minutes. They were then rinsed with water and dried with nitrogen. Since the solution is in the polymeric form, it is not necessary to allow for curing, however, more nanoparticle aggregates may be present with this technique. Eight well, 9 mm diameter secure-seal adhesive spacers (Molecular Probes/Invitrogen, Eugene, Oregon) were also utilized to contain the area where the nanoshells deposited as well as hold the 100 uL of water/buffer when immersing the 63x objective for in solution SERS measurements. After nanoparticle deposition, SEM images were obtained to determine sample density, nanoparticle size, and number and aggregate size.